

**Studies on control of active species and design of gas molecules for
etching of dielectric films in fluorocarbon and related-gas plasmas**

KONDO Yusuke

2015

Department of Electrical Engineering and Computer Science
Graduate School of Engineering, Nagoya University

Chapter 1 Introduction

1.1 Trends in future generations of large scale integrated circuits	1
1.2 Reactive ion etching of fluorocarbon plasma	6
1.3 Problems for dielectric film etching processes	9
1.4 Development and selection of feedstock gas molecule	11
1.5 Purposes and Construction of this thesis	13
1.6 References	15

Chapter 2 Experimental and simulation methods

2.1 Quadrupole Mass Spectrometer	19
2.2 Plasma Absorption Probe (PAP)	22
2.3 Optical interferometer	24
2.4 Optical Emission Spectroscopy	26
2.5 Spectroscopic Ellipsometry	29
2.6 Molecular Orbital Calculations	35
2.7 References	37

Chapter 3 Mechanism of dissociation of C_3F_6O and $C_5F_{10}O$ induced by electron

3.1 Introduction	39
3.2 Dissociative ionization and dissociative electron attachment reaction of C_3F_6O	41
3.2.1 Experimental detail	41
3.2.2 Cracking pattern of C_3F_6O induced by electron	43
3.2.3 Potential curves of positive ion state and negative ion state of C_3F_6O	48
3.3 Dissociative ionization and dissociative electron attachment	58
3.3.1 Experimental detail	58
3.3.2 Cracking pattern of $C_5F_{10}O$ induced by electron	62
3.3.3 Potential curves of positive ion state and negative ion state of $C_5F_{10}O$	68

3.4 Conclusion	80
3.4 Reference.....	81
 Chapter 4 Mechanism of dissociation and etching process of hydro-fluorocarbon in rare gas diluted plasma	
4.1 Introduction	84
4.2 Comparison of dissociation reaction and ion density in CH_xF_y plasma.....	86
4.3 Dissociation reaction of C-H and C-F bonds in CH_2F_2	91
4.3.1 Experimental detail	91
4.3.2 Mechanism of selective dissociation of C-H and C-F in CH_2F_2	93
4.3.3 Etch rate of SiO_2 , Si_3N_4 and poly-Si by $\text{CH}_2\text{F}_2/\text{Ar}/\text{Kr}$ plasma	108
4.4 Conclusion	117
4.5 References	119
 Chapter 5 Conclusions and future works	
5.1 Conclusion of present research	123
5.2 Future scope	126
 Acknowledgements	 129
List of papers	133

Chapter 1 Introduction

1.1 Trends in future generations of large scale integrated circuits

Information technology (IT) has been continuously evolving and reaching the current state is called as information technology society. The need for electronic devices such as laptops, personal computers, tablets, and mobile phones (particularly smartphones) increases significantly year by year. Those electronic devices is expected to be increasing, however they involve improvements in terms of high ability of information processing, scaling down and expanded functionality in single chip. The silicon based ultra large scale integrated (ULSI) circuit has been used for information processing in these devices. CPU, random access memory (Static random access memory: SRAM, Dynamic Random Access Memory: DRAM) and Flash memory are typical ULSI devices. These chips play an important role as a core and determine the performance of electronic devices. To respond the large demands for the high performance of electronic devices, many researchers have been investigating: high integration of ULSI chips and high speed information processing.

Since four decades until now the development of semiconductor industry has been carried out by the rapid pace of improvements of cost, speed, and power of the consumer products. Most of the improvements have been accomplished principally by the industry's ability to exponentially decrease the minimum feature size used to fabricate ULSI. The most frequently cited trend is in integration level, which is usually expressed as Moore's Law proposed in 1965 (that is, the number of components per chip will double roughly every year).^[1] The most significant trend is the decreasing of cost-per-function, which has led to significant improvements of the economic productivity (profitability) and the overall quality of life through proliferation of computers, communication tool, and other industrial and consumer

electronics in the sophisticated information society.

There is another widely known law to keep Moore's Law active. This law called as "scaling law" was proposed in 1974 by R. H. Dennard *et al.* ^[2] They expected that the improvement of device performances could be achieved by the miniaturization of device dimension with a constant electric field in the device. (Table 1.1) If the device dimension and source voltage are reduced $1/k$ times and doping concentration is increased to k times, the delay time decreased to $1/k$ times, the power dissipation decreased to $1/k^2$ times, and integration degree becomes k^2 times, i.e., processing time, integration degree and power dissipation can be improved. Thus, the scaling law has been lead to the miniaturization of devices as a main approach for the fabrication of high performance semiconductor devices for a long time.

The DRAM, SRAM and MPU are typical examples of the improvement of devices based on the scaling laws described above. In 1998, the capacity of DRAM was increased to 1 Gbit, million times of 1 Kbit capacity of first DRAM developed in 1970. The first MPU developed by Intel Corporation in 1971 consisted of about 2,300 transistors, and was operating at 760 kHz of clock frequency. In 2010 Intel Corporation has announced the 32 nm Intel[®] Core[™] i7 Processor (Gulftown). This is a complex system on a chip with multiple functional units and multiple interfaces, including four cores, 1.17 billion transistors, and operating at the frequency of 3.33 GHz. ^[3]

In present day, the increment speed of the number of components becomes lower than that expected by the Moore's law (the number of components per chip will double roughly every two year), however it still keeps increasing exponentially and it is expected that number of devices will continue the increasing trend. Table 1.2 shows the interconnect technology requirements for MPU, DRAM and Flash memory, which was published by International Technology Roadmap for Semiconductors (ITRS). ^[4] The miniaturization is still a most fundamental key issue for development

of semiconductor devices described above.

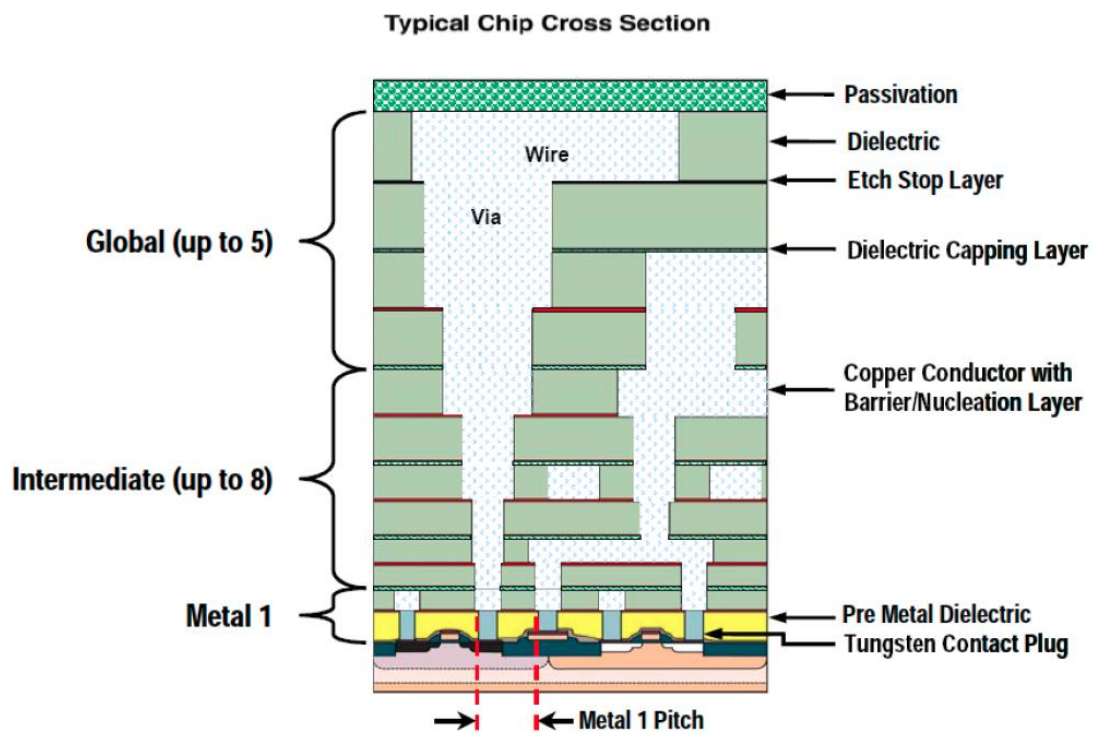


Fig. 1.1 Cross section of CMOS LSI multilevel wiring structure.

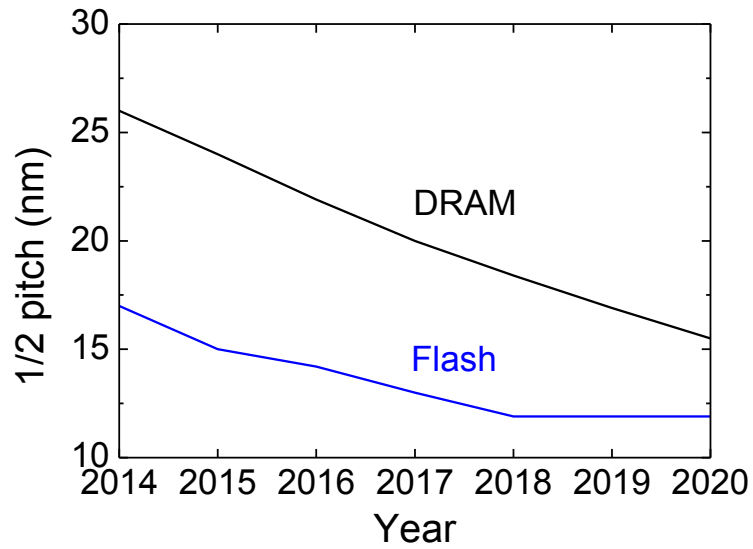


Fig. 1.2 Technology node of the DRAM and MPU.

Table 1.1 Scaling law of transistor

Decive of circuit parameter	Scaling factor
Device dimension t_{ox} , L, W	$1/k$
Doping concentration N_a	k
Voltage	$1/k$
Current	$1/k$
Capacitance	$1/k$
Delay time/circuit	$1/k$
Power dissipation/circuit	$1/k^2$
Power density	1

Table 1.2 Requirements for pitches of DRAM, MPU and Flash

Year of Production	2014	2015	2016	2017	2018	2019	2020
DRAM 1/2 Pitch (nm) (contacted)	26	24	21.9	20.0	18.4	16.9	15.5
MPU/ASIC Metal 1/2 Pitch (nm) (contacted)	32	32	28.3	25.3	22.5	20.0	17.9
Flash 1/2 Pitch (nm)	17	15	14.2	13.0	11.9	11.9	11.9

1.2 Reactive ion etching of fluorocarbon plasma

Figure 1.3 shows an illustration of a fluorocarbon-based plasma etching. Fluorocarbon gases such as CF_4 are introduced to the plasma reactor together with rare gases (Ar, He, etc.) and addition gases (O_2 , N_2 , H_2 , etc.). Plasmas have been generated with the power of excitation frequencies from 13.56 MHz to 2.45 GHz. Radicals, ions, and electrons are generated by the electron impact dissociation of the feed gas. The species are generated by complicated chemical reactions in the plasmas, such as dissociation, excitation, ionization, recombination, elastic scattering, charge transfer, and so on. An excited state of the species can decay to lower energy state by emission of a photon.

The plasma provides radicals, ions, and electrons onto the wafer surface. The radicals diffuse thermally onto the wafer surface since they are electrically neutral. On the other hand, the ions are accelerated perpendicularly to the wafer surface by the sheath field on the wafer and then bombard the wafer surface ^[5]. In common case of the high-density plasma etching, the ion bombardment is enhanced by applying RF bias power to the wafer. Generally, the RF-bias frequency is chosen from a few hundred kHz to 13.56 MHz. One of the advantages of the plasma etching is its anisotropic etching characteristic. As ions perpendicularly bombard the wafer surface, the activation of chemical reaction takes place only on the bottom of the pattern, and not on the sidewall. As a result, the radicals contribute to etch the bottom and deposit to form a fluorocarbon polymer layer on the sidewall, which prevents the sidewall from being etched. Ion energy distribution strongly depends on the frequency of the bias. The radicals and ions react on the surface, and the byproducts are emitted to the plasma region. The byproducts are exhausted together with other products from the plasma by a pump system.

It is believed that CF_x ($x=1-3$) radicals work as precursors of the selective etching of SiO_2 films. CF_x ($x=1-3$) radicals etch the surface film, if the wafer surface is activated

by the ion bombardment with high energies ^[6-9]. On the contrary, the CF_x ($x=1-3$) radicals work as precursors of the deposition of fluorocarbon polymers, if the surface is insufficiently activated by the ion bombardment with low energies ^[7]. Thus, the etching process using fluorocarbon plasmas proceeds in competition with the polymer deposition on the wafer surface.^[10-15] The formation of the fluorocarbon polymer strongly depends on plasma chemistry, that is, the selection of feed gases considerably influences the selectivity. The rare gases and addition gases are introduced in order to control the behaviors of ions and radicals in the plasma, and to control the polymer formation on the surface. Rare gas such as Ar plays a role to achieve a high ion/radical ratio. Addition gases such as H_2 , O_2 , and N_2 molecules increase the chemical reaction rate in the plasma and on the surface. When H_2 gas is added to the fluorocarbon plasma, fluorocarbon radicals is generated with not only electron impact dissociation, but also F abstraction by H atoms.^[16] For the Additions of O_2 and N_2 gases, they are known to play a role to suppress the excess deposition of polymers on the surface. O atoms are easy to associate with fluorocarbon radicals, and to decrease the density of fluorocarbon radicals in the plasma.^[17] However, behaviors of fluorocarbon radicals in the N_2 addition plasma have not been understood enough. The temperature of radicals and neutral molecules is one of the most important parameters for understanding and controlling the plasma process, because the temperature governs the density profiles, the transport of radicals, the reaction rate on the surface, and so on.

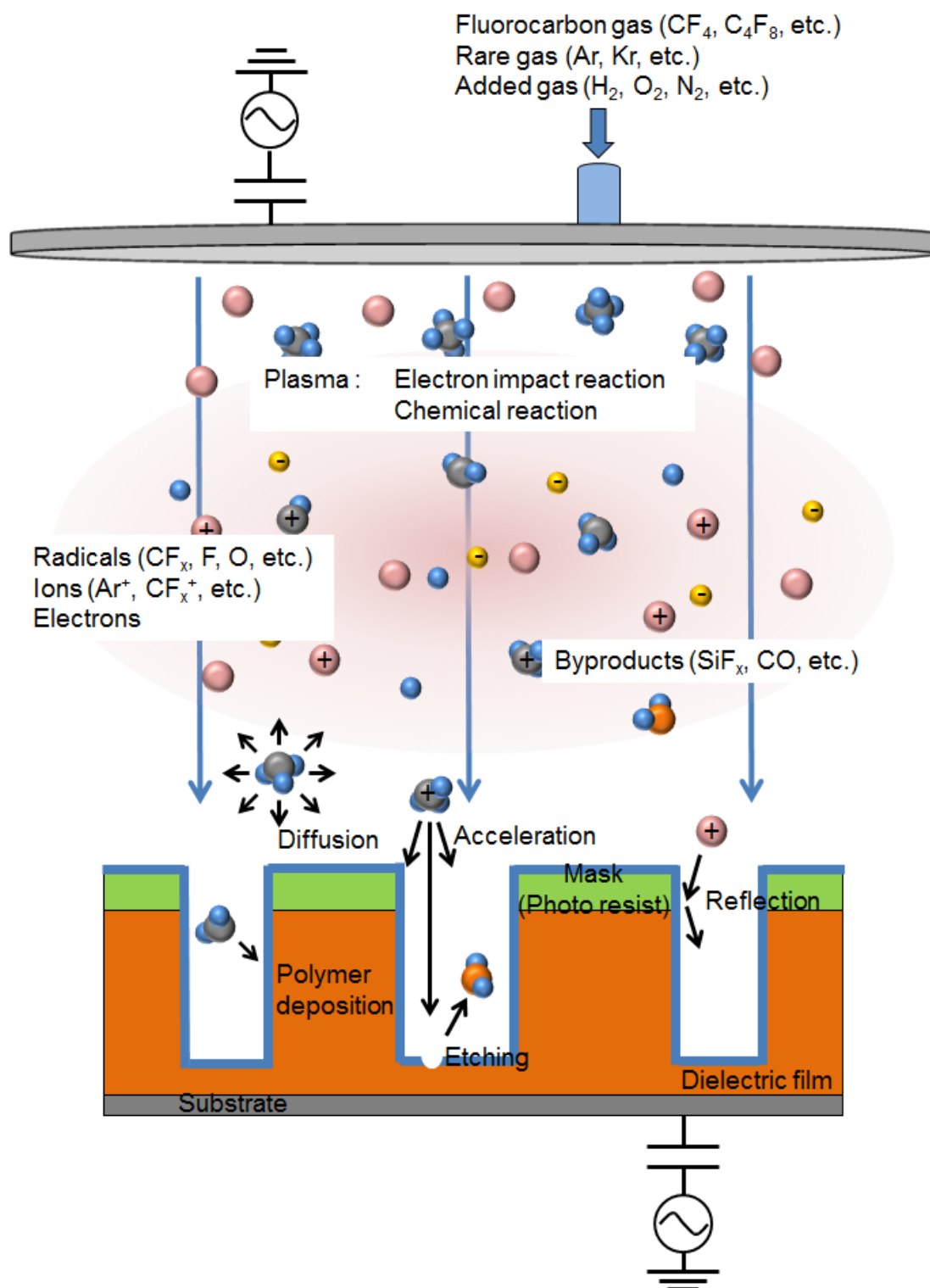


Fig. 1.3 Fluorocarbon-based plasma etching

1.3 Problems for dielectric film etching processes

Etching processes for dielectric films are important processes in fabricating the contact hole and trench. As technology nodes are progressed, the process window for the plasma process is more tight and difficult. For example, the error of the dimension of dielectric films after etch is allowed only under 10% as fabrication size.

One of problems in the etching process with high-density plasmas is poor etching selectivity of a dielectric film over photo resist (PR) and underlying materials. This is due to poor protection films deposited on the surface. The selective deposition on PR and underlying materials decreases their etch rate, and therefore increases the selectivity. However, excessive amounts of the CF_x ($x=1-3$) radicals result in the deposition on dielectric films as well, which cause an etching stop and taper shape ^[20].

Other problem is the etch rate uniformity. In the case of a 200 mm wafer, it is said that uniformity of less than 3 %, within a diameter of 195 mm, is required ^[21]. Recently, semiconductor industries demand large-area etching of a 300 mm wafer. Non-uniformity causes excess discharge times to etch dielectric films over the underlying materials. One of the mechanisms of etching non-uniformity is non-uniform distribution of ions, radicals, and electric field over the wafer ^[21, 22]. Koshiishi et. al. reported that the improvement of the electric field enable us to control a etch rate distribution ^[21]. Diagnostics of CF_x ($x=1-3$) radicals and active species are useful to understand the poor selectivity and etching non-uniformity.

High-aspect-ratio SiO_2 contact-hole etching is one of the key technologies. However, there are many serious problems, such as charge-buildup damage ^[23-25], etching-stop ^[26], and micro-loading effects ^[26]. Charge accumulation in contact hole during etching is one of the main causes of these problems. It is well known that fluorocarbon polymers deposited on the sidewall influence on the etching characteristics and charge accumulation.

Micro-trench is another problem observed in the dielectric etching. The formation of micro-trench during the etching of dielectric films is often explained by two reasons, that is, ion scattering from sloped sidewalls ^[27-29], and different charging at the sidewalls and bottom of the contact hole due to a difference in the angular distribution for positive ions and electrons.^[30,31] It is important to understand the mechanism of the problem and to monitor the plasma using plasma diagnostics. Moreover, it is important to control active species working for etch reactions in plasma, and it is necessary that good condition of plasma is assumed and kept from the understood mechanism of the problem. One solution is plasma simulation. The behaviors of active species are simulated on the computer. Then the composition of active species in plasma is fixed by controlling some conditions of plasma generation using simulation results. For these control, it is necessary that the dissociation reaction of feedstock gas is understood. In addition, it is necessary to select the feedstock gas whose dissociation reaction can be controlled.

1.4 Development and selection of feedstock gas molecule

The active species in plasma effecting etch process are strongly reflected by the feedstock gas molecule because the feedstock gas molecule is source of the active species. Therefore various fluorocarbon gases of molecules are developed and have been used for etching processes.

For process gas, the fluorocarbon molecules with straight chain structure (such as C_2F_6 , C_3F_6 , C_4F_6 , and C_3F_8), and the fluorocarbon molecules with circular structure (such as $c-C_4F_8$ and $c-C_5F_8$) have been considered and investigated^[32-35]. In the contained atom ratio, these gas have lower F/C ratio than CF_4 , a basic fluorocarbon. They were expected to realize a high selectivity process because lower F/C ratio molecule can produce less F atoms in plasma and could enhance the polymerization working for protection films. In other way than modifying molecular structure, it is considered extra elements are contained. For example, hydrogen contained fluorocarbons such as CH_xF_{4-x} ($x=1,2,3$) have been used for etching processes.^[36-39] Iodine contained fluorocarbons such as CF_3I and C_3F_7I ^[40-42], and oxygen contained fluorocarbons such as $C_5F_{10}O$ (Perfluoro- propyl-vinyl-ether)^[43,44], C_3HF_7O (Tetrafluoro-ethyl-Trifluoromethyl-ether)^[45] and C_3F_6O (Perfluoro-propen- oxide)^[46] were reported for etching process gas. However, dissociation reaction of these molecules is not understood sufficiently, except conventional molecules such as CF_4 , CHF_3 , C_2F_6 , C_3F_8 and $c-C_4F_8$ ^[47-50]. Especially, dissociation reactions of molecules containing extra elements have not been investigated.

However, these development and selection of feedstock gas have been performed by trial-and-error method. It is required that the knowledge of the dissociation reaction of gas molecule, the composition of active species in plasma and the properties of etch process are fed back to gas design.

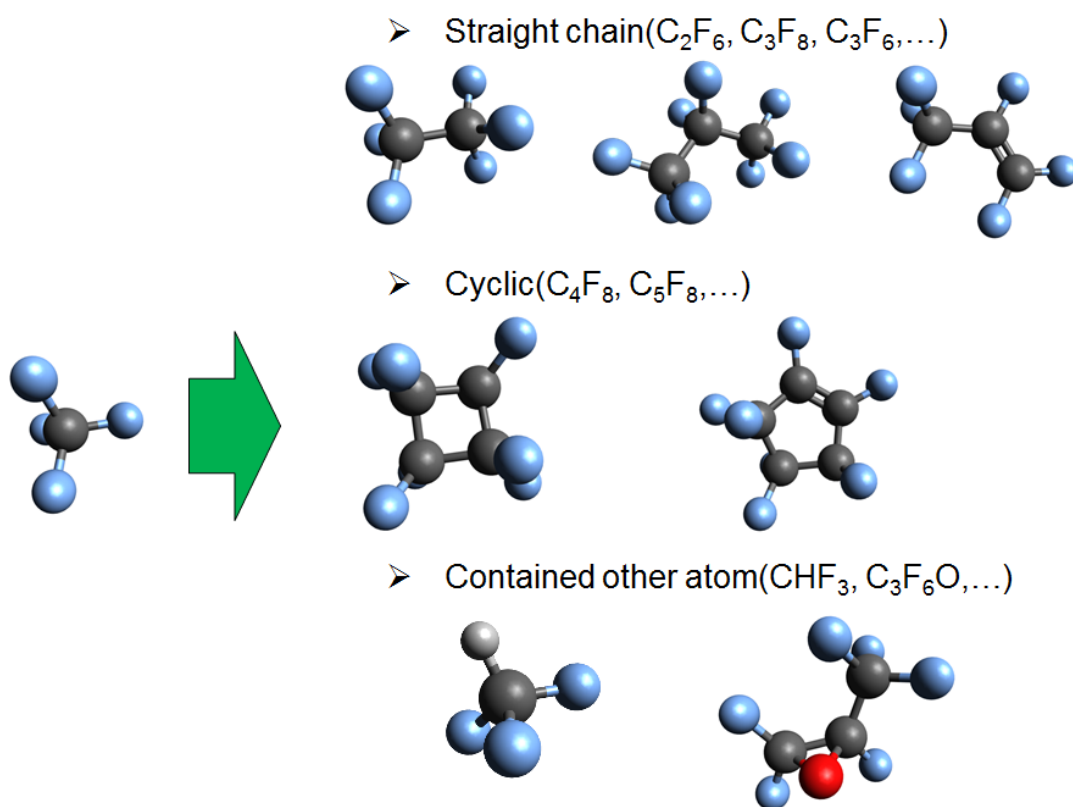


Fig. 1.4 Development of fluorocarbon gas molecule

1.5 Purposes and Construction of this thesis

The goal of this study is to understand the dissociation reaction of fluorocarbon gas molecule and control active species in plasma by controlling molecular dissociation, and feed back the results of dissociation and plasma diagnostics to gas design. In order to achieve this goal, perfluoro-vinyl-ether and hydro-fluorocarbon molecule were used and investigated. These molecules contain other atom (not fluorine or carbon) and the high etch performances such as high selectivity expected and reported. These molecular dissociation reactions were clarified by measurement and computation method. Ions and radicals densities in plasma were measured to clarify the mechanisms of molecular dissociation in plasma, and active species control, and etching.

In Chapter 2, theory of plasma diagnostics of mass spectrometry and computation method of molecular orbital calculations used for investigation of molecular dissociation were introduced. Theories of film characterization techniques such as X-ray photoelectron spectroscopy (XPS) and optical interferometer used as measurement methods of etched subsurface reactions were also described.

In Chapter 3, the dissociation reactions of two perfluoro-vinyl-ether molecules, perfluoro-ethyl-vinyl-ether (C_3F_6O) and perfluoro-propyl-vinyl-ether ($C_5F_{10}O$), induced by electron were described. These molecular fragmentation were measured by mass spectrometry and considered the mechanism using the results of molecular orbital calculations.

In Chapter 4, the dissociation reactions of hydro-fluorocarbon molecules induced by electron were described. Especially, the inconsistency between the tendencies of dissociation reactions of CH_2F_2 and the ions density in CH_2F_2 plasma was focused. To solve this inconsistency, some pathway of generating considered ions were investigated and the selective dissociation reaction at specific bond was appeared. Then the possibility of control of ions ratio using this selective dissociation was shown.

Chapter 1

Finally, the results in the present study were summarized and future works were described in the Chapter 5.

1.6 References

- [1] G. E. Moore: Electronics, **38** (1965).
- [2] R. H. Dennard, F. H. Gaensslen, H. N. Yu, V. L. Rideout, E. Bassous, and A. R. LeBlanc: IEEE J. Solid-State Circuits, **9** (1974) 256.
- [3] Intel Core TM i7-980X processor Extreme Edition,
<http://ark.intel.com/products/47932/intel-core-i7-980x-processor-extreme-edition>.
- [4] Intern. Technol. Roadmap for Semicond. (Semicond. Indust. Associat., 2013).
- [5] T. Namura, H. Okada, Y. Naitoh, Y. Todokoro, and M. Inoue: Jpn. J. Appl. Phys. **29** (1990) 2251.
- [6] D. L. Flamm, V. M. Donnelly, and D. E. Ibbotson: J. Vac. Sci. & Tec. B, **1** (1983) 23.
- [7] G. S. Oehrlein, Y. Zhang, D. Vender, and M. Haverlag: J. Vac. Sci. & Tec. A, **12** (1994) 323.
- [8] T. Sikola, D. G. Armour, and A. V. Berg: J. Vac. Sci. & Tec. A, **14** (1996) 3156.
- [9] T. Shirafugi, W. W. Stoffels, H. Moriguchi, and K. Tachibana: J. Vac. Sci. & Tec. A, **15** (1997) 209.
- [10] T. Akimoto, S. Furuoya, K. Harasima, and E. Ikawa: Jpn. J. Appl. Phys. **33** (1994) 2151.
- [11] C. Cardinaud, and G. Turban: Appl. Surface Sci. **45** (1990) 109.
- [12] S. Fang, C. Chiang, D. Fraser, B. Lee, P. Keswick, M. Chang, and K. Fung: J. Vac. Sci. & Tec. A, **14** (1996) 1092.
- [13] G. E. Potter, G. H. Morrison, P. K. Charvat, and A. L. Ruoff: J. Vac. Sci. & Tec. B, **10** (1992) 2398.

- [14] T. Akimoto, H. Nanbu, and E. Ikawa: J. Vac. Sci. & Tec. B, **13** (1995) 2390.
- [15] K. H. R. Kirmse, A. E. Wendt, S. B. Disch, J. Z. Wu, I. C. Abraham, J. A. Meyer, R. A. Breun, and R. C. Woods: J. Vac. Sci. & Tec. A, **13** (1995) 877.
- [16] H. Doh, J. Kim, S. Lee, and K. Whang: J. Vac. Sci. & Tec. A, **14** (1996) 2827.
- [17] K. Takahashi, M. Hori, and T. Goto: J. Vac. Sci. & Tec. A, **14** (1996) 2004.
- [18] R. C. Reid, J. M. Prausnitz, and T. K. Sherwood: The Properties of Gases and Liquids (McGraw-Hill, New York, 1977).
- [19] B. Chapmann: Glow Discharge Processes, Sputtering and Plasma Etching (Wiley, New York, 1980).
- [20] S. B. Kim, D. G. Choi, T. E. Hong, T. S. Park, D. S. Kim, Y. W. Song, and C. I. Kim: J. Vac. Sci. & Tec. A, **23** (2005) 953.
- [21] A. Koshiishi, Y. Araki, S. Himori and T. Iijima: Jpn. J. Appl. Phys. **40** (2001) 6613.
- [22] S. Yun and G. R. Tynan: J. Appl. Phys. **89** (2001) 911.
- [23] T. Nozawa and T. Kinoshita: Jpn. J. Appl. Phys. **34** (1995) 2107.
- [24] T. Kinoshita, M. Hane, and J. P. Mavittée: J. Vac. Sci. & Tec. B, **14** (1996) 560.
- [25] H. Ootera: Jpn. J. Appl. Phys. **33** (1993) 6109.
- [26] S. Samukawa and T. Mukai: J. Vac. Sci. & Tec. B, **18** (2000) 166.
- [27] S. V. Nguyen, D. Dobuzinski, S. R. Stiffler and G. Chrisman: J. Electrochem. Soc. **138** (1991) 1112.
- [28] T. J. Dalton, J. C. Arnold, H. H. Sawin, S. Swan, and D. Corliss: J. Electrochem. Soc. **140** (1993) 2395.
- [29] A. C. Westerheim, A. H. Labum, J. H. Dublash, J. C. Arnold, H. H. Sawin, and V. Y. Wang: J. Vac. Sci. & Tec. A, **13** (1995) 853.

- [30] J. C. Arnold, and H. H. Sawin: J. Appl. Phys. **70** (1991) 5314.
- [31] M. Schaeplens, and G. S. Oehrlein: Appl. Phys. Lett. **72** (1998) 1293.
- [32] Y. Feurprier, Y. Chinzei, M. Ogata, T. Kikuchi, M. Ozawa, T. Ichiki, and Y. Horiike: J. Vac. Sci. & Tec. A, **17** (1999) 1556.
- [33] R. Chatterjee, S. Karecki, R. Reif, T. Sparks, V. Vartanian, and B. Goolsby: J. Electrochem. Soc. **148** (2001) G721.
- [34] M. Nakamura, M. Hori, T. Goto, M. Ito, and N. Isii: J. Vac. Sci. & Tec. A, **19** (2001) 2134.
- [35] R. Chatterjee, S. Karecki, R. Reif, V. Vartanian, and T. Sparks: J. Electrochem. Soc. **149** (2002) G276.
- [36] M. Schaepkens, T. E. F. M. Standaert, N. R. Rueger, P. G. M. Sebel, G. S. Oehrlein, and J. M. Cook: J. Vac. Sci. & Tec. A, **17** (1999) 26.
- [37] B. S. Kwon, J. H. Lee, and N. E. Lee: Thin Solid Films, **519** (2011) 6741.
- [38] K. Miyata, M. Hori, and T. Goto: J. Vac. Sci. & Tec. A, **14** (1996) 2343.
- [39] A. M. Barklund, and H. O. Blom: J. Vac. Sci. & Tec. A, **11** (1993) 1226.
- [40] S. Karecki, L. Pruette, R. Reif, T. Sparks, L. Beu, and V. Vartanian: J. Vac. Sci. & Tec. A, **16** (1998) 2722.
- [41] S. Karecki, R. Chatterjee, L. Pruette, R. Reif, V. Vartanian, T. Sparks, and L. Beu: J. Vac. Sci. & Tec. B, **19** (2001) 1306.
- [42] S. Karecki, R. Chatterjee, L. Pruette, R. Reif, V. Vartanian, T. Sparks, L. Beu, and K. Novoselov: J. Vac. Sci. & Tec. B, **19** (2001) 1269.
- [43] M. Nagai, T. Hayashi, and M. Hori: Jpn. J. Appl. Phys. **45** (2006) 7100.
- [44] Y. Miyawaki, E. Shibata, Y. Kondo, K. Takeda, H. Kondo, K. Ishikawa, H. Okamoto, M. Sekine, and M. Hori: Jpn. J. Appl. Phys. **52** (2013) 020204.

- [45] Y. Chinzei, Y. Feurprier, M. Ozawa, T. Kikuchi, K. Horioka, T. Ichiki, and Y. Horiike: J. Vac. Sci. & Tec. A, **18** (2000) 158.
- [46] F. Fracassi, R. D'agostino, A. Fornelli and T. Shirafuji: Jpn. J. Appl. Phys. **41** (2002) 6287.
- [47] H. Hayashi, S. Morishita, T. Tatsumi, Y. Hikosaka, S. Noda, H. Nakagawa, S. Kobayashi, Masami Inoue, and T. Hoshino: J. Vac. Sci. & Tec. A, **17** (1999) 2557.
- [48] L. G. Christophorou, and J. K. Olthoff: J. Phys. Chem. Ref. Data. **28** (1999) 967.
- [49] H. Toyoda, M. Ito, and H. Sugai: Jpn. J. Appl. Phys. **36** (1997) 3730.
- [50] M. Goto, K. Nakamura, H. Toyoda, and H. Sugai: Jpn. J. Appl. Phys. **33** (1994) 3602.

Chapter 2 Experimental and simulation methods

2.1 Quadrupole Mass Spectrometer

Quadrupole mass spectrometer (QMS) is widely used for the analysis in many fields. Mass spectrometry is the detection method for ions by ionizing the object species and selecting the ions by the ratio of the mass to the ionic charge (m/z). Figure 2.2 (a) shows the schematic diagram of construction of QMS. The object species are ionized in the ionization chamber. Applying the voltage superposing the high frequency on the direct current voltage [$\pm(U + V \cos \omega t)$] to the four electrodes, the only ions of specific m/z oscillate stably in the quadrupole electrodes because those amplitude are getting large as the ions travel in the electrodes. Then, ions can be selected by m/z . Varying the high frequency voltage V with keeping U/V constant, the ions of M/Z enter the detector by following equation:

$$M/Z = C \frac{V}{r_0^2 f^2} \quad (2.1)$$

where C , r_0 , and f are the constant, the distance from the center to the surface of the electrodes, and the frequency, respectively. Secondary electrons by the ions through the quadrupole electrodes are amplified in a secondary electron multiplier (SEM). The mass spectrometer (Hiden EQP) with an orifice of 100 μm in a diameter was attached to the wall. The inside of the mass spectrometer was differentially pumped by a turbo molecular pump. The ionic or neutral species in the plasma introduced from the chamber into the mass spectrometer through the orifice. To neutral species were ionized in the ionization chamber by and electron beam from an oxide-coated iridium filament. The inside of the mass spectrometer was differentially pumped by 50 l/s turbo-molecular pump.

Generally the sensitivity of QMS detection depends on mass to charge ratio (m/z).

Therefore the measured intensity is corrected by mass sensitivity to know the true difference between signals of different (m/z). Figure 2.1 shows the intensities of He, Ne, Ar, Kr and Xe measured by QMS used in this studies. From the result, the efficiency depended on $(m/z)^{-0.84}$ for the species mass to charge ratio (m/z). For comparison, the mass-dependent calibrations were $(m/z)^{-0.85}$ for the HIDEN PSM2 reported by Pulpytel *et al.*,^[1] $(m/z)^{-0.81 \sim -1}$ for the HIDEN PIC reported by Singh *et al.*,^[2] $(m/z)^{-0.75}$ for HIDEN EQP 300 reported by Kechkar *et al.*,^[3] and the regression curve for Pfeiffer PPM 422 by Sode *et al.*^[4]

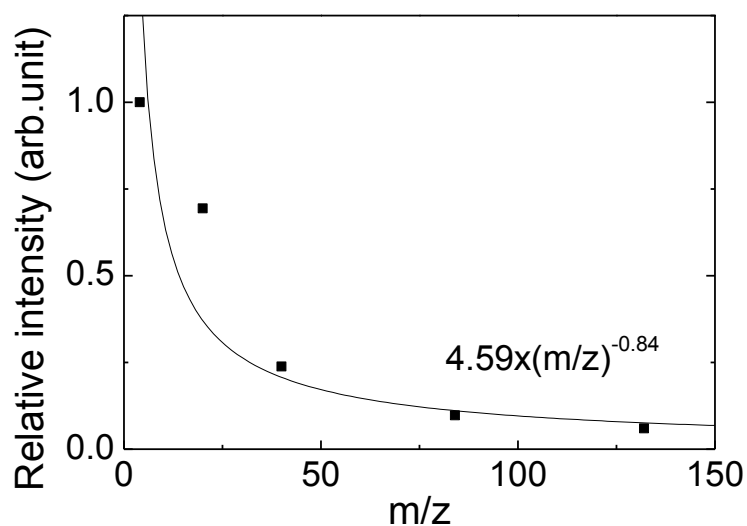


Fig. 2.1 Mass sensitivity of QMS used in this studies

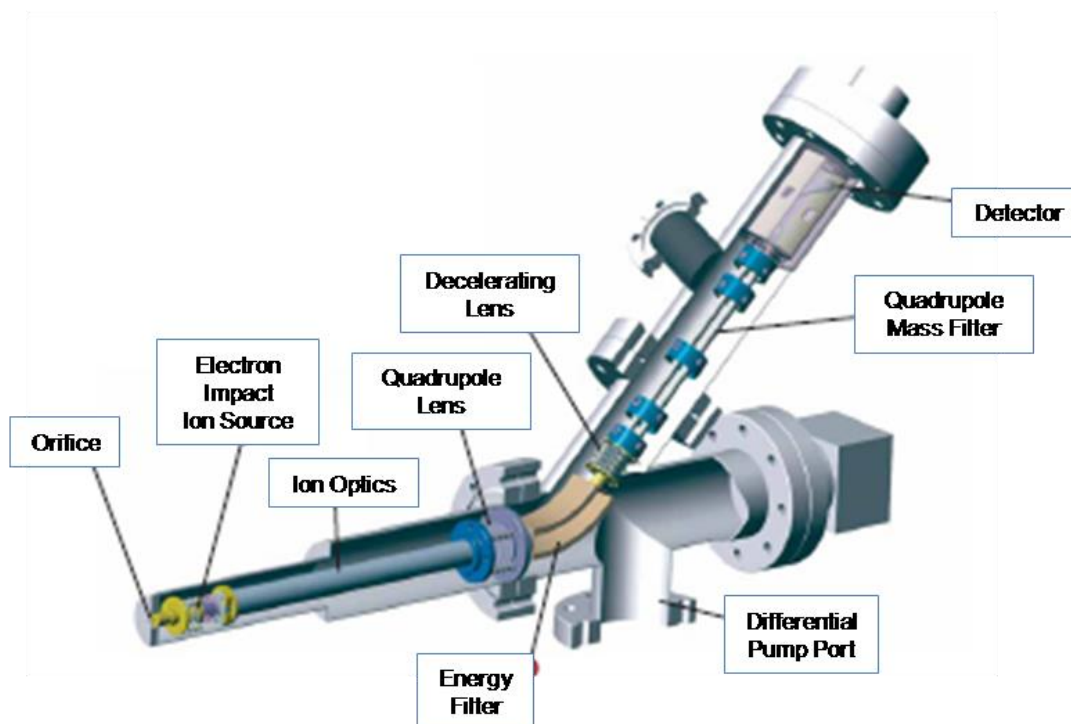
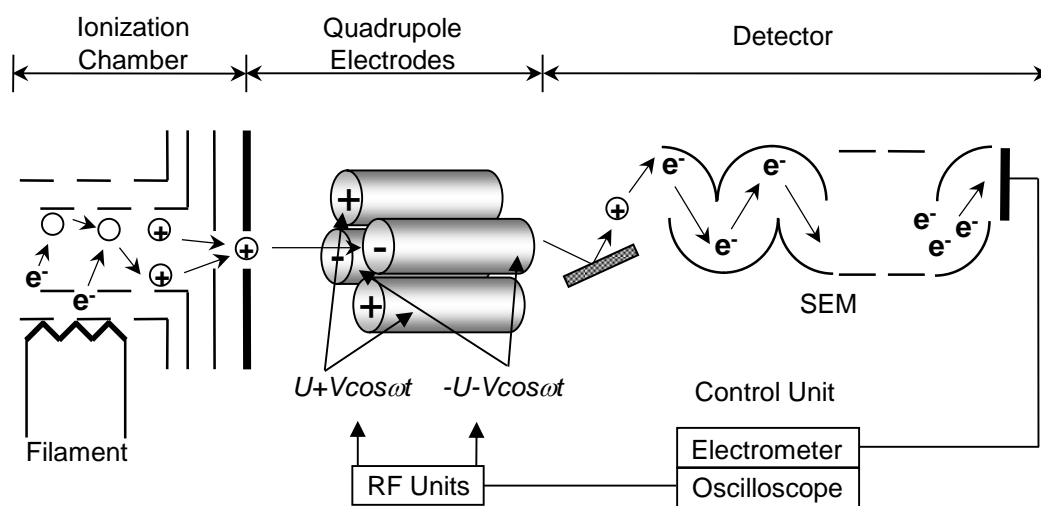


Fig. 2.2 (a) Schematic of configuration



(b)

Fig. 2.2 (b) Schematic of the principle of QMS

2.2 Plasma Absorption Probe (PAP)

Many methods have been used to measure the electron density, but they are usually not suitable for monitoring commercial processes in industrial reactors or even in research reactors. For example, Langmuir probes are usable in rare-gas discharges. In many industrial applications using reactive gases, however, insulating layers are formed on the probes, causing them to fail. In such depositing conditions, a microwave interferometer technique is available; however, it gives us only the line-averaged electron densities. Another useful technique is the plasma oscillation method^[5-8] where a weak electron beam excites electrostatic waves oscillating at the electron plasma frequency. A disadvantage here is the use of a hot filament as the electron beam source: the filament has a short lifetime and induces contamination of heavy metals in plasma reactors.

It is possible to use the PAP in measuring the electron density in a space- and time-resolved manner.^[9,10] The PAP is fully covered with quartz; thus, reactor contamination is minimized and insulating layer deposition on the probe is unimportant. Figure 2.3 shows the schematic of PAP. A PAP was constructed from a dielectric tube and a coaxial cable. The coaxial cable was enclosed by a quartz tube (dielectric constant $\varepsilon = 3.78$). This quartz tube probe was inserted through the chamber-wall to the center of the chamber. A 50 Ω semi-rigid coaxial cable of 3 mm outer diameter can be moved in the tube. A 5 mm lead of the center conductor (1 mm diameter) of the cable acts as a monopole antenna for radiating electromagnetic waves, to which a frequency-swept signal of 1 mW is fed from a network analyzer (Agilent E5071C). The network analyzer is conventionally used for measuring rf impedances and the power reflection coefficient which is defined as the ratio of the reflected power to the incident in a frequency range $\omega/2\pi = 0.1 \text{ MHz} - 8 \text{ GHz}$. Let the power reflection coefficient without plasma be $\Gamma_0 = \rho_0 \exp(i\theta_0)$, the coefficient with plasma be $\Gamma_p = \rho_p \exp(i\theta_p)$, and their ratio be $\Gamma = \Gamma_p/\Gamma_0$. The network analyzer displays the frequency dependence with the value of

$\log|\Gamma| = \log\rho_p - \log\rho_0$, thus subtracting the spurious signals ρ_0 .

From the plasma dispersion relationship, the surface wave resonance frequency f_{sw} is proportional to the square-root of the plasma density, n_e . Thus, the plasma density was estimated by the following relation,

$$n_e = 1.24 \times 10^{10} (1 + \varepsilon) f_{sw}^2 \quad (2.2)$$

where f_{sw} is $\omega_{sw}/2\pi$ in units of GHz. ε is 3.78 because the deposited film on the quartz tube is sufficiently negligibly thin. The proportional constant given here strongly depends on the probe geometric arrangement.

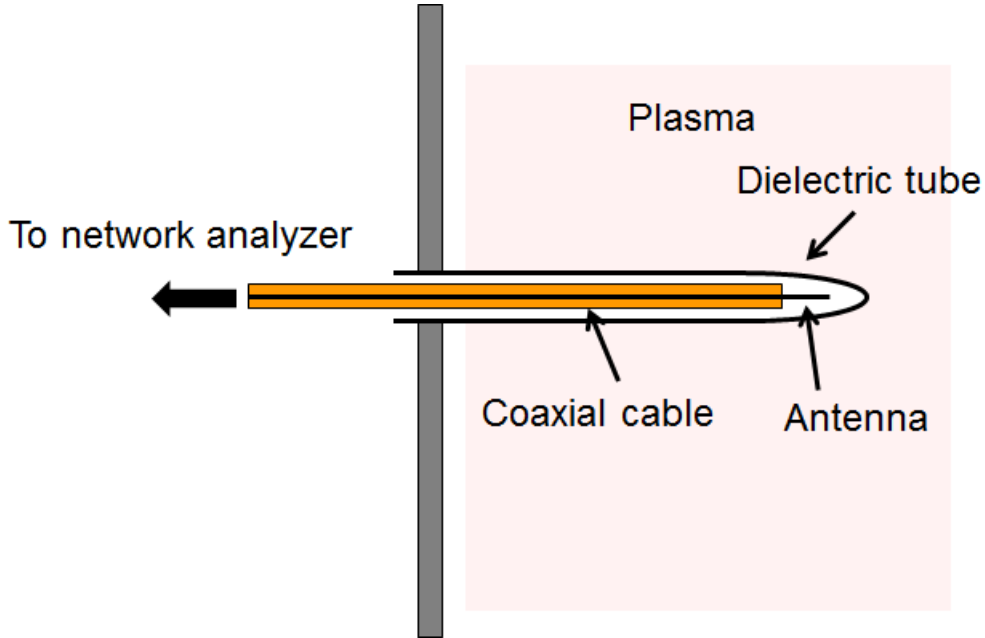


Fig. 2.3 Schematic of Plasma Absorption Probe

2.3 Optical Interferometer

Optical interferometer is one of the methods for measurement of film thickness. It can perform non-destructive and non-contact measurement unlike a profilometer and a scanning electron microscopy. The most fundamental principle used for measurement of film thickness by using interference of light is Peak-to-Valley method. Figure 2.4 shows schematic of light path during the film thickness measurement. Incident light is reflected at the top of target film (air/film) and the bottom (film/substrate). These reflected lights cause interference each other. The intensity of mixture of reflected lights increases when the optical phases of reflected lights match each other, and in the contrary case decreases. Peak-to-Valley method uses this interference pattern to calculate the film thickness.

As shown in Figure 2.4, light reflected at bottom goes through film twice. The difference of length of light path between lights reflected bottom and top is represented as $2nd$, with n and d are density and thickness of the target film, respectively. Thus, thickness d can be calculated with known density n from measured interference pattern.

Generally intensity of light going through material decreases depending on an extinction coefficient k . The decrease of the intensity non-related to interference make measurement difficult, thus, near infrared light, which is not absorbed in the film, is generally employed for optical interferometer.

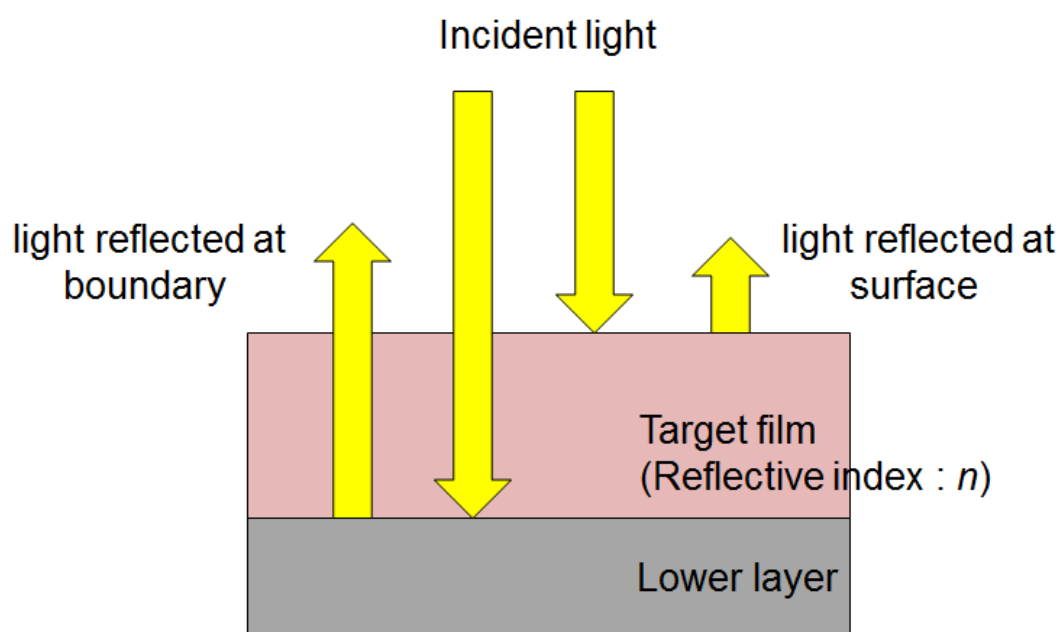
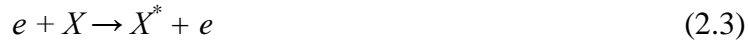


Fig. 2.4 Schematic of light pass irradiated to the film on the substrate.

2.4 Optical Emission Spectroscopy

Many optical emissions originating from excited species (e.g. atomic and molecular radicals) are generally observed in the plasma. Specific species is identified by the photon energy of the optical emission. Excited species are generated by various processes such as electron collision, dissociation, impact of other excited species, photon absorption, etc. Generally, excitation by electron impact frequently occurs in the plasma. Electron impact excitation of the ground state is given by



where X is the species of interest. De-excitation is followed by the emission of a photon from the excited state as,



The intensity of the optical emission due to the transition from an excited state to the ground state is given by

$$I_x \propto n_e n_x \int \sigma(\varepsilon) \nu(\varepsilon) f_e(\varepsilon) d\varepsilon = k_w n_e n_x \quad (2.5)$$

where n_e is the electron density, n_x is the concentration of X , $\sigma_X(\varepsilon)$ is the collision cross section for the electron impact excitation of X as a function of electron energy ε , $\nu(\varepsilon)$ is the electron velocity and $f_e(\varepsilon)$ is the electron energy distribution function (EEDF). $k_e X(\varepsilon)$ is the excitation rate coefficient for X^* by the electron impact on X . Under the condition where $k_e X$ and n_e are kept constant, the emission intensity is proportional to the concentration of species. However, both of them are affected by the experimental conditions and are generally so difficult to be kept constant when external parameters, such as input power, working pressure, are varied in the plasma processing. Thereby, optical emission spectroscopy (OES) technique is widely used as a monitoring tool in various plasma processes. Moreover, in order to compare those emission intensities with the concentration of species, it is necessary to assume that emissions from excited states chosen are proportional to the concentration of the

same species in the ground state. Therefore, the special technique such as actinometric optical emission spectroscopy (AOES) is frequently applied to estimate relative concentration of species in the ground state ^[11-17].

Optical emission spectra are generally measured by using a spectrometer. Usually, a monochromator with a photomultiplier tube (PMT) and multi-channel spectrometer with a charged coupled device (CCD) array are used. In a monochromator the light intensity is detected through the exit slit by PMT, as shown in Figure 2.5(a). On the other hand, in a multi-channel spectrometer the light intensity is detected by each pixel of CCD, as shown in Figure 2.5(b). The advantage of the multi-channel spectrometer is that it can measure a wide range (several ten nm) of wavelength simultaneously; however, the defect of the multi-channel spectrometer is that the resolution is restricted by the size of the pixel of CCD. The resolution of spectrometer sometimes limits the accuracy of measurements.

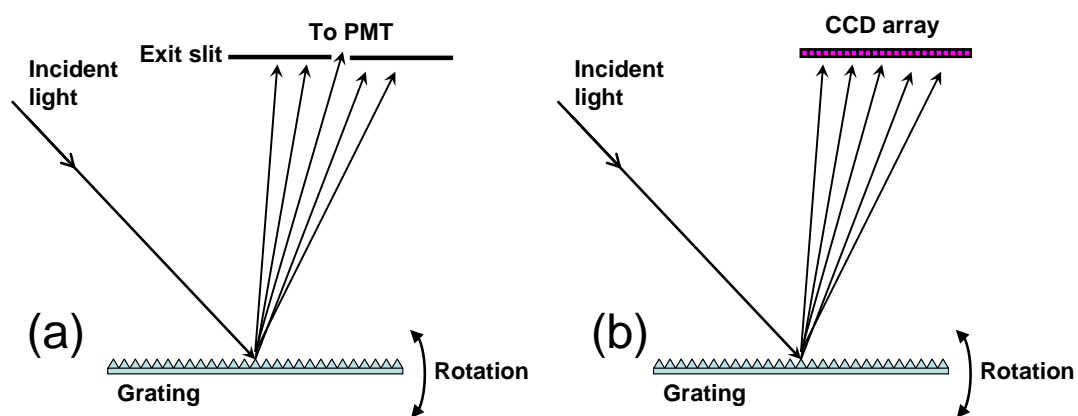


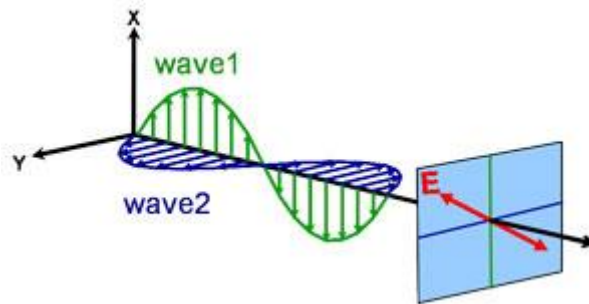
Fig. 2.5 The schematic illustration of (a) monochromator and
(b) multi-channel spectrometer.

2.5 Spectroscopic Ellipsometry^[18]

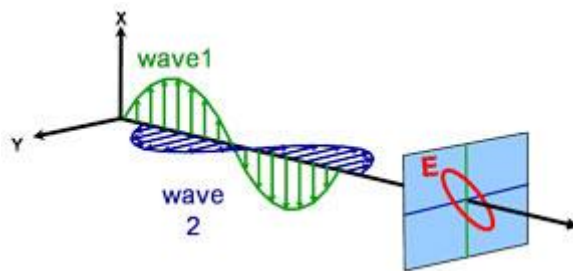
Ellipsometry is a truly powerful technique of interest and use to physicists, chemists, electrochemists, electrical and chemical engineers. Ellipsometry measures a change in polarization as light reflects or transmits from a material structure. The polarization change is represented as an amplitude ratio, Ψ , and the phase difference, Δ . The measured response depends on optical properties and thickness of individual materials. Thus, ellipsometry is primarily used to determine film thickness and optical constants. However, it is also applied to characterize composition, crystallinity, roughness, doping concentration, and other material properties associated with a change in optical response. Since the 1960s, as ellipsometry developed to provide the sensitivity necessary to measure nanometer-scale layers used in microelectronics, interest in ellipsometry has grown steadily. Today, the range of its applications has spread to the basic research in physical sciences, semiconductor and data storage solutions, flat panel display, communication, biosensor, and optical coating industries.

Ellipsometry measures the interaction between light and material. Light can be described as an electromagnetic wave traveling through space. For purposes of ellipsometry, it is adequate to discuss the waves's electric field behavior in space and time, also known as polarization. The electric field of a wave is always orthogonal to the propagation direction. Therefore, a wave traveling along the z-direction can be described by its x- and y- components. When the light has completely random orientation and phase, it is considered unpolarized. For ellipsometry, however, we are interested in the kind of electric field that follows a specific path and traces out a distinct shape at any point. This is known as polarized light. When two orthogonal light waves are in-phase, the resulting light will be linearly polarized (Figure 2.6 (a)). The relative amplitudes determine the resulting orientation. If the orthogonal waves are 90° out-of-phase and equal in amplitude, the resultant light is circularly polarized (Figure

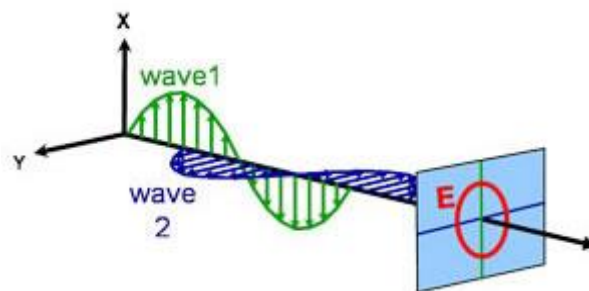
2.6 (b)). The most common polarization is “elliptical”, one that combines orthogonal waves of arbitrary amplitude and phase (Figure 2.6 (c)).



(a)



(b)



(c)

Fig. 2.6 Orthogonal waves combined to demonstrate polarization:

(a) linear, (b) circular and (c) elliptical.

Maxwell's equations must remain satisfied when light interacts with a material, which leads to boundary conditions at the interface. Incident light will reflect and refract at the interface, as shown in Figure 2.7. The angle between the incident ray and sample normal (θ_i) will be equal to the reflected angle, (θ_r). Light entering the material is refracted at an angle (θ_t) given by:

$$n_0 \sin(\theta_i) = n_i \sin(\theta_t) \quad (2.6)$$

The same occurs at each interface where a portion of light reflects and the remainder transmits at the refracted angle. This is illustrated in Figure 2.8. The boundary conditions provide different solutions for electric fields parallel and perpendicular to the sample surface. Therefore, light can be separated into orthogonal components with relation to the plane of incidence. Electric fields parallel and perpendicular to the plane of incidence are considered p- and s- polarized, respectively. These two components are independent and can be calculated separately. Fresnel described the amount of light reflected and transmitted at an interface between materials:

$$r_s = \left(\frac{E_{or}}{E_{oi}} \right)_s = \frac{n_i \cos(\theta_i) - n_t \cos(\theta_t)}{n_i \cos(\theta_i) + n_t \cos(\theta_t)} \quad (2.7)$$

$$r_p = \left(\frac{E_{or}}{E_{oi}} \right)_p = \frac{n_t \cos(\theta_i) - n_i \cos(\theta_t)}{n_i \cos(\theta_t) + n_t \cos(\theta_i)} \quad (2.8)$$

$$t_s = \left(\frac{E_{ot}}{E_{oi}} \right)_s = \frac{2n_i \cos(\theta_i)}{n_i \cos(\theta_i) + n_t \cos(\theta_t)} \quad (2.9)$$

$$t_p = \left(\frac{E_{ot}}{E_{oi}} \right)_p = \frac{2n_i \cos(\theta_i)}{n_i \cos(\theta_t) + n_t \cos(\theta_i)} \quad (2.10)$$

Thin film and multilayer structures involve multiple interfaces, with Fresnel reflection and transmission coefficients applicable at each. It is important to track the relative phase of each light component to determine correctly the overall reflected or transmitted beam. For this purpose, we define the film phase thickness as:

$$\beta = 2\pi \left(\frac{t_1}{\lambda} \right) n_1 \cos(\Phi_1) \quad (2.11)$$

The superposition of multiple light waves introduces interference that depends on the relative phase of each light wave. Figure 2.7 illustrates the combination of light waves in the reflected beam and their corresponding Fresnel calculations.

Ellipsometry is primarily interested in how p - and s - components change upon reflection or transmission in relation to each other. In this manner, the reference beam is part of the experiment. A known polarization is reflected or transmitted from the sample and the output polarization is measured. The change in polarization is the ellipsometry measurement, commonly written as,

$$\rho = \tan(\psi) e^{i\Delta} \quad (2.12)$$

A sample ellipsometry measurement is shown in Figure 2.9. The incident light is linear with both p - and s - components. The reflected light has undergone amplitude and phase changes for both p - and s - polarized light, and ellipsometry measures their changes.

The film thickness is determined by interference between light reflecting from the surface and light traveling through the film. Depending on the relative phase of the rejoining light to the surface reflection, interference can be defined as constructive or destructive. The interference involves both amplitude and phase information. The phase information from Δ is very sensitive to films down to sub-monolayer thickness. Ellipsometry is typically used for films whose thickness ranges from sub-nanometers to a few microns. As films become thicker than several tens of microns, interference oscillations become increasingly difficult to resolve, except with longer infrared wavelengths. Other characterization techniques are preferred in this case. Thickness measurements also require that a portion of the light travel through the entire film and return to the surface. If the material absorbs light, thickness measurements by optical instruments will be limited to thin, semi-opaque layers. This limitation can be circumvented by targeting measurements to a spectral region with lower absorption. For

example, an organic film may strongly absorb UV and IR light, but remain transparent at mid-visible wavelengths. For metals, which strongly absorb at all wavelengths, the maximum layer for thickness determination is typically about 100 nm.

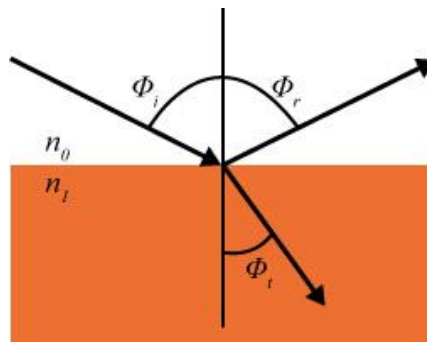


Fig. 2.7 Light reflects and refracts according to Snell's law

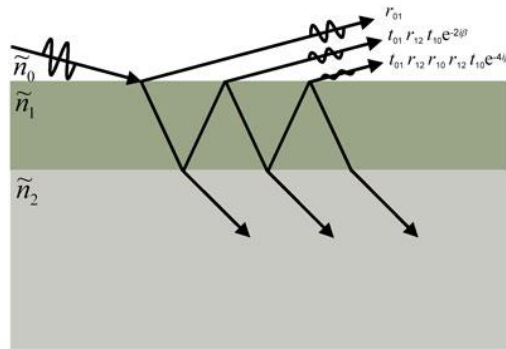


Fig. 2.8 Light reflects and refracts at each interface, which leads to multiple beams in a thin film. Interference between beams depends on relative phase and amplitude of the electric fields. Fresnel reflection and transmission coefficients can be used to calculate the response from each contributing beam.

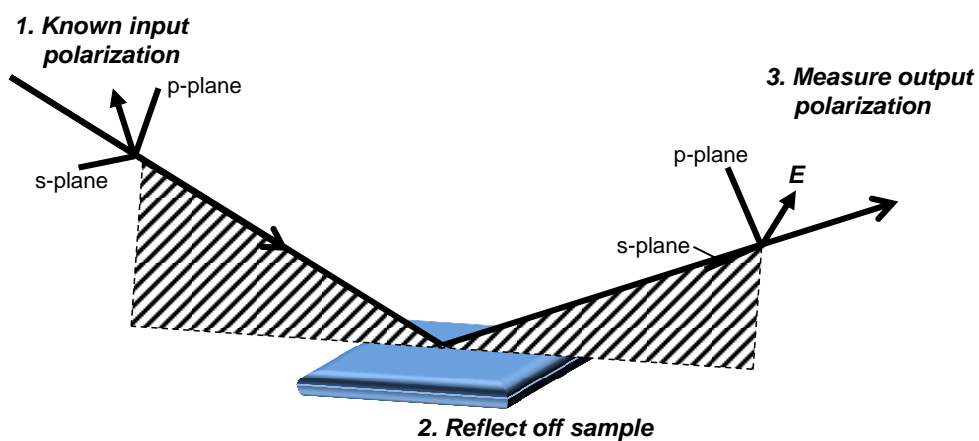


Fig. 2.9 Typical ellipsometry configuration, where linearly polarized light is reflected from the sample surface and the polarization change is measured to determine the sample response.

2.6 Molecular Orbital Calculations

Molecular orbital calculations^[19,20] have developed and can simulate molecular properties easily. Thus, the phenomena in plasma can be understood by calculations.

Molecular orbital calculations are categorized calculation based on Hartree Fock (HF) method and density function theory (DFT) based on potential functional. DFT uses the potential functional expressed an electron density instead of the wave function. Therefore calculation time of electron conditions in multielectron system is short. Kohn and Shan^[21] propounded the method calculating lower energy and its molecular orbital under variation principle for the interaction potential of electron which is functional of electron density. Then chemical properties and solid properties could be calculated quantitatively. B3LYP, which was proposed Becke^[22], is functional method using exchange integral of HF method, relative functional of Lee Yang and Parr^[23], exchange functional and other 3 parameters determined to fit molecular and atomic G2 value^[24]. Using B3LYP, a molecular structure can be calculated only in a few minutes. It is seen that B3LYP calculates accurately the energy of negative ion state and ionization energy.

The universal programs for these calculations are GAMESS^[25], Gaussian^[26], MOLPRO^[27], and so on. In this study, Gaussian 03W was used.

Wave function is used in basic as linear coupling of atomic orbital of Slater form. However, the integral term of 2 electrons is calculated in a long time by difference of wave function form for main quantum number. If atomic orbital of Slater form is described Gauss function, this atomic orbital can be calculated analytically. Thus, the integral term of 2 electrons is calculated in a shorter time. Atomic orbital of Slater form cannot be described a Gauss function. So atomic orbital of Slater form is described a number of Gauss functions. STO-3G shows that atomic orbital of Slater form is described three Gauss functions. In this study, B3LYP/6-31G(d) method was used for calculation of molecular structures. This basis function shows that atomic 1s orbitals are

described 6 primitive Gauss functions for atom from Li to Ne (at second line of periodic table), and orbitals of valance electron are described 4 (3+1) primitive Gauss functions. (d) shows addition of d orbital for atom not involving H to express the polarization of atomic orbitals when atoms connect. Figure 2.10 shows the comparison of atomic 1s orbital of Slater form, STO-3G and STO-1G.

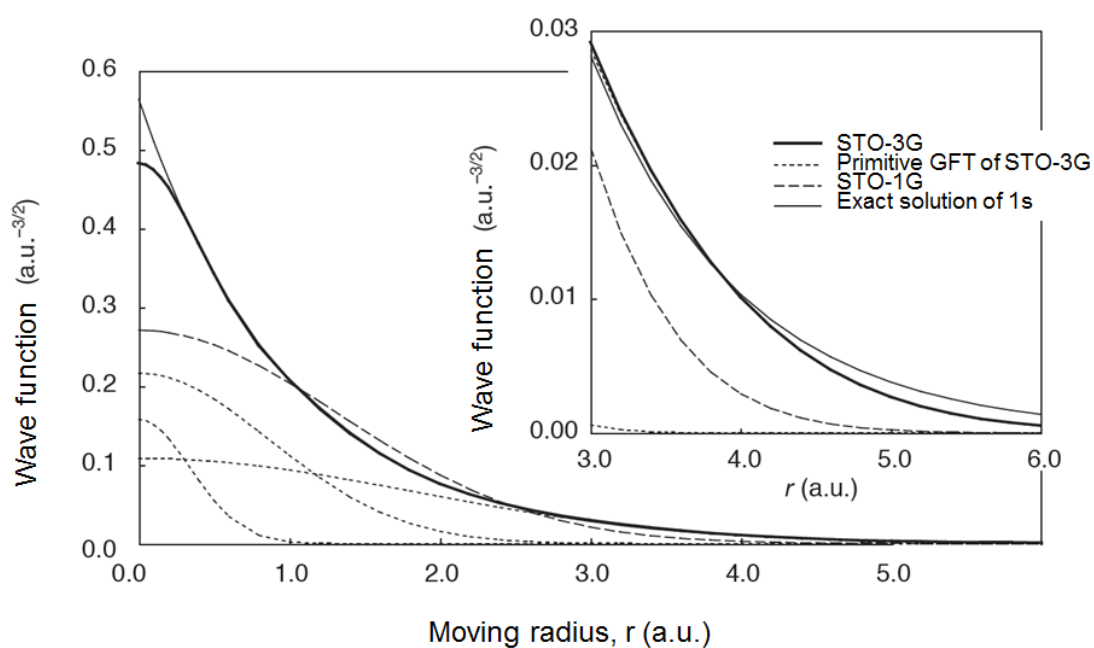


Fig. 2.10 Atomic 1s orbital of Slater form, STO-3G and STO-1G

2.6 References

- [1] J. Pulpytel, F. A. Khonsari, and W. Morscheidt: J. Phys. D: Appl. Phys. **38** (2005) 1390.
- [2] H. Singh, J. W. Coburn, and B. Graves: J. Vac. Sci. & Tec. A, **18** (2000) 299.
- [3] S. Kechkar, S. K.Babu, P. Swift, C. Gaman, S. Daniels, and M. Turner: Plasma Sources Sci. Tec. **23** (2014) 065029.
- [4] M. Sode, T. Schwarz-Selinger, and W. Jacob: J. Appl. Phys. **113** (2013) 093304.
- [5] T. Shirakawa and H. Sugai, Jpn. J. Appl. Phys. 32 5129 (1993).
- [6] T. H. Ahn, K. Nakamura and H. Sugai, Jpn. J. Appl. Phys. 34 L1405 (1995).
- [7] M. Goto, H. Toyoda, M. Kitagawa, T. Hirao and H. Sugai, Jpn. J. Appl. Phys. 36 3714 (1997).
- [8] A. Schwabedissen, E. C. Benck and J. R. Roberts, Plasma Sources Sci. Technol. 7 119 (1998).
- [9] K. Nakamura, H. Kokura, I. Ghanashev and H. Sugai, Bull. Am. Phys. Soc. 43 1416 (1998)
- [10] H. Kokura, K. Nakamura, I. P. Ghanashev and H. Sugai, Jpn. J. Appl. Phys. 38 5262 (1999)
- [11] (3)J. W. Coburn, and J. R. Roberts: J. Appl. Phys. **74** (1993) 6558.
- [12] (4)Y. Kawai, K. Sasaki, and K. Kadota, Jpn: J. Appl. Phys. **36** (1997) L1261.
- [13] (5)R. E. Walkup, K. L. Saenger, and G. S. Sewyn: J. Chem. Phys. **84** (1986) 2668.
- [14] (6)H. M. Katsch, A. Tewes, E. Quandt, A. Goehlich, T. Kawetzki, and H. F. Dobe: J. Appl. Phys. **88** (2000) 6232.
- [15] (7)S. F. Durrant, and M. A. B. Moraes: J. Vac. Sci. & Tec. A, **13** (1995) 2513.
- [16] (8)S. F. Durrant, and M. A. B. Moraes: J. Vac. Sci. & Tec. A, **16** (1998) 509.
- [17] (9)A. Gicquel, M. Chenevier, Kh. Hassouni, A. Teserepi, and M. Dubus: J. Appl. Phys. **83** (1998) 7504.

- [18] Spectroscopic Ellipsometry: Principles and Applications, H. Fujiwara, (Wiley, New York) (2007).
- [19] Introduction to Computational Chemistry, F Jensen, (John Wiley & Sons, Ltd)
- [20] T. Hayashi: J. Plasma Fusion Res. **89** (2013) 12.
- [21] W. Kohn, and L. J. Sham: Phys. Rev. **140** (1965) A1133.
- [22] A.D. Becke: J. Chem. Phys. **98** (1993) 5648.
- [23] C. Lee, W. Yang, and R. G. Parr: Phys. Rev. B, **37** (1988) 785.
- [24] L. A. Curtiss, K. Raghavachari, G. W. Trucks, and J. A. Pople: J. Chem. Phys. **94** (1991) 7221.
- [25] www.msg.ameslab.gov/gamess
- [26] www.gaussian.com/g_prod/g03.htm
- [27] www.molpro.net

Chapter 3 Mechanism of dissociation of C_3F_6O and $C_5F_{10}O$ induced by electron

3.1 Introduction

The fluorocarbon (FC) gases are extensively used as feedstock in semiconductor manufacturing. For use in plasma etching processes of these gases, much attention has recently been paid to selective CF_3^+ ion formation,^[1,2] because CF_3^+ ion shows a higher etch yield for SiO_2 at lower ion impact energies compared with CF_2^+ , CF^+ and F^+ ions.^[3,4] This property is utilized to provide rapid and selective etching of SiO_2 over Si. CF_4 feedstock gas has been conventionally used for this purpose, but the counter fragment of F atom produced by the dissociative ionization of CF_4 are believed to etch Si spontaneously,^[5] prompting the investigation of alternative gases for the selective formation of CF_3^+ ions. At present, several gases - C_3F_6 ,^[6] C_4F_6 ,^[6] C_6F_6 ,^[8] $c-C_4F_8$,^[9,10] $c-C_5F_8$, $c-C_5HF_7$,^[11] etc. - appear suited for plasma etching; our goal is to apply our knowledge of dissociation processes to design feedstock gas molecules and to control the densities of chemically reactive species such as CF_3^+ ions.

To date, there have been few reports on the use of oxygen-containing fluorocarbons. Polarization of the electronic charge density of chemical bonds, such as those to the oxygen atom, often leads to dissociation of the chemical bonds. For example, The oxygen-containing FCs such as $c-C_4F_8O$ (octafluoro-tetra-hydrofuran)^[12] and C_3HF_7O (tetrafluoro-ethyl-trifluoro-methyl-ether)^[13] using for etching processes have been reported. In particular, ether-bridging oxygen bonds should dissociate easily under dissociative ionization conditions. Both C_3H_6O ^[16-24] and C_3F_6O comprise several isomers that are characterized as ketones, aldehydes, cyclic and acrylic alcohols, and cyclic and acrylic ethers. The results of etching using the isomer hexafluoroacetone ($F_3C-C(=O)-CF_3$, CAS. 684-16-2) have been reported by Kim *et al.*,^[25] and the results

using perfluoro-propylene oxide ($\text{CF}_2\text{O-CFCF}_3$, CAS: 428-59-1) have been reported by Fracassi *et al.*^[26,27] Mass spectra for these gases have been published in the NIST chemistry WebBook.^[28] Morikawa *et al.* reported briefly mass spectra for perfluoro-methyl-vinyl-ether (PMVE, $\text{CF}_3\text{-O-CF=CF}_2$, $\text{C}_3\text{F}_6\text{O}$; CAS: 1187-93-5) forming selectively CF_3^+ ion.^[1] Nagai *et al.* and Miyawaki *et al.* reported similar structure molecule, perfluoro-propyl-vinyl-ether (PPVE, $\text{CF}_3\text{-CF}_2\text{-CF}_2\text{-O-CF=CF}_2$, $\text{C}_5\text{F}_{10}\text{O}$) also forming selectively CF_3^+ ion^[13,14]. But to our knowledge, the electron impact reactions of PMVE and PPVE have not been studied, and the ion energies for PMVE and PPVE are unknown. Moreover, PMVE and PPVE is as monomers in the formation of fluoropolymers or fluoroelastomers.^[29] The fluorinated compounds such as Teflon^R and Cytop^R are commercially produced numerous in mass by their excellence in resisting chemical attack and their very good thermal stability.^[30]

Here we investigated the electron impact reactions of PMVE and PPVE, including dissociative ionization and electron attachment. Cationic (positive) and anionic (negative) ions of PMVE and PPVE were experimentally detected using quadrupole mass spectrometry, and the experimentally-obtained dissociation products were confirmed by quantum chemical calculations. We propose that PMVE and PPVE fragments at the ether bonds.

3.2 Dissociative ionization and dissociative electron attachment

reaction of C_3F_6O

3.2.1 Experimental detail

A quadrupole mass spectrometer (QMS; Hiden Analytical, EQP) was installed in the chamber wall of the commercial plasma etching reactor, as schematically shown in Figure 3.1. The reactor can process 200 mm diameter wafers. Highly purified PMVE (purity of 99%; Asahi Glass Co.) at a flow rate of 80 sccm was introduced into the chamber through the shower head of upper electrode and maintained at a pressure of 1.5 Pa. The aperture to the QMS had a diameter of 100 μm . The pressure in the QMS was 3.2×10^{-5} Pa during measurements and 5.3×10^{-6} Pa for fully pumping-down background; under these conditions, residual gas did not affect signal measurements.

The relative abundance of positive and negative ions formed by both dissociative ionization and electron attachment to PMVE gas molecules was measured by electron impact using an energy range of 0.4 to 80 eV. The typical emission currents were measured with 200 μA for positive ion spectra or ionization efficiency curves and 20 μA for negative ion spectra. Mass dependent ion transmission was calibrated by data determined using a mixture of rare gases (He, Ne, Ar, Kr and Xe) with known partial pressures, and referred the literature cross-sections.^[31]

The cross sections for the electron impact dissociations were estimated as a function of electron energy by reference to the cross section for $\text{CF}_4 \rightarrow \text{CF}_3^+ + \text{F}$ (14.2~15.5 eV).^[2] The ionization potential for $\text{Ar} + \text{e}^- \rightarrow \text{Ar}^+ + 2 \text{e}^-$ (15.8 eV)^[31] and $\text{Kr} + \text{e}^- \rightarrow \text{Kr}^+ + 2 \text{e}^-$ (14.0 eV)^[31] was used to calibrate the ionizing energy scale for the appearance potential.

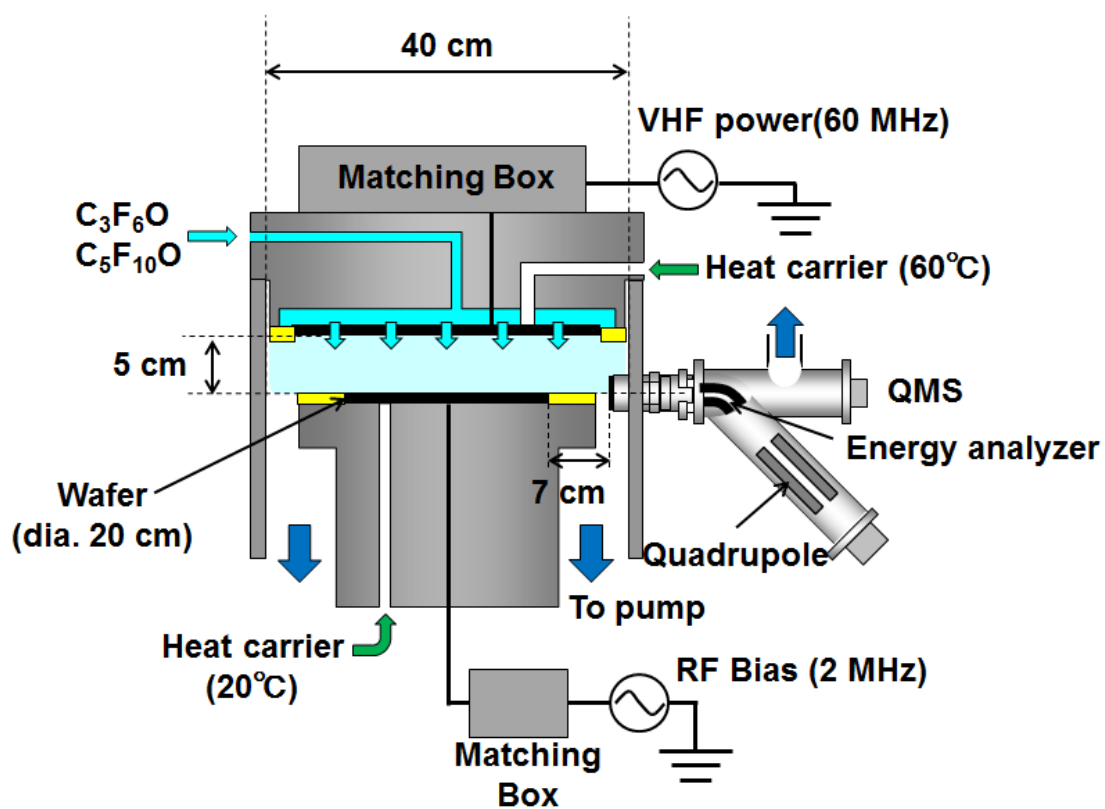


Fig. 3.1 Schematic of dual-frequency CCP reactor.

3.2.2 Cracking pattern of C₃F₆O induced by electron

Dissociative ionization of PMVE caused by impact with 70 eV electrons provided the positive-ion mass spectra shown in Figure 3.2. The observed peaks and relative abundances are tabulated in Table 3.2. Lowering the electron energy to 20 eV simplified the fragmentation pattern to two peaks: 69 m/z for CF₃⁺, 78 m/z for C₂F₂O⁺ and 166 m/z for C₃F₆O⁺. Plasma processing typically uses electron energies of several eV; consequently, using lower electron energies, close to the ionization threshold, generates the largest number of target ions. We thus focused on electron impact processes to generate CF₃⁺, and C₂F₂O⁺.

Figure 3.3 shows the ionization efficiency curves for the PMVE dissociative ionization products CF₃⁺, C₂F₂O⁺ and C₃F₆O⁺. The ionization threshold for the formation of CF₃⁺ ion was approximately 11.8 eV, in agreement with the computational results (Section 3.2.2). The signal intensity for CF₃⁺ ions gradually increased with increasing electron energy, then saturated, in common with the dissociative ionization of other fluorocarbon molecules.^[2] The signal intensity for C₂F₂O⁺ also increased with increasing electron energy, but increased abruptly in the lower energy, then saturated at higher eV. The decrease in ionization efficiency with increasing electron energy above 11.8 eV might be due to decomposition of PMVE and the liberation of F atoms. Consequently, the ionization efficiency might be maximal around the threshold energy, whereas much higher energies cause molecular decomposition. The pathways by which F atoms are liberated require further investigation. Regardless, the positive-ion mass spectra revealed a lower C₂F₂O⁺/CF₃⁺ ratio than that obtained at higher electron energy, showing that relatively few C₂F₂O⁺ ions are generated by highly energetic electron impacts.

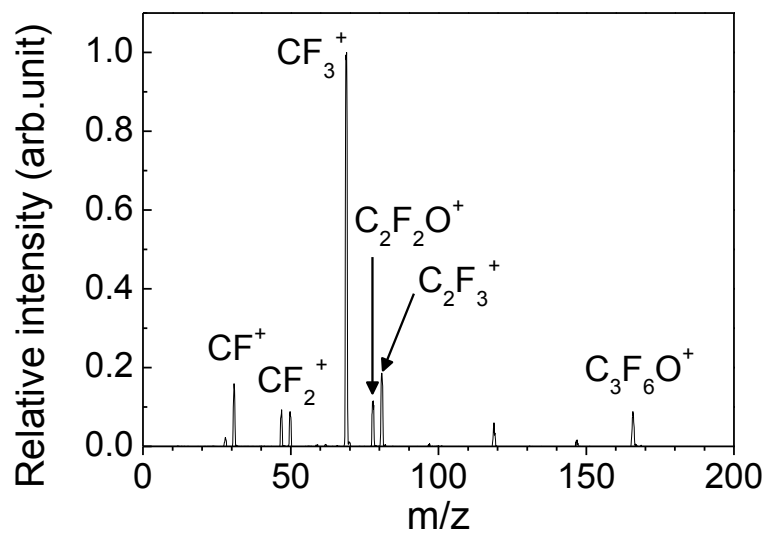


Fig. 3.2 (a) Positive ion mass spectra for PMVE obtained by electron impact at 70 eV.

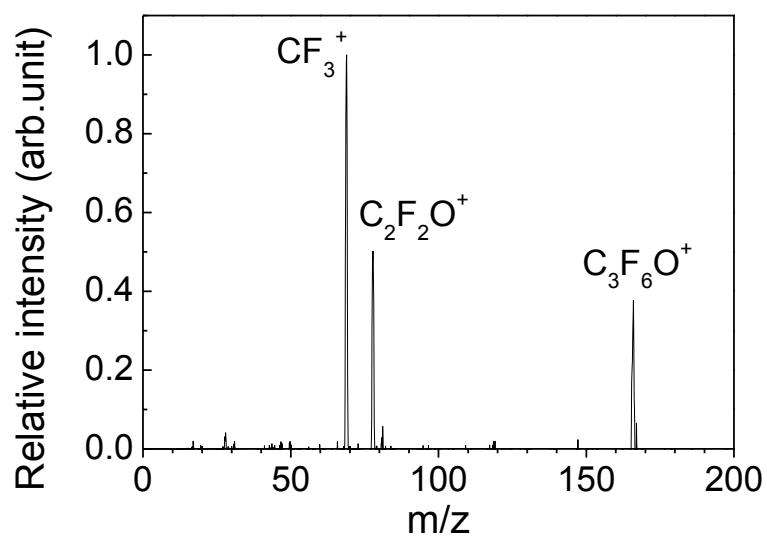


Fig. 3.2 (b) Positive ion mass spectra for PMVE obtained by electron impact at 20 eV.

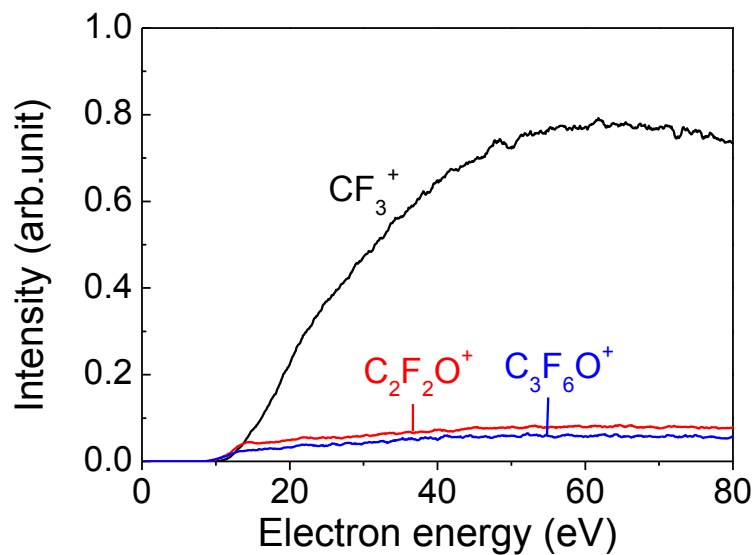


Fig. 3.3 (a) Ionization efficiency curves for the fragments CF_3^+ , $\text{C}_2\text{F}_2\text{O}^+$ and $\text{C}_3\text{F}_6\text{O}^+$ ions formed by electron impact ionization of the PMVE

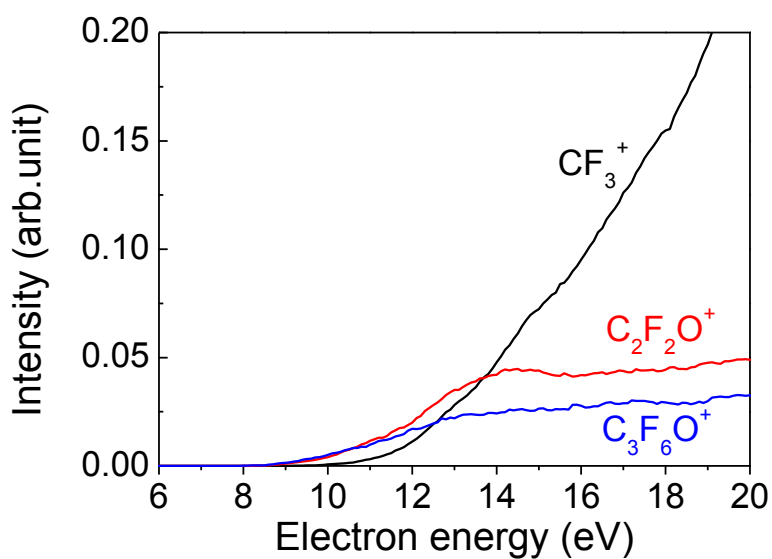


Fig. 3.3 (b) Ionization efficiency curves for the fragments CF_3^+ , $\text{C}_2\text{F}_2\text{O}^+$ and $\text{C}_3\text{F}_6\text{O}^+$ ions formed by electron impact ionization of the PMVE (enlarged view of (a))

Table 3.1. Relative abundance of identified positive ions for the dissociative ionization of PMVE measured at an electron energy of 70 eV.

m/z	Positive ions	Relative intensity
31	CF	0.002
47	COF	0.065
50	CF ₂	0.056
69	CF ₃	1.000
78	C ₂ F ₂ O	0.087
81	C ₂ F ₃	0.101
116	C ₂ F ₄ O	0.027
119	C ₂ F ₅	0.024
147	C ₃ F ₅ O	0.006
166	C ₃ F ₆ O	0.012

Figure 3.4 shows the negative-ion mass spectrum produced by dissociative electron attachment to PMVE. The most abundant negative ion was observed at 85 m/z, corresponding to CF_3O^- , and a small peak at 19 m/z corresponding to F^- was also observed. Negative ions are mostly formed by resonance attachment processes. We believe that the detected F^- is not generated by process of the resonance electron attachment of PMVE, because no obvious dissociative electron attachment with generation of F^- . Thus a secondary process maybe likely dissociated residual gases as a source of F^- .

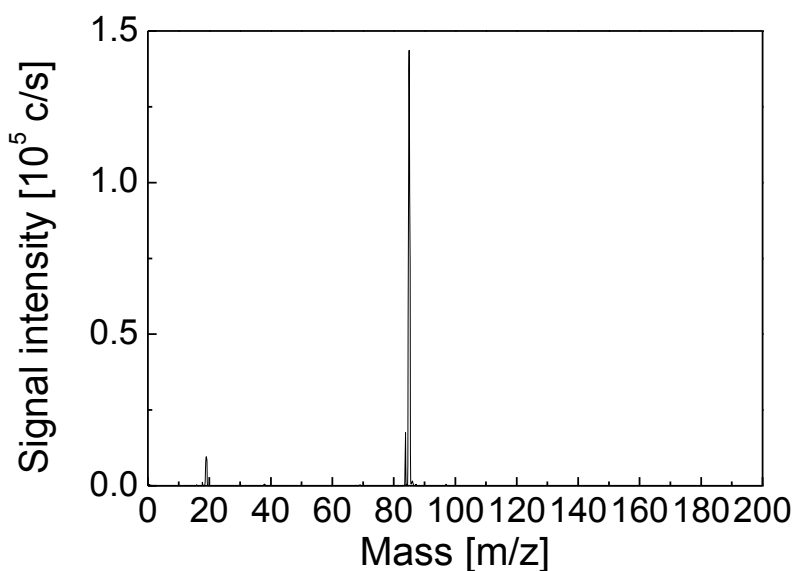


Fig. 3.4 Negative ion mass spectra for PMVE obtained by electron impact at 2.5 eV.

3.2.3 Potential curves of positive ion state and negative ion state of C₃F₆O

The dissociation channels of PMVE was studied based on density functional theory calculations using Gaussian 03W package.^[18] The grounded state, negative ion state, and ionized state potentials were calculated by using B3LYP/6-31+G(d). The most stable ground state structure of PMVE was obtained by geometrical optimizations as shown in Figure 3.5. (Structural parameters are listed in Table 3.2.) Leibold et al. reported the optimizing geometric structure for the ground state PMVE, calculated with HF/3-21G and MP2/6-31G.^[19]

Potential curves were obtained by optimizing the total energy (non-adiabatic energy) and the molecular structures at each bond length along the reaction coordinate (adiabatic energy) at each 0.1 Å using rigid scan and z-matrix scan mode (non-adiabatic energy).

Figure 3.6 shows the calculated potential curves for the CF₃-OC₂F₃ (O3-C4) coordinate for negative and positive ions and Figure 3.7 shows the corresponding curves for CF₃O-C₂F₃ (C2-O3). Black lines represent the potential curve for the ground state, while the two blue lines show the potential curves for the positive ion states. The dotted blue line represents the adiabatic potential curve calculated by assuming a rigid structure identical to the ground state structure. Electron impact instantaneously excites PMVE, vertically transitioning it from the ground state to the positive ion state, followed by a brief relaxation of the molecular structure. Another solid blue line shows non-adiabatic potential curves calculated for the relaxed structure of the positive ion state following the transition initiated by electron impact.

The total energy difference between the ground and positive ion states of PMVE is estimated to be 10.1 eV, determined from the energy minima of the adiabatic positive ion state and the ground state on the potential curves. The non-adiabatic potential curve always exhibits lower energies, and longer C-O bonds. This calculation therefore

supports the dissociative ionization of PMVE into $\text{CF}_3^+ + \text{C}_2\text{F}_3\text{O}$. In contrast, for C2-O3, the $\text{CF}_3\text{O}^+ + \text{C}_2\text{F}_3$ reaction is not dissociative because the calculated potential curve does not show a minimum as the C-O bond is lengthened, as demonstrated in Figure 3.7. Therefore, the dissociative ionization of PMVE mainly generates CF_3^+ at an ionization threshold energy of 11.2 eV, in good agreement with the experimental value of 11.8 eV obtained from Figure 3.3.

Abundant $\text{C}_2\text{F}_2\text{O}^+$ ions were experimentally observed and were likely generated by dissociative ionization of PMVE and the formation of CF_4 . Figure 3.8 shows the geometry of the positive ion state, in which the central C atom (C4) of CF_3 and the F atom (F7) of the closest ether bond are positioned proximally. Molecular vibrations may assist the formation of the bonds between C4 of CF_3 and F7. In addition, the geometry of $\text{C}_2\text{F}_2\text{O}^+$ is planar, and aligned along the C–C=O bonds. Based on these considerations, the potentials for each position along the C2–F7 bond with the 0.1 Å interval step were calculated; the results are shown in Figure 3.8. Increasing the C2–F7 bond length eventually results in the generation of CF_4 , leading to a decrease in total energy and supporting the possibility that dissociation occurs via the $\text{C}_2\text{F}_2\text{O}^+ + \text{CF}_4$ pathway. CF_4 formation was further indicated by the results obtained by moving C4 towards the F7 atom. Taken together, the summed total energy of CF_4 and $\text{C}_2\text{F}_2\text{O}^+$ is more stable than the energies obtained for CF_3^+ and $\text{C}_2\text{F}_3\text{O}$.

Alternatively, the $\text{C}_2\text{F}_2\text{O}^+$ ions could be generated by the $\text{C}_2\text{F}_3\text{O} \rightarrow \text{C}_2\text{F}_2\text{O}^+ + \text{F}$ pathway; Another possibility of direct ionization of $\text{C}_2\text{F}_2\text{O}^\bullet$; however, this reaction probably requires multiple electron impacts, which is not realistic, particularly under low pressure conditions. If occurrence of such secondary process of residual components, then the low threshold for ionizing of $\text{C}_2\text{F}_2\text{O}^\bullet$ would appear around a calculated appearance potential of relatively low 9.9 eV.

In electron impact ionization processes, energies in excess of the threshold shift $\text{CF}_3^+ + \text{C}_2\text{F}_3\text{O}$ towards $\text{CF}_4 + \text{C}_2\text{F}_2\text{O}^+$. Thus, dissociation via $\text{C}_2\text{F}_2\text{O}^+ + \text{CF}_4$ is common,

especially at energies close to the threshold. From the change in potential it can be estimated that $\text{C}_2\text{F}_2\text{O}^+$ ions are generated at energies above 11.8 eV, which is consistent with the experimentally-determined saturation energy. The experiments showed that the abundance of $\text{C}_2\text{F}_2\text{O}^+$ ions decreases at higher electron impact energies, suggesting that the formation of CF_4 by rearrangement is favorable only at low electron impact energies. High energy electron impacts tend to cause decomposition of the molecule, and not dissociation into fragments such as CF_3^+ and $\text{C}_2\text{F}_2\text{O}^+$. Consequently, the experimental observation of $\text{C}_2\text{F}_2\text{O}^+$ ions supports the CF_4 formation scheme.

Finally, Figure 3.7 shows the calculated potential curves for negative ion formation along the C atom (C2) to O atom (O3) bond. The calculated potentials for the $\text{C}_2\text{F}_3\text{O}^- + \text{CF}_3$ (Figure 3.6) and $\text{CF}_3\text{O}^- + \text{C}_2\text{F}_3$ (Figure 3.7) reactions both show dissociative curves, but the $\text{C}_3\text{F}_6\text{O} \rightarrow \text{CF}_3 + \text{C}_2\text{F}_3\text{O}^-$ reaction shown in Figure 3.6 has a potential energy barrier, whereas there is almost not barrier for the latter reaction. After vertical electronic transitions, the repulsive potential curve promotes instantaneously either with conserved kinetic energy or with lost in a three-body process. For the reason of the collisions posed under low pressure, we interpret that the former repulsive formation of CF_3O^- is more reasonable to explain the experimental result. Thus, the formation of $\text{C}_2\text{F}_3\text{O}^-$ via dissociative electron attachment is energetically favorable. The total energy difference between the ground and negative ion states of PMVE is estimated to be 3.0 eV. Moreover, in calculation using 6-311G(3df), the value is estimated to be 2.7 eV.

Easy dissociation of fluorocarbon molecules by electron attachment should produce a high abundance of F atoms due to dissociative electron attachment. However, PMVE dissociated at the C-O bond by electron attachment, a process that requires an electron energy lower than that for dissociation and ionization. Therefore, in contrast to other categories of fluorocarbon molecules, PMVE easily dissociated at the ether bond due to polarization of the charge on the bridging oxygen atom. Ionization and excitation cause structural changes centered at the ether bond, because strain is brought by strong

electronic charge polarization in order to form an energetically stable structure.

The positive and negative ions observed by mass spectrometry are in agreement with the calculated potential curves for both electron attachment and ionization. Abundant positive and negative ions were generated via the three pathways shown in Figure 3.9 at the thresholds listed in Table 3.3. All ionization processes were centered on the ether bond.

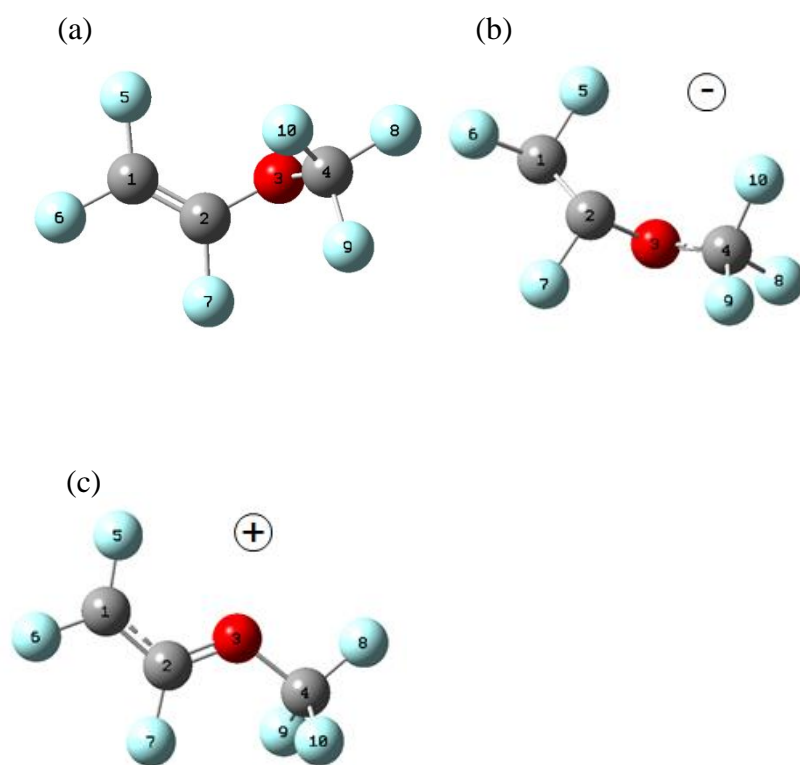
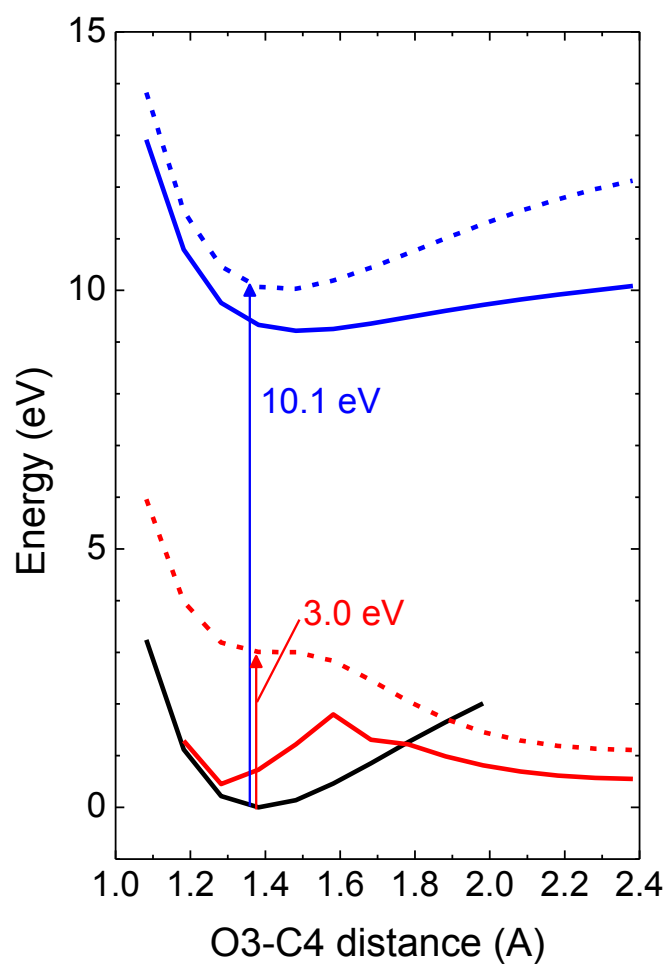


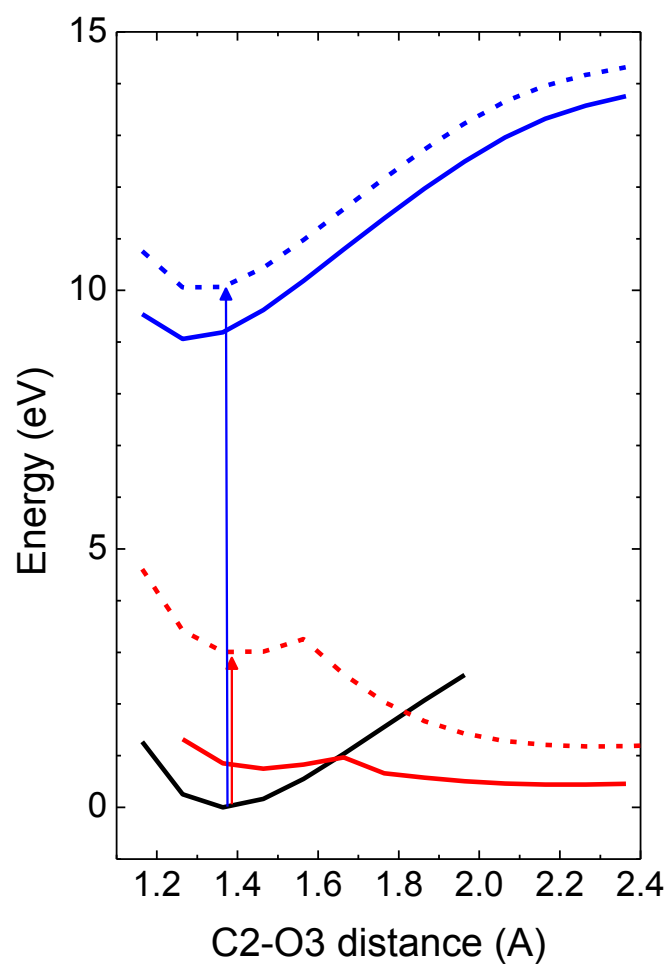
Fig. 3.5 Molecular structure of PMVE in the (a) ground state, (b) negative ion state, and (c) positive ion state. (C for 1,2,4; O for 3; and F for 5,6,7,8,9,10)

Table 3.2 Geometrical parameters for the ground state, negative ion state and ionized state of PMVE

A	B	C	D	A-B Distance (Å)	A-B-C Angle (°)	A-B-C-D Dihedral angle (°)
(a) ground state						
C2	C1			1.329349		
O3	C2	C1		1.361514	123.237572	
C4	O3	C2	C1	1.382299	117.707717	101.468755
F5	C1	C2	O3	1.322347	123.746494	-5.135022
F6	C1	C2	O3	1.322293	123.389351	174.433545
F7	C2	C1	O3	1.339675	121.049117	-173.864780
F8	C4	O3	C2	1.329692	106.899174	-179.808246
F9	C4	O3	C2	1.342240	111.986066	60.512551
F10	C4	O3	C2	1.343912	111.565858	-60.362901
(b) negative ion state						
C2	C1			1.408786		
O3	C2	C1		1.457389	109.793788	
C4	O3	C2	C1	1.322929	114.637039	127.571782
F5	C1	C2	O3	1.411705	123.234459	30.136631
F6	C1	C2	O3	1.376969	114.109588	162.163544
F7	C2	C1	O3	1.435393	117.589834	-120.900052
F8	C4	O3	C2	1.360848	108.354433	176.829452
F9	C4	O3	C2	1.358731	114.851838	58.227925
F10	C4	O3	C2	1.358578	114.631729	-64.750304

A	B	C	D	A-B Distance (Å)	A-B-C Angle (°)	A-B-C-D Dihedral angle (°)
(c) ionized state						
C2	C1			1.417268		
O3	C2	C1		1.284873	119.694518	
C4	O3	C2	C1	1.509483	122.703809	179.960734
F5	C1	C2	O3	1.279512	121.396867	-0.007672
F6	C1	C2	O3	1.280067	120.938305	179.995111
F7	C2	C1	O3	1.294462	117.909076	-179.996091
F8	C4	O3	C2	1.298116	103.575424	-179.964766
F9	C4	O3	C2	1.311258	107.411062	60.428444
F10	C4	O3	C2	1.311283	107.409493	-60.360922

Fig. 3.6 Potential curves for the CF₃-OC₂F₃

Fig. 3.7 Potential curves for the CF₃O-C₂F₃

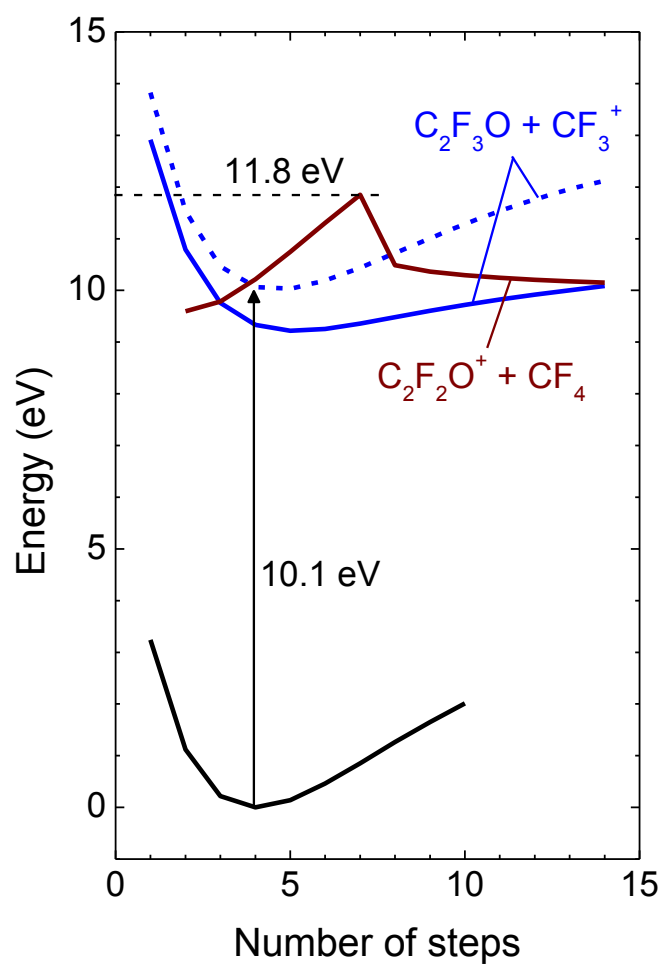


Fig. 3.8 Potential curves for the $\text{CF}_4 + \text{C}_2\text{F}_2\text{O}^+$

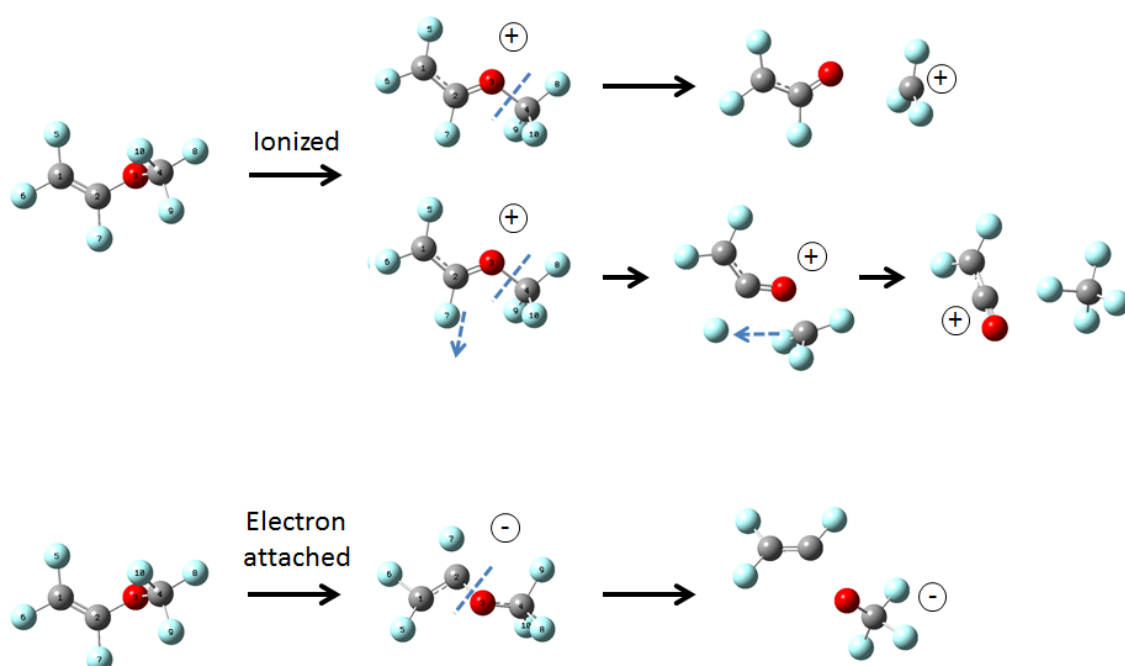


Fig. 3.9 Summary of electron impact ionization process for PMVE.

Table 3.3 Threshold for dissociative ionization reactions.

Reaction	Energy threshold (eV)	
	Experiments	Calculation
$\text{CF}_3^+ + \text{C}_2\text{F}_3\text{O}$	11.8	11.2
$\text{C}_2\text{F}_2\text{O}^+ + \text{CF}_4$	11.1	11.8
$\text{C}_2\text{F}_2\text{O} \cdot + \text{e}^- \rightarrow \text{C}_2\text{F}_2\text{O}^+$		9.9
$\text{C}_3\text{F}_6\text{O}^+$	10	10.1
$\text{CF}_3\text{O}^- + \text{C}_2\text{F}_3$	<2.5	3.0

3.3 Dissociative ionization and dissociative electron attachment

reaction of $\text{C}_5\text{F}_{10}\text{O}$

3.3.1 Experimental detail

A quadrupole mass spectrometer (QMS; Hiden Analytical, EQP) was installed in the chamber wall of the commercial plasma etching reactor (Figure 3.2). Highly purified PPVE at a flow rate of 70 sccm was introduced into the chamber and maintained at a pressure of 1.0 Pa. The aperture to the QMS had a diameter of 100 μm . The pressure in the QMS was 3.2×10^{-5} Pa during measurements and 5.3×10^{-6} Pa for fully pumped-down background; under these conditions, residual gas did not affect signal measurements.

Relative abundance of positive and negative ions formed by both dissociative ionization and electron attachment to PPVE gas molecules was measured by electron impact using an energy range of 0.4 to 80 eV. The typical emission currents were measured with 200 μA for positive ion spectra or ionization efficiency curves and 20 μA for negative ion spectra. Mass dependent ion transmission was calibrated by data determined using a mixture of rare gases (He, Ne, Ar, Kr and Xe) with known partial pressures, and referred to literature cross-sections.^[31] The extraction efficiency of the ions from the ionizer was considered to be equal, and a product of efficiency for transmission of both energy filter and mass filter and for detection at the electron multiplier. The efficiency $(m/z)^{-0.84}$ depended on the mass-to-charge ratio (m/z) of the species. The dependence agreed well with a previous report.²⁸ The ionization potentials for $\text{Ar} + e^- \rightarrow \text{Ar}^+ + 2e^-$ (15.8 eV) and $\text{Kr} + e^- \rightarrow \text{Kr}^+ + 2e^-$ (14.0 eV) were used to calibrate the ionizing energy scale for the appearance potential.

The PPVE dissociation pathways were studied by density functional theory using the Gaussian 03W package.^[18] The ground state and positive ion state potentials were calculated using B3LYP/6-31G(d) without diffuse function.

Potential curves were obtained by optimizing the total energy (non-adiabatic energy)

and the molecular structures for each bond length along the reaction coordinate (adiabatic energy) at 0.1 Å intervals using rigid scan and relax scan modes (non-adiabatic energy).

Figure 3.10 shows the most stable structure of PPVE obtained by geometrical optimization: (a) the ground state, (b) the negative ion, and (c) the positive ion. Table 3.4 shows the geometrical parameters.

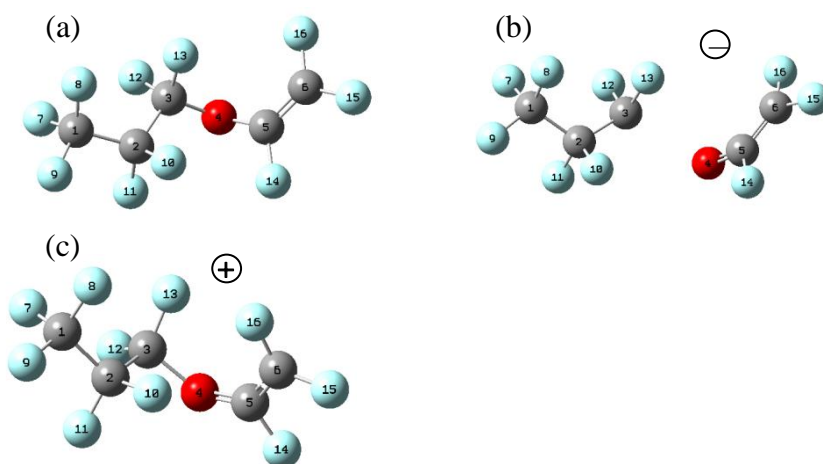


Fig. 3.10 Molecular structure of PPVE in the (a) ground state, (b) negative ion state, and (c) positive ion state (C for 1,2,3,5,6; O for 4; and F for 7,8,9,10,11,12,13,14,15,16).

Table 3.4 Geometrical parameters for the ground state, negative ion state and positive ion state of PPVE, as shown in Scheme 1.

A	B	C	D	A-B Distance (Å)	A-B-C Angle (°)	A-B-C-D Dihedral angle (°)
(a) ground state						
C2	C1			1.549197		
C3	C2	C1		1.551975	115.467238	
O4	C3	C2	C1	1.392612	112.803030	-171.117962
C5	C4	C3	O2	1.361824	118.942067	-76.798775
C6	C5	C4	O3	1.328233	122.874465	-90.443703
F7	C1	C2	C3	1.337951	110.518202	64.801811
F8	C1	C2	C3	1.339758	110.386986	-55.940110
F9	C1	C2	C3	1.338155	109.014343	-175.543531
F10	C2	C1	C3	1.355557	107.708691	120.687924
F11	C2	C1	C3	1.350362	107.865119	-121.387979
F12	C3	C2	C1	1.339298	109.342780	-53.744860
F13	C3	C2	C1	1.348858	108.772068	65.473435
F14	C5	O4	C3	1.335652	115.462036	94.226814
F15	C6	C5	O4	1.320130	123.335553	-175.742025
F16	C6	C5	O4	1.319891	123.382325	4.170318

A	B	C	D	A-B Distance (Å)	A-B-C Angle (°)	A-B-C-D Dihedral angle (°)
(b) negative ion state						
C2	C1			1.547268		
C3	C2	C1		1.508632	117.907392	
O4	C3	C2	C1	2.461147	119.007150	170.692041
C5	C4	C3	O2	1.246463	107.676821	-104.435443
C6	C5	C4	O3	1.360206	130.016834	-83.093291
F7	C1	C2	C3	1.346220	111.001875	60.782750
F8	C1	C2	C3	1.344788	110.957287	-59.316523
F9	C1	C2	C3	1.353464	111.705977	-179.330421
F10	C2	C1	C3	1.362913	105.592173	122.579280
F11	C2	C1	C3	1.367757	105.357405	-122.048738
F12	C3	C2	C1	1.365129	109.809000	-58.774933
F13	C3	C2	C1	1.358445	110.046976	60.450665
F14	C5	O4	C3	1.405205	118.745083	93.991617
F15	C6	C5	O4	1.355162	125.297002	-175.878476
F16	C6	C5	O4	1.350490	123.224036	-5.447946
(c) positive ion state						
C2	C1			1.558000		
C3	C2	C1		1.559351	113.409656	
O4	C3	C2	C1	1.494184	107.833427	168.701130
C5	C4	C3	O2	1.282846	129.943276	-73.142326
C6	C5	C4	O3	1.420087	131.205250	-12.043025
F7	C1	C2	C3	1.335447	108.597504	50.271874
F8	C1	C2	C3	1.335563	108.885688	-69.226496
F9	C1	C2	C3	1.324488	108.883722	170.557405
F10	C2	C1	C3	1.363682	108.965390	118.874649
F11	C2	C1	C3	1.335228	110.445612	-120.945314
F12	C3	C2	C1	1.305137	112.377595	-78.321851
F13	C3	C2	C1	1.323403	113.288813	49.017797
F14	C5	O4	C3	1.293139	114.366375	170.488343
F15	C6	C5	O4	1.281166	119.111775	-179.099578
F16	C6	C5	O4	1.279846	124.147207	1.880103

3.3.2 Cracking pattern of C₅F₁₀O induced by electron

Figure 3.10 shows a typical positive ion mass spectrum of the etching plasmas with feedstock mixed with PPVE. As complicated as electron collision processes are in plasmas, and despite the fact that fundamental processes are not understood comprehensively, large abundant ions were confirmed to be CF₃⁺ ions. To understand why CF₃⁺ ion was selectively formed, we studied electron-induced dissociations of PPVE both experimentally and computationally.

Figure 3.10 shows positive ion mass spectra showing the dissociative ionization of pure PPVE caused by impact with 20 eV and 70 eV electrons. Relative abundances are tabulated in Table 3.4. As shown in Figure 3.10 (a), the observed peaks at 20 eV were 69 m/z for CF₃⁺, 78 m/z for C₂F₂O⁺, 119 m/z for C₂F₅⁺, 169 m/z for C₃F₇⁺ and 266 m/z for C₅F₁₀O⁺. At the electron energy of 70 eV, the fragmentation pattern simplified for some peaks: 69 m/z for CF₃⁺ as shown in Figure 3.10(b). The largest abundant ion of CF₃⁺ is in good agreement with the previous report.^[7]

Figure 3.11 shows the ionization efficiency curves for the PPVE dissociative ionization products of CF₃⁺, C₂F₂O⁺, C₂F₅⁺, C₃F₇⁺ and C₅F₁₀O⁺. Ionization efficiency curves for the target ions are quite different. The ionization thresholds for the formation of CF₃⁺, C₂F₂O⁺, C₂F₅⁺, C₃F₇⁺ and C₅F₁₀O⁺ ions were approximately 14.5, 11.4, 16.5, 11.8 and 10.3 eV, respectively. With the exception of C₂F₅⁺, ions with larger masses appeared at lower energies. Notably, fragments by dissociation at the C=C bond, such as CF₂⁺, were not observed.

Interestingly, the C₂F₂O⁺ ion was expected to dissociate with rearrangement, since a possible counter fragment of C₃F₈ was not dissociated by direct cleavage of PPVE. As the electron energy increased, the signal intensities for C₂F₂O⁺ and C₅F₁₀O⁺ apparently saturated. This means that low excess energy for ionization is enough for rearrangement but then the fragmentation rate rapidly approaches the limit. Rearrangement

fragmentation with expulsion of $\text{C}_2\text{F}_2\text{O}^+$ ion and formation of a C_3F_8 molecule can be interpreted to be energetically favored.

Considered together with the fragmentation process, when energetic electrons collide with PPVE, the quantum states move electronically with vertical transition in accordance with the Franck-Condon principle, while bond lengths remain unaltered during ionization. This is accompanied by higher vibrational excitation. Below the energy barrier for dissociation, adiabatic ionization and the ions of $\text{C}_5\text{F}_{10}\text{O}^+$ will dissociate leading to the creation of fragmented ions. Generally, molecules containing more atoms and π -bonds are easier to ionize by means of stabilization of charges, causing removal of electrons, by delocalization and hyperconjugation.^[30] Thus, the fragment ions of CF_3^+ , C_2F_5^+ and C_3F_7^+ were dissociated at the counter C–C or C–O bond of the C=C bond. In fact, the signal intensities for CF_3^+ , C_2F_5^+ and C_3F_7^+ ions were gradually increased. This reflects that more energy can be absorbed faster than bond rupture.^[31] In particular, the signal intensity for CF_3^+ ion was almost three times larger than those for C_2F_5^+ , and C_3F_7^+ ions.

Although the electron energies of several eV was typically used in plasma etching, as seen in the mass spectrum at lower electron energies, close to the ionization threshold, the low energy electron generates CF_3^+ and the largest number of ions such as $\text{C}_2\text{F}_2\text{O}^+$, C_2F_5^+ and C_3F_7^+ .

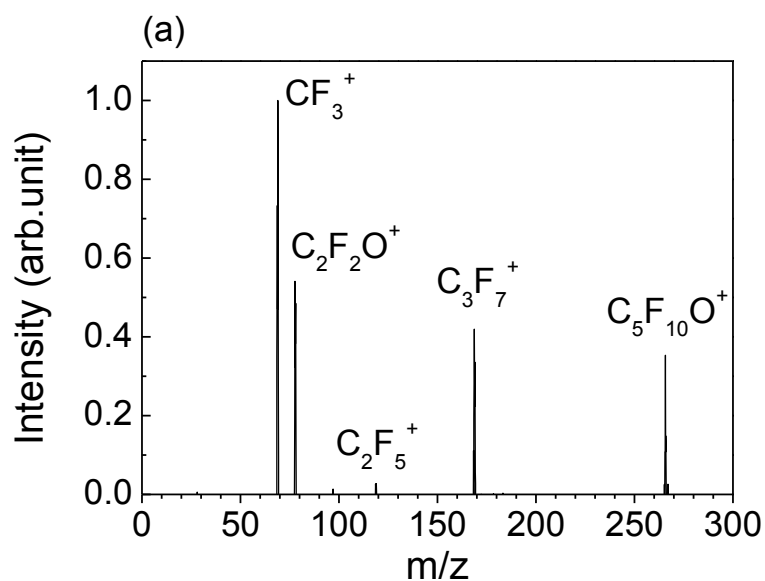


Fig. 3.10 (a) Positive ion mass spectra showing the dissociative ionization of pure PPVE obtained by electron impact at 20 eV.

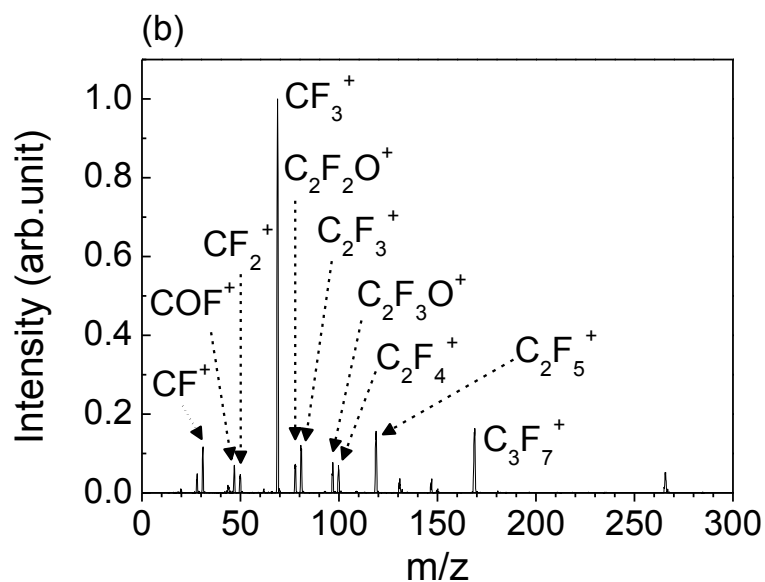


Fig. 3.10 (b) Positive ion mass spectra showing the dissociative ionization of pure PPVE obtained by electron impact at 70 eV.

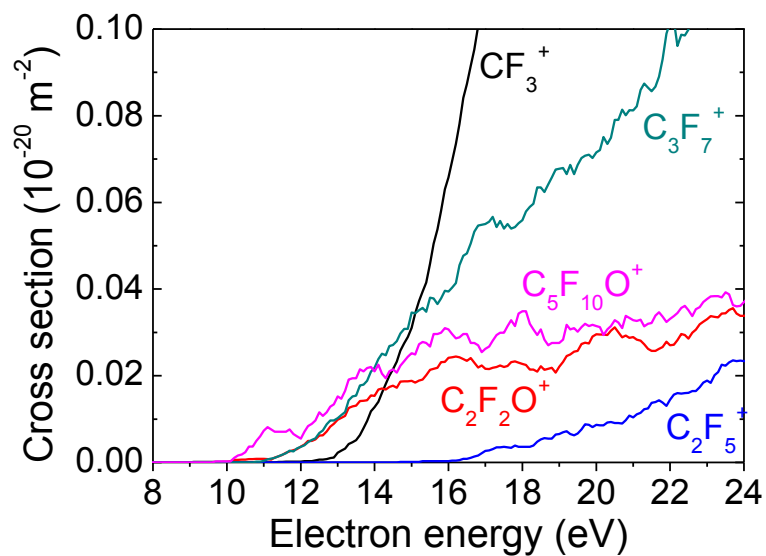


Fig. 3.11. Ionization efficiency curves for the PPVE dissociative ionization

Table 3.4. Threshold for dissociative ionization reactions.

Reaction	Energyv threshold (eV)	
	Experiments	Calculation
$\text{CF}_3^+ + \text{C}_4\text{F}_7\text{O}$	14.5	12.8
$\text{C}_2\text{F}_2\text{O}^+ + \text{C}_3\text{F}_8$	11.4	12.3
$\text{C}_2\text{F}_2\text{O}^\bullet + \text{e}^- \rightarrow \text{C}_2\text{F}_2\text{O}^+$		9.9
$\text{C}_2\text{F}_5^+ + \text{C}_3\text{F}_5\text{O}$	16.5	12.8
$\text{C}_3\text{F}_7^+ + \text{C}_2\text{F}_3\text{O}$	11.8	10.9
$\text{C}_5\text{F}_{10}\text{O}^+$	10.3	9.9
$\text{C}_3\text{F}_7\text{O}^- + \text{C}_2\text{F}_3$	2.0	2.7
$\text{C}_3\text{F}_7 + \text{C}_2\text{F}_3\text{O}^-$	2.1	2.6

Figure 3.12 shows the negative ion mass spectrum produced by dissociative electron attachment to PPVE. Negative ions were observed at 19 m/z for F^- , 97 m/z for $C_2F_3O^-$ and 185 m/z for $C_3F_7O^-$. Negative ions are mostly formed by resonance attachment processes. The C-O bonds also contribute to dissociative electron attachment reactions. Figure 3.13 shows the ionization efficiency curves for the PPVE dissociative electron attachment products $C_2F_3O^-$ and $C_3F_7O^-$. The curves of $C_2F_3O^-$ and $C_3F_7O^-$ had peaks at 2.0 and 2.1 eV, respectively. The pathways by which F atoms are liberated require further investigation.

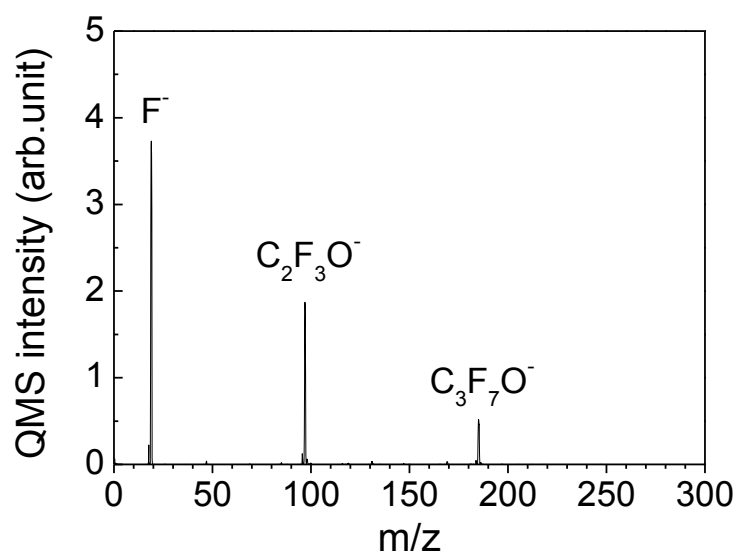


Fig 3.12. Negative ion mass spectrum produced by dissociative electron attachment to PPVE

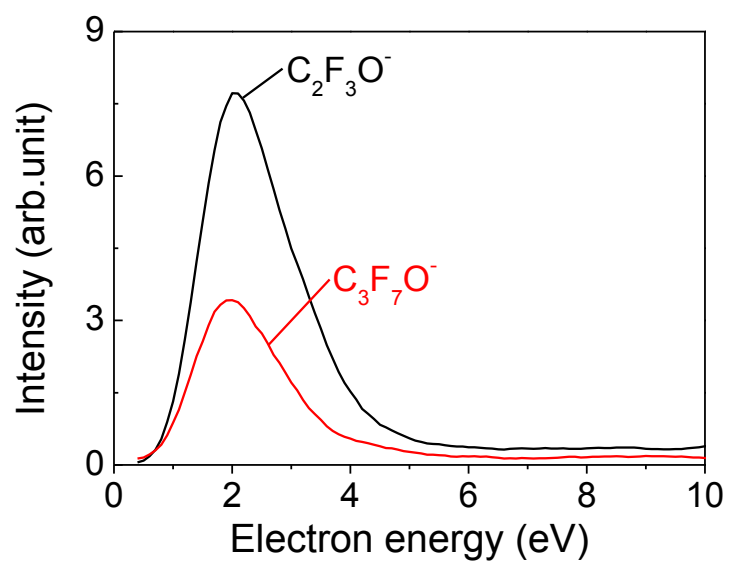


Fig 3.13. Ionization efficiency curves for the PPVE dissociative electron attachment

3.3.3 Potential curves of positive ion state and negative ion state of C₅F₁₀O

Figure 3.14 shows an energy diagram for C₅F₁₀O. The lowest dissociative ionization processes are predicted for C₂F₃O⁺ + C₃F₇ with an energy of 9.9 eV. As mentioned before, the rearrangement of C₂F₂O⁺ + C₃F₈ will occur to create a lower energy barrier and more stable C₃F₈ formation. Comparatively, an ionization process of CF₃⁺ + C₂F₄OC(F)=CF₂ requires more energy at 12.8 eV. The possible pathways for fragmentation are as follows:

CF ₃ ⁺ + C ₂ F ₄ OC(F)=CF ₂	(direct bond rupture)
C ₂ F ₅ ⁺ + CF ₂ OC(F)=CF ₂	(relatively low rate and high appearance energy)
C ₃ F ₇ ⁺ + OC(F)=CF ₂ or OC(F)=CF ₂ ⁻	(direct bond rupture or heterolytic fragmentation)
F ₂ C ₂ =CO ⁺ + C ₃ F ₈	(rearrangement)
C ₃ F ₇ O ⁻ + •C(F)=CF ₂	(electron attachment)
F ₂ C ₂ =C(F)O ⁻ + C ₃ F ₇	(electron attachment)

As listed in Table 3.5, calculated energy thresholds are in good agreement with the experimental results.

Next, energy diagrams for targeted ions were computationally prepared. Figure 3.15 shows the calculated potential curves for these reactions. The dotted line represents the adiabatic potential curve calculated by assuming a rigid structure identical to the ground state structure. Electron impact instantaneously excites PPVE, vertically transitioning it from the ground state to the positive ion state, followed by a brief relaxation of the molecular structure. Another solid line shows non-adiabatic potential curves calculated for the relaxed structure following the transition initiated by electron impact. The total energy difference between the ground and positive ion states of PPVE is estimated to be

9.9 eV, determined from the energy minima of the adiabatic positive ion state and the ground state on the potential curves.

Figure 3.15(a-c) shows the calculated potential curves along the reaction coordinates for the C–C bonds of the fluoroalkyl chain bound to the vinyl ether group: (a) $\text{F}_3\text{C} + \text{CF}_2\text{CF}_2\text{OC}_2\text{F}_3$, (b) $\text{F}_3\text{CF}_2\text{C} + \text{CF}_2\text{OC}_2\text{F}_3$, and (c) $\text{F}_3\text{CF}_2\text{CF}_2\text{C} + \text{OC}_2\text{F}_3$. Those of the $\text{CF}_3^+ + \text{C}_2\text{F}_4\text{OC}_2\text{F}_3$, $\text{C}_2\text{F}_5^+ + \text{CF}_2\text{OC}_2\text{F}_3$ and $\text{C}_3\text{F}_7\text{O} + \text{C}_2\text{F}_3^+$ reactions have no minimum, e.g., no dissociative ionization occurs. The nonadiabatic potential curve for the $\text{C}_3\text{F}_7^+ + \text{OC}_2\text{F}_3$ reaction always exhibits lower energies. This calculated result therefore supports the dissociative ionization of PMVE into $\text{C}_3\text{F}_7^+ + \text{C}_2\text{F}_3\text{O}$. The appearance energy for C_3F_7^+ at an ionization threshold energy of 10.9 eV agreed well with the experimental value of 11.8 eV obtained from Figure 3.11.

In the experimental results of $\text{C}_2\text{F}_2\text{O}^+$, Figure 3.15(c) also shows the potential curves for a case of rearrangement fragmentation. In this process, once the CO bond is stretched, the F atom will favorably rearrange to form the more stable product of C_3F_8 . Similar rearrangement fragmentation has been proposed in the case of PMVE, as an isomer of $\text{C}_3\text{F}_7\text{O}$. Therefore, the $\text{C}_2\text{F}_2\text{O}^+$ rather than the C_3F_7^+ fragmentation occurs favorably.

Figure 3.16 shows the calculated potential curves for negative ion formation. The calculated potentials for the $\text{C}_2\text{F}_3\text{O}^- + \text{C}_3\text{F}_7$ and $\text{C}_3\text{F}_7\text{O}^- + \text{C}_2\text{F}_3$ reactions show dissociative curves. The formation of $\text{C}_3\text{F}_7\text{O}^-$ was measured at low energies compared with that of $\text{C}_2\text{F}_3\text{O}^-$. The total energy difference between the ground and negative ion states of PPVE was estimated to be 2.6 eV. This energy difference was in good agreement with the experimental appearance energy of 2.0 eV for $\text{C}_3\text{F}_7\text{O}^-$ and 2.1 eV for $\text{C}_2\text{F}_3\text{O}^-$. The negative ions of $\text{C}_3\text{F}_7\text{O}^-$ were favorably formed via electron attachment.

Abundant positive and negative ions were generated via the three pathways shown in Figure 3.16 at the thresholds listed in Table 3.5.

The significantly large ionization efficiency of CF_3^+ was experimentally observed as the leading cause of large cross-sections for dissociative ionization of CF_3^+ ions. As shown in Figure 3.11, the ionization efficiency curves for CF_3^+ from PPVE was large, on the order of 10^{-20} cm^{-2} . Figure 3. 17 shows comparison of the ionization efficiency for CF_3^+ between (a) PPVE and Figure 3.3 (a) shows an isomer of $\text{C}_3\text{F}_6\text{O}$ (PMVE), over a larger electron energy range of 80 eV. For the perfluorovinyl ethers, such as PPVE and PMVE, the cross-sections of the other ions were only on the order of 10^{-21} cm^{-2} . Thus, the process for CF_3^+ is more than an order of magnitude higher than other ionization fragmentations. Regardless of the appearance energy, CF_3^+ ion dominated with only 20% of the other ions formed.

For other perfluoroalkanes such as $\text{C}_x\text{F}_{2x+2}$ ($x = 2-8$), the largest abundant ion is CF_3^+ . At an electron energy of 70 eV, almost 30 to 40% of C_2F_5^+ ion is fragmented. During the electron impact processes, the time for ion fragmentation is long compared with the time for ionization or excitation. Thus, the energy distribution of the ions was partitioned broadly into internal energies. By the energetic electron impact on the perfluorovinyl ethers, excess energy is distributed among internal energies and survives for the time required for relaxation from vibrational excited states to the ground state. Therefore, rates for this process depend on the reaction degeneracy and the number of internal energy states in the transition state. Fragmentation via direct bond rupture into smaller product ions occurs more favorably than the rearrangement or cleavage into molecules with large mass. Estimation of the density of states in the quantum chemical calculations is a further area of research. As a consequence, we must emphasize that the characteristic CF_3^+ formation of the perfluorovinyl ethers is characteristic of ether and vinyl bonds in these molecules.

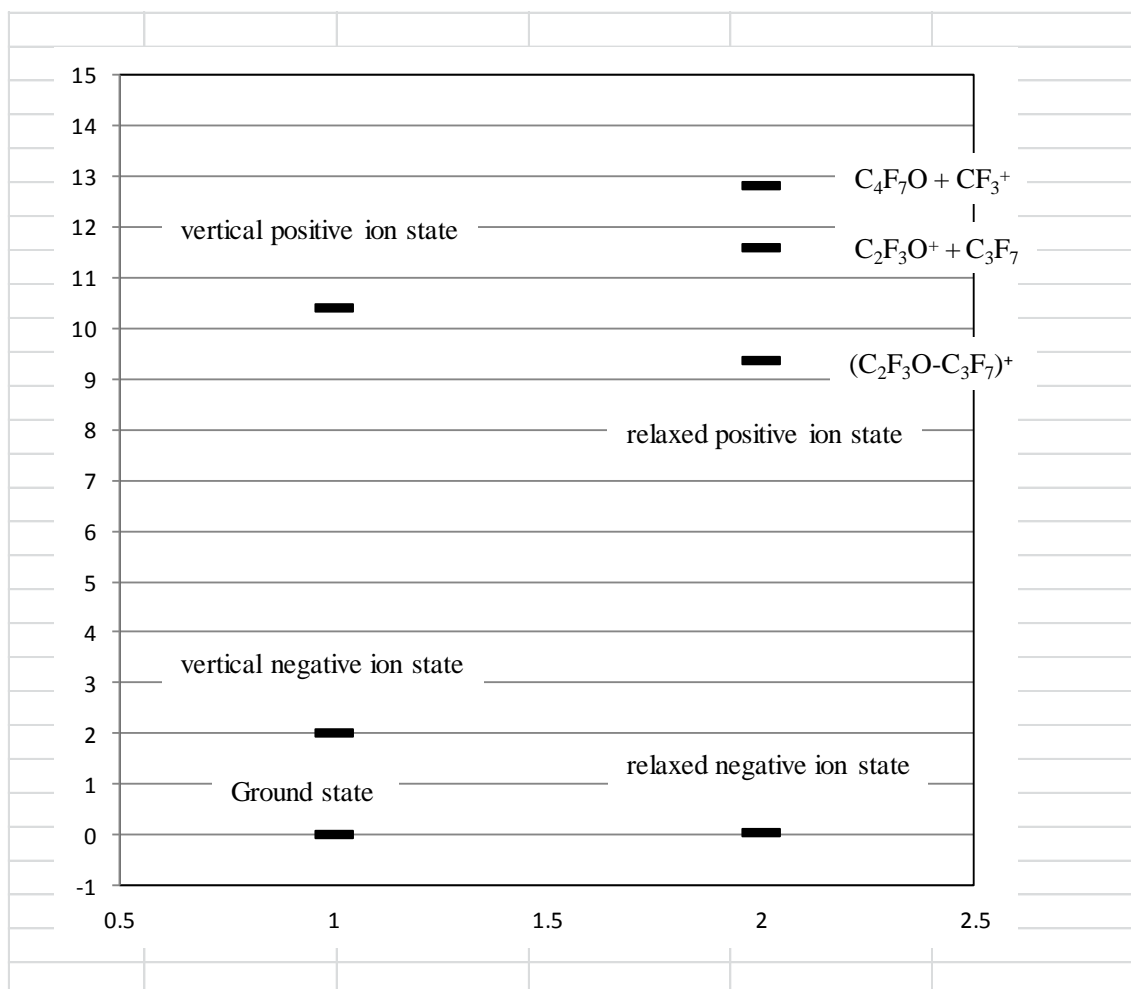
Fig. 3.14 energy diagram for $C_5F_{10}O$

Table 3.5 Threshold for dissociative ionization reactions

Reaction	Energy threshold (eV)	
	Experiments	Calculation
$\text{CF}_3^+ + \text{C}_4\text{F}_7\text{O}$	14.5	12.8
$\text{C}_2\text{F}_2\text{O}^+ + \text{C}_3\text{F}_8$	11.4	12.3
$\text{C}_2\text{F}_2\text{O}\cdot + \text{e}^- \rightarrow \text{C}_2\text{F}_2\text{O}^+$		9.9
$\text{C}_2\text{F}_5^+ + \text{C}_3\text{F}_5\text{O}$	16.5	12.8
$\text{C}_3\text{F}_7^+ + \text{C}_2\text{F}_3\text{O}$	11.8	10.9
$\text{C}_5\text{F}_{10}\text{O}^+$	10.3	9.9
$\text{C}_3\text{F}_7\text{O}^- + \text{C}_2\text{F}_3$	2.0	2.7
$\text{C}_3\text{F}_7 + \text{C}_2\text{F}_3\text{O}^-$	2.1	2.6

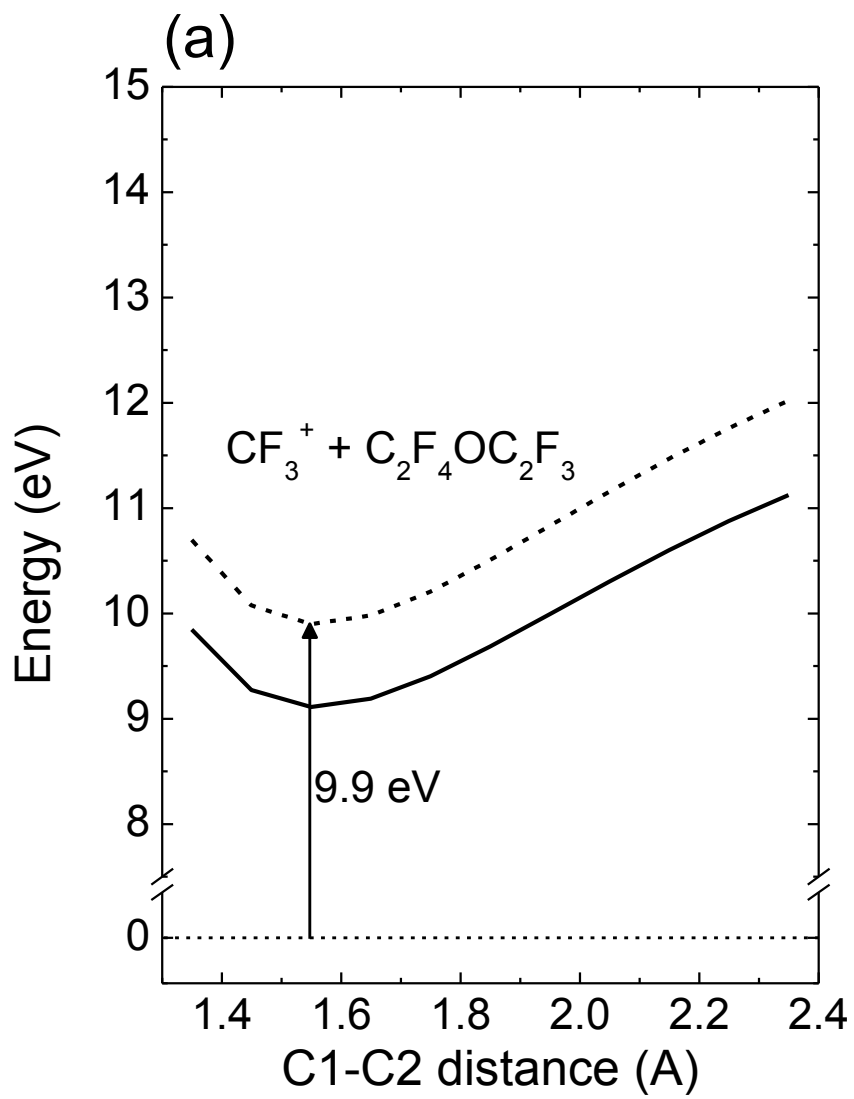


Fig. 3.15 (a) Potential curves for the $\text{CF}_3\text{-C}_2\text{F}_4\text{OC}_2\text{F}_3$

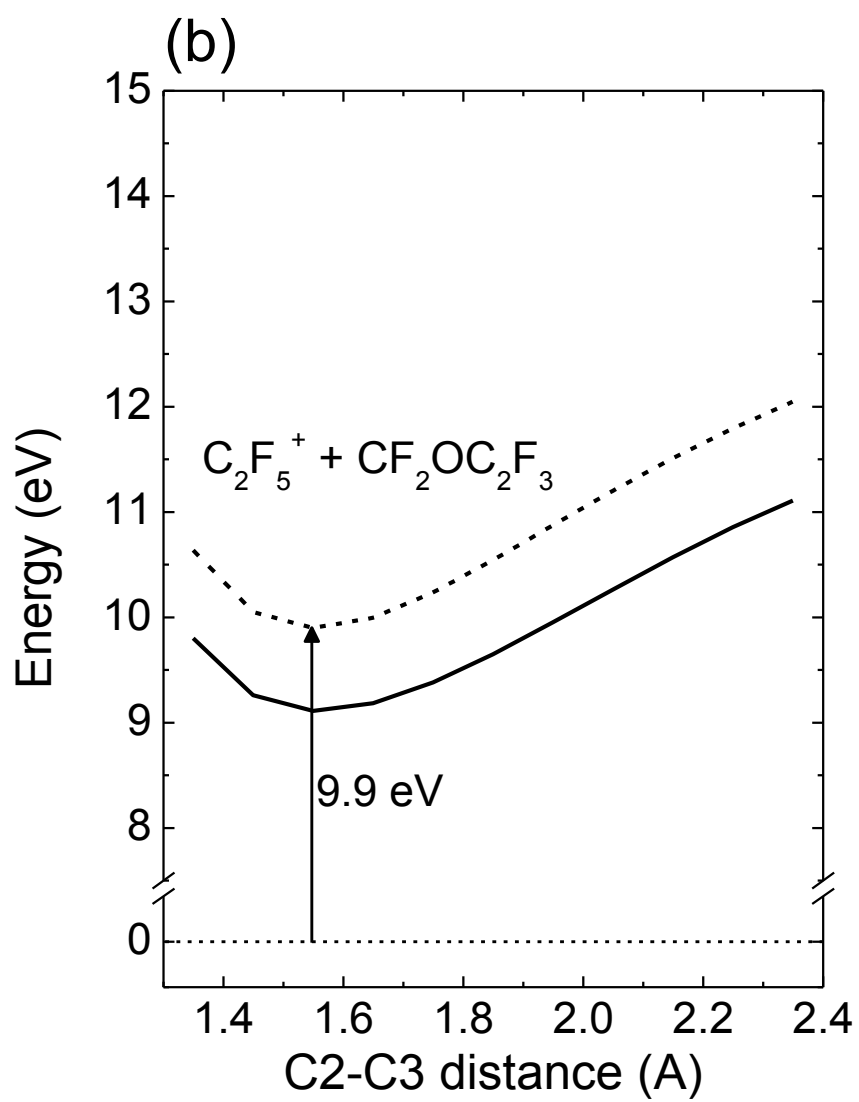


Fig. 3.15 (b) Potential curves for the C_2F_5 - $CF_2OC_2F_3$

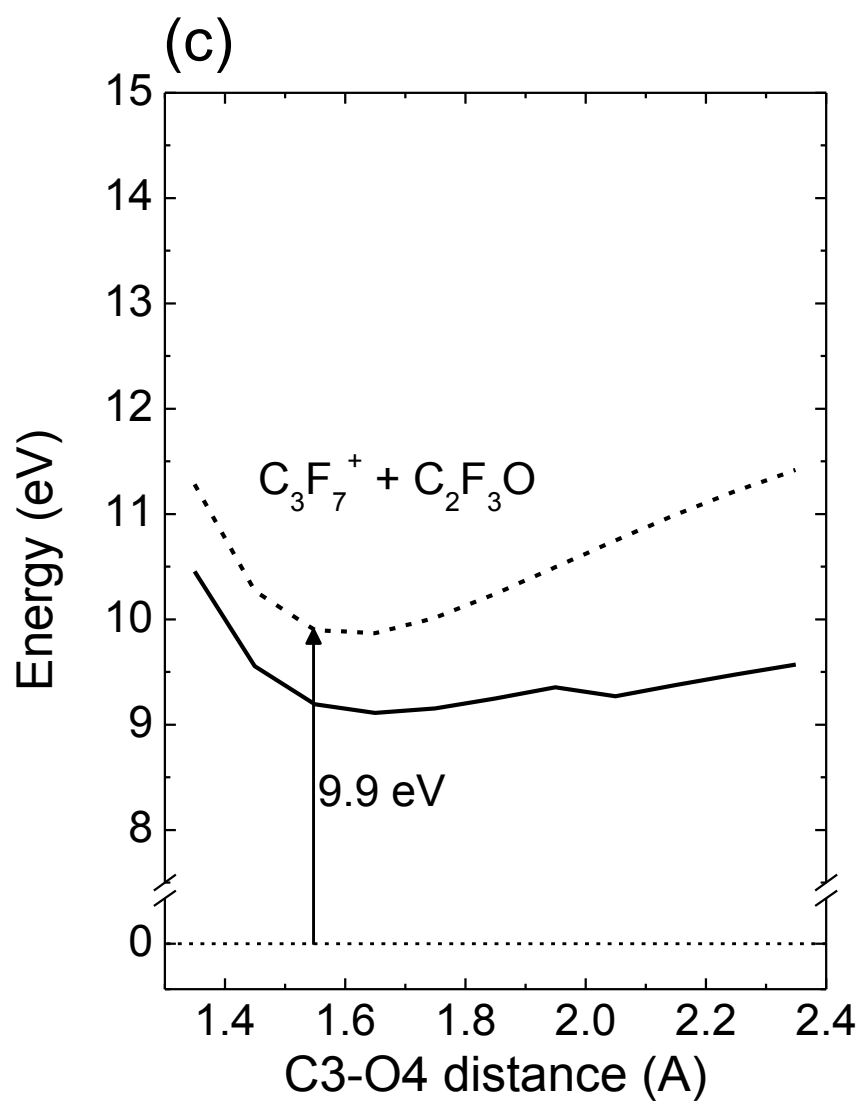


Fig. 3.15 (c) Potential curves for the $C_3F_7-OC_2F_3$

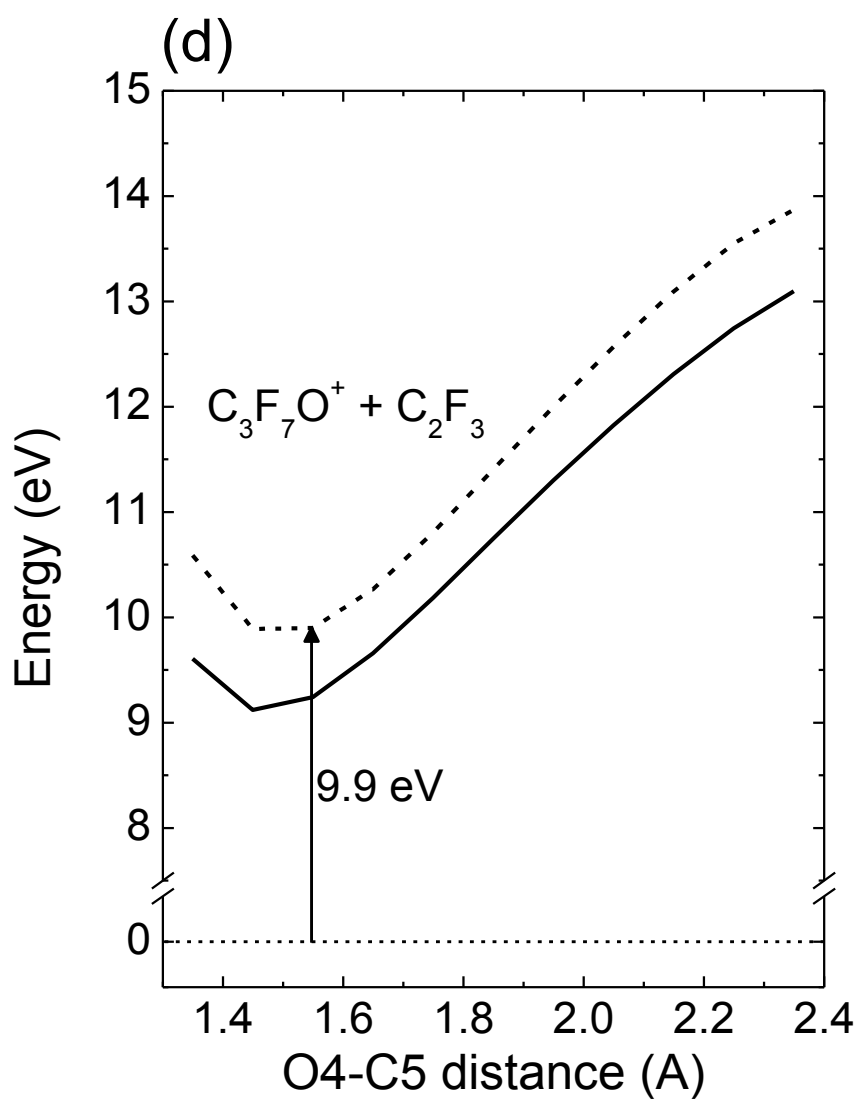


Fig. 3.15 (d) Potential curves for the $\text{C}_3\text{F}_7\text{O}-\text{C}_2\text{F}_3$

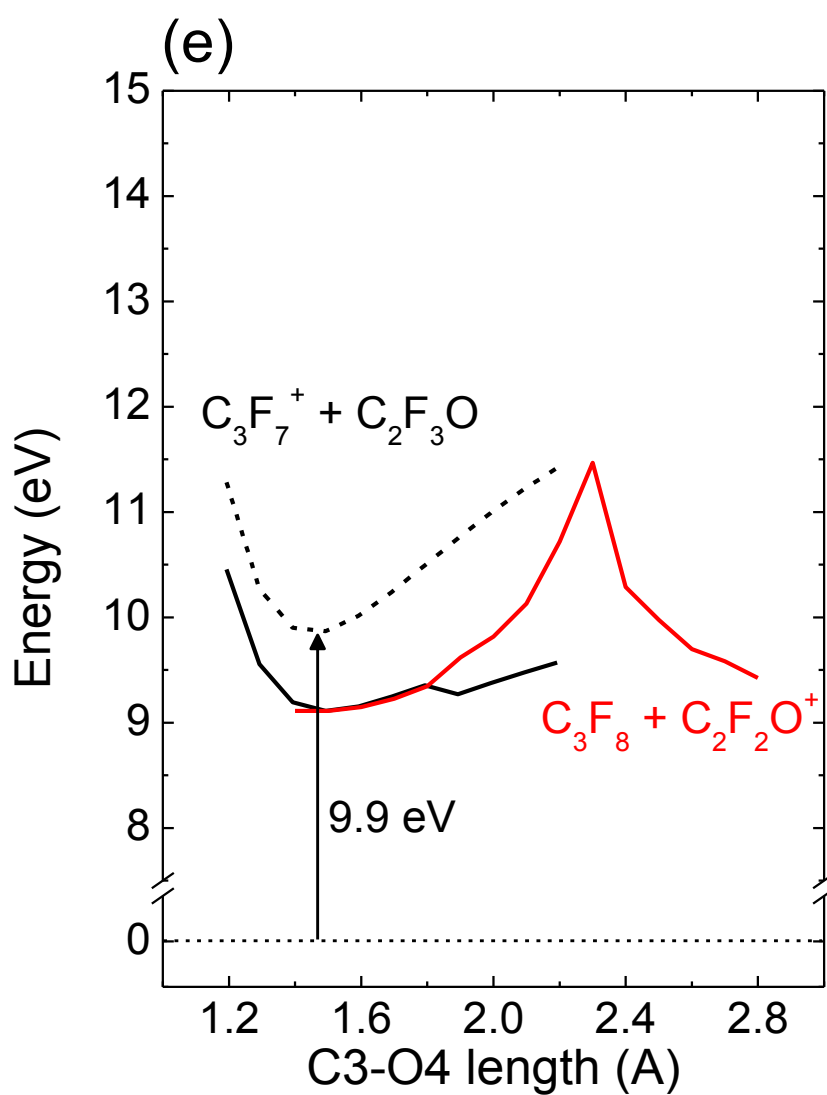


Fig. 3.15 (e) Potential curves for the $C_3F_8 + C_2F_2O^+$

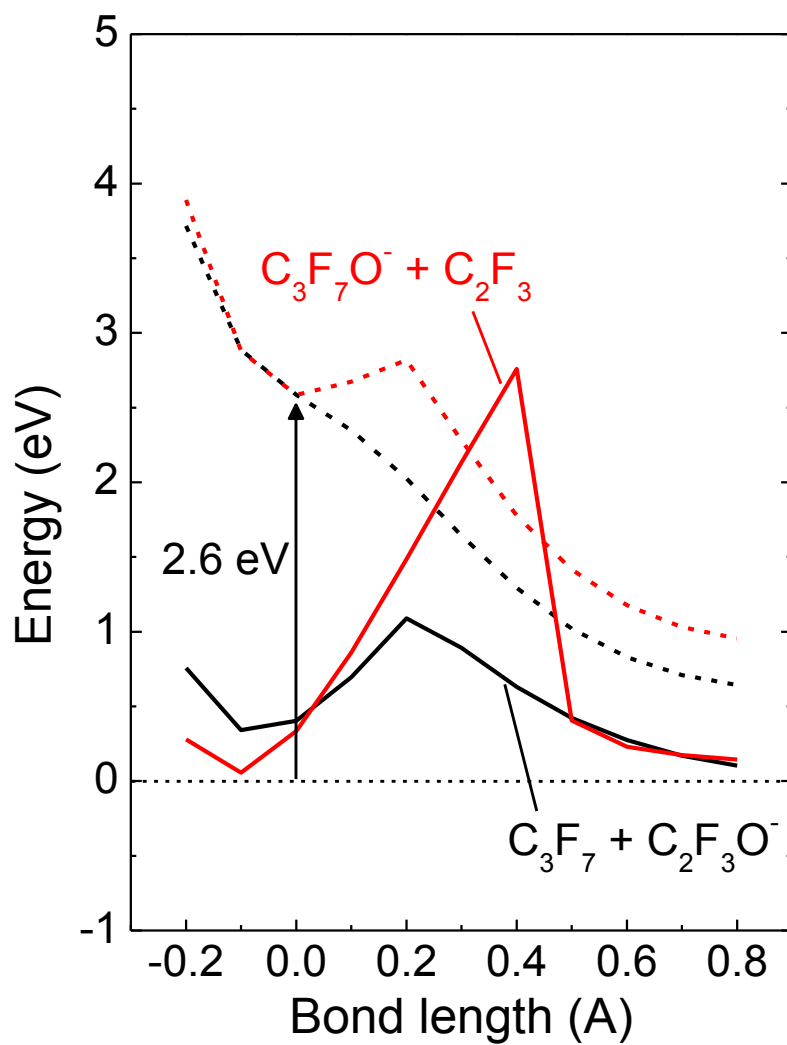


Fig 3.16 Potential curves for negative ion states

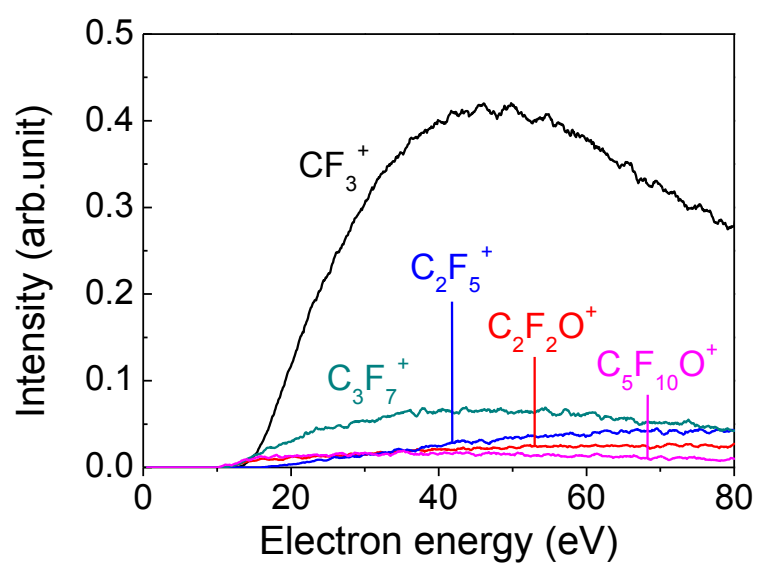


Fig 3.17 Ionization efficiency curves for the PPVE dissociative ionization

3.4 Conclusion

In this chapter, two perfluoro-vinyl-ether molecule (PMVE and PPVE) were measured and calculated to clarify dissociation reaction of ether structure.

The dissociative ionization and electron attachment reactions of a C_3F_6O isomer, perfluoro-methyl-vinyl-ether, were examined using quadrupole mass spectrometry. The most abundant CF_3^+ ions were generated by dissociative ionization at a threshold energy of around 10.2 eV, and the second most abundant positive ions were $C_2F_2O^+$. These data suggest rearrangement of the F atom to form CF_4 . Generation of the abundant negative ions, $C_2F_3O^-$, was confirmed by calculation of the potential energy curves for electron attachment along the reaction coordinate on both sides of the ether C–O bond. Only dissociative electron attachment was involved in $C_2F_3O^-$ ion generation.

The dissociative ionization and electron attachment reactions of a $C_5F_{10}O$ isomer, perfluoropropylvinyl ether (PPVE), were examined using quadrupole mass spectrometry. The major positive ion was CF_3^+ . A minority of positive and negative ions, involving $C_2F_2O^+$, $C_2F_3O^-$ and $C_3F_7O^-$, were observed. The appearance energies causing the dissociative ionization were around 14.5 for CF_3^+ and 11.8 eV for $C_3F_7^+$ ions. Each reaction channel was confirmed by the potential energy curves provided in the quantum chemical calculations. Combined with the previous research on the C_3F_6O isomer, perfluoromethylvinyl ether (PMVE), the observed ion efficiencies for the CF_3^+ ion were larger, on the order of 10^{-20} cm^{-2} , compared with the order of only 10^{-21} cm^{-2} for the other channels. This is attributed to the excess energy of energetic electron impacts being distributed among internal energies of CF_3^+ with stabilization of the ionizing charge by delocalization onto the vinyl ether bond. Overall, perfluorovinyl ethers characteristically generated CF_3^+ as the largest abundant ion.

This information may be useful for controlling the generation of fluorocarbon ions and in the design of molecules containing a vinyl-ether.

3.5 Reference

- [1] Y. Morikawa, W. Chen, T. Hayashi, and T. Uchida: Jpn. J. Appl. Phys. **42** (2003) 1429.
- [2] T. Uchida, and S. Hamaguchi: J. Phys. D: Appl. Phys. **41** (2008) 083001.
- [3] K. Karahashi, K. Yanai, K. Ishikawa, H. Tsuboi, K. Kurihara, and M. Nakamura: J. Vac. Sci. & Tec. A, **22** (2004) 1166.
- [4] K. Karahashi, and S. Hamaguchi: J. Phys. D: Appl. Phys. **47** (2014) 224008.
- [5] M. A. Lieberman, and A. J. Lichtenberg: Principles of Plasma Discharges and Materials Processing, 2nd ed. Wiley (2005).
- [6] Y. Feurprier, Y. Chinzei, M. Ogata, T. Kikuchi, M. Ozawa, T. Ichiki, and Y. Horiike: J. Vac. Sci. & Tec. A, **17** (1999) 1556.
- [7] R. Chatterjee, S. Karecki, R. Reif, V. Vertanian, and T. Sparks: J. Electrochem. Soc. **149** (2002) G276.
- [8] R. Chatterjee, S. Karecki, R. Reif, T. Sparks, V. Vartanian, and B. Goolsby: J. Electrochem. Soc. **148** (2001) G721.
- [9] H. Hayashi, S. Morishita, T. Tatsumi, Y. Hikosaka, S. Noda, H. Nakagawa, S. Kobayashi, and M. Inoue: 1999, J. Vac. Sci. & Tec. A, **17** (1999) 2557.
- [10] T. Yamaguchi, T. Komuro, C. Koshimizu, S. Takashima, K. Takeda, H. Kondo, K. Ishikawa, M. Sekine, and M. Hori: J. Phys. D: Appl. Phys. **45**, (2012) 025203.
- [11] Y. Miyawaki, Y. Kondo, M. Sekine, K. Ishikawa, T. Hayashi, K. Takeda, H. Kondo, A. Yamazaki, A. Ito, H. Matsumoto, and M. Hori: Jpn. J. Appl. Phys. **52** (2103) 016201.
- [12] L. Pruette, S. Karecki, R. Reif, L. Tousignant, W. Reagan, S. Kesari, and L. Zazzera: J. Electrochem. Soc. **147** (2000) 1149.
- [13] M. Nagai, T. Hayashi, and M. Hori: Jpn. J. Appl. Phys. **45** (2006) 7100.
- [14] Y. Miyawaki, E. Shibata, Y. Kondo, K. Takeda, H. Kondo, K. Ishikawa, H. Okamoto, M. Sekine, and M. Hori: Jpn. J. Appl. Phys. **52** (2013) 020204.

- [15] Y. Chinzei, Y. Feurprier, M. Ozawa, T. Kikuchi, K. Horioka, T. Ichiki, and Y. Horiike: J. Vac. Sci. & Tec. A, **18** (2000) 158.
- [16] M. Elango, G. S. Maciel, F. Palazzetti, A. Lombardi, and V. Aquilanti: J. Phys. Chem. A, **114** (2010) 9864.
- [17] D. P. Chong, and C. H. Hu: J. Chem. Phys. **108** (1998) 8950.
- [18] J. H. Beynon, R. M. Capriolain, and R. G. Cooks: Org. Mass Spectrometry, **1** (1974) 1.
- [19] C. C. Van de Sande, and F. W. McLafferty: J. Am. Chem. Soc. **97** (1975) 4617.
- [20] W. J. Bouma, J. K. MacLeod, and L. Radom: J. Am. Chem. Soc. **102** (1980) 2246.
- [21] R. D. Bowen, and A. G. Harrison: Org. Mass Spectrometry, **16** (1981) 159.
- [22] C. E. Hudson, and D. J. McAdoo: Org. Mass Spectrometry, **17** (1982) 366.
- [23] F. Turecek, and F. W. McLafferty: J. Am. Chem. Soc. **106** (1984) 2525.
- [24] C. Lifshitz: Org. Mass Spectrometry, **23** (1988) 303.
- [25] I. J. Kim, H. K. Moon, J. H. Lee, N. E. Lee, J. W. Jung, and S. H. Cho: Microele. Reliab. **52**, (2012) 2970.
- [26] F. Fracassi, R. d'Agostino, E. Fornelli, and T. Shirafuji: Jpn. J. Appl. Phys. **41** (2002) 6287.
- [27] F. Fracassi, R. d'Agostino, E. Fornelli, F. Illuzzi, and T. Shirafuji: J. Vac. Sci. & Techn. A, **21** (2003) 638.
- [28] <http://webbook.nist.gov/chemistry>.
- [29] C. Leibold, S. Reinemann, R. Minkwitz, P. R. Resnik, and H. Oberhammer: J. Org. Chem. **62** (1997) 6160.
- [30] J. S. Forsythe, and D. J. T. Hill: Prog. Polym. Sci. **25** (2000) 101.
- [31] E. Krishnakumar, and S. K. Srivastava: J. Phys. B: At. Mol. Opt. Phys. **21** (1988) 1055.

Chapter 4 Mechanism of Dissociation and Etching Process of Hydro-fluorocarbon in Rare Gas diluted Plasma

4.1 Introduction

In ultra-large-scale integrated circuit (ULSI) fabrication, hydrofluorocarbon molecules, $\text{CH}_x\text{F}_{4-x}$ ($x=1,2,3$), are frequently used for etching of dielectric SiO_2 and Si_3N_4 .^[1-4] The ability to control the dimensions of the etched features is necessary for SiO_2 etching for contact holes and for Si_3N_4 etching for gate spacers.^[5-13] To achieve this, a high selectivity to protect the underlying film is a key performance feature during etching. In general, reducing spontaneous etching of the Si is accomplished by reducing the quantity of F atoms in the gas phase, because F atoms react with Si to form SiF_x . To reduce the F density, a fluorocarbon gas containing hydrogen can be used. A previous report indicated that highly selective etching of SiO_2 and Si_3N_4 films while protecting the underlying Si layer was accomplished using the novel hydrofluorocarbon gas, C_5HF_7 .^[14,15]

For Si_3N_4 etching, H atoms enhance the removal of N atoms via formation of volatiles such as NH_x and HCN ; therefore, the H atom acts as an etchant. For this purpose, CH_2F_2 gas has been used to achieve highly selective etching of Si_3N_4 without affecting the underlying material.^[16-22]

Hydrofluorocarbons have H atoms in place of F atoms in fluorocarbon gases. Dissociation reactions involving C–H and C–F bonds are of interest for controlling the density of reactive species: F atoms, produced by dissociation of the C–F bond, are a main etchant for Si, while H atoms, produced by dissociation of the C–H bond, promote the deposition of polymers on a substrate surface and increase the selectivity and processing accuracy. Furthermore the dissociation of C–F and C–H bonds also

produces CH_xF_y radicals that will contribute to deposition. One could even emphasize that the CH_xF_y radical produced via F abstraction will contribute more to deposition than the CH_xF_y radicals produced by H abstraction, since their net F/C ratio is smaller. Therefore a balance of species for etching and deposition is believed to be important and to be closely related to the dissociation processes in gas-phase. However, the mechanism involved in highly selective etching has not yet been fully elucidated, and the variety and densities of the ions and radicals generated in hydrofluorocarbon plasmas have not been determined. Therefore, the present study focused on dissociative reactions in plasma with the goal of controlling ion and radical densities by investigating the dissociation channels of the parent molecules.

Several research groups have reported vacuum ultraviolet (VUV) absorption data for CH_2F_2 molecules.^[23-25] Electron collision-induced reactions of CH_2F_2 molecules have also been reported.^[26-31] However, the mechanism underlying the generation of the chemical species is complicated because the etching plasmas have relatively low electron temperatures of less than 5 eV.^[32] Therefore, detailed investigations of electron impact dissociative ionization at a threshold energy of approximately 10 eV for dissociative ionization are needed.

The present study examined the ions and radicals produced in CH_2F_2 plasmas diluted with Ar or Kr gas. For these plasmas, the dominant pathways for dissociative ionization of CH_2F_2 in plasma are determined by the charge exchange collision reactions due to resonantly occurring dissociation at energies similar to the ionization of rare gases. Furthermore, selective dissociation of C-F or C-H bonds and the density of CH_2F^+ and CHF_2^+ ions obtained by adding Ar or Kr gas to the plasma was shown to control the dissociation process.

4.2 Comparison of dissociation reaction and ion density in CH_xF_y plasma

A quadrupole mass spectrometer (QMS; Hiden Analytical, EQP) was installed in the chamber wall of the commercial plasma etching reactor, as schematically shown in Figure 4.1. The reactor can process 200 mm diameter wafers. In the conventional CCP setup for dielectric material etching processes, VHF (60 MHz) power is applied to the upper electrode made of silicon and sustained the plasma discharge. The temperature of the upper electrode and side wall were maintained at 60°C by circulating a temperature control coolant. RF (2 MHz) power was applied to the lower electrode to control the energies for ion-bombardment onto the samples. A 200 mm wafer was electrostatically chucked on the lower electrode which was cooled to a temperature of 20°C. Highly purified CHF_3 , CH_2F_2 and CH_3F at a flow rate of 100 sccm was introduced into the chamber through the shower head of upper electrode and maintained at a pressure of 1.0 Pa. The aperture to the QMS had a diameter of 100 μm . The pressure in the QMS was 5.2×10^{-5} Pa during measurements and 9.1×10^{-6} Pa for fully pumping-down background; under these conditions, residual gas did not affect signal measurements.

To investigate dissociation reaction at C-H and C-F bonds in CH_xF_y , The dissociative ionization cross sections of CH_xF_y and ions density in CH_xF_y plasma were measured by QMS and compared each other. Figure 4.1 shows measured cross sections of C-H dissociation product ion and C-F dissociation product ion produced by electron collision with CH_xF_y . In measurement of dissociative ionization cross sections, VHF power and RF power were not applied. For all CH_xF_y , C-H bond was dissociated easier than C-F, because energy threshold of C-H dissociation was lower. For only CHF_3 , C-F dissociative ionization cross section was rapidly increased with electron energy and became higher than C-H dissociative ionization cross section around 22 eV. Figure 4.2

shows the relative CH_xF_y ion densities in CH_xF_y plasma diluted with pure Ar, under discharge conditions of 1800 W VHF power to the upper electrode, at a total flow rate of 330 sccm, including 30 sccm CH_xF_y gas, at 2 Pa.. In the case of CHF_3 , CF_3^+ ion and CHF_2^+ ion density were similar reflecting the results of cross section. In the case of CH_3F , CH_2F^+ ion density was much higher than CH_3^+ ion density. This result reflects the results of cross section similarly to CHF_3 plasma. On the other hand, in CH_2F_2 plasma, a CHF_2^+ ion was major ion. However, this result did not correspond with the result of cross section. Figure 4.3 shows the relative CH_xF_y ion densities in $\text{CH}_2\text{F}_2/\text{Kr}$ plasma to change the plasma parameter much. In only CH_2F_2 plasma, the major ion was changed by changing Ar dilution to Kr dilution.

From these results, it is assumed the selective dissociation processes were occurred in $\text{CH}_2\text{F}_2/\text{Ar}$ and $\text{CH}_2\text{F}_2/\text{Kr}$ plasma. To clarify the mechanism of C-H and C-F dissociation and control dissociation bond, CH_2F_2 dissociation processes were investigated in detail from next section.

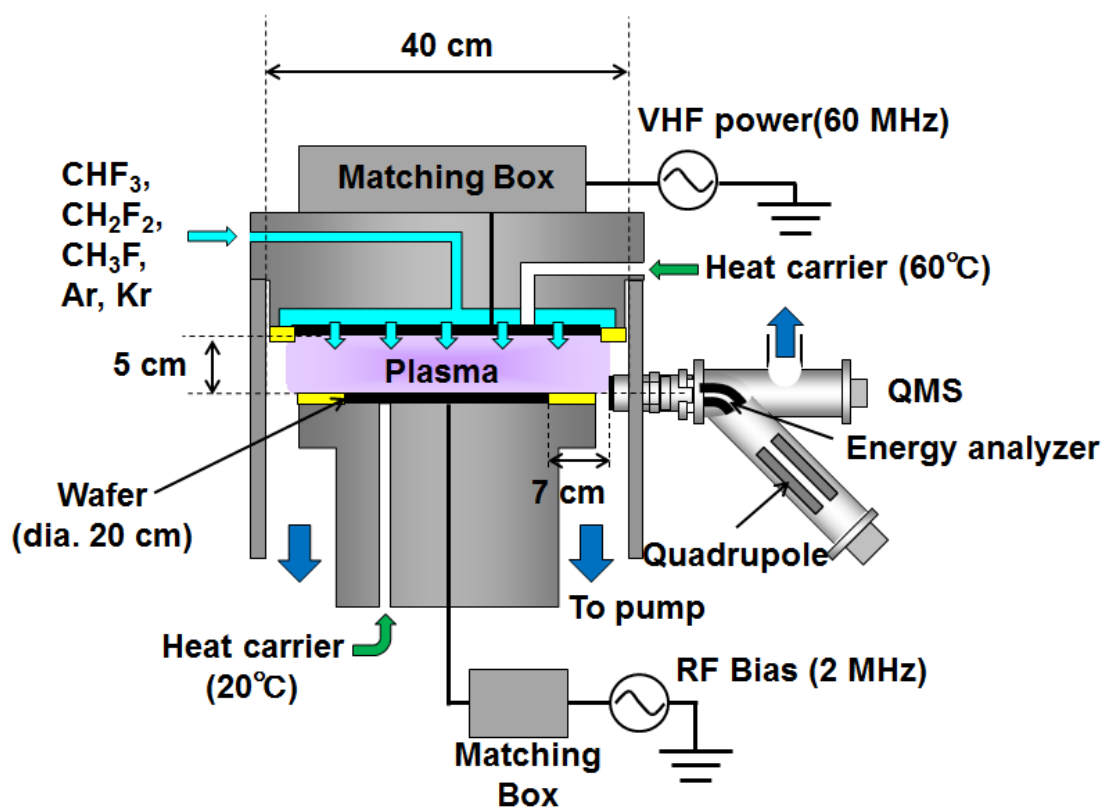
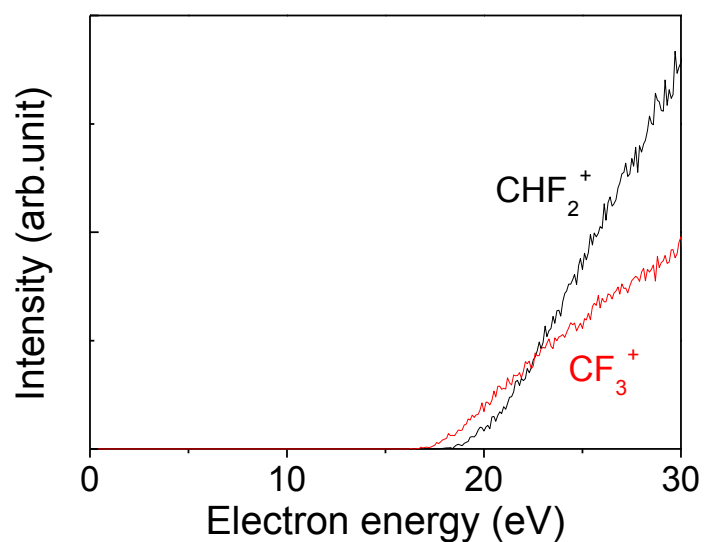


Fig. 4.1 Schematic of dual-frequency CCP reactor.

Fig 4.1 (a) Cross sections of C-H dissociation product ion and C-F dissociation product of CHF₃

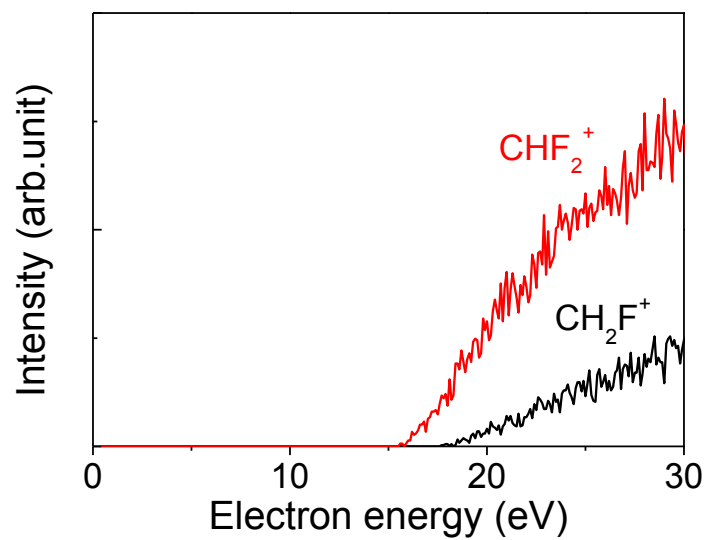


Fig 4.1 (b) Cross sections of C-H dissociation product ion and C-F dissociation product of CH_2F_2

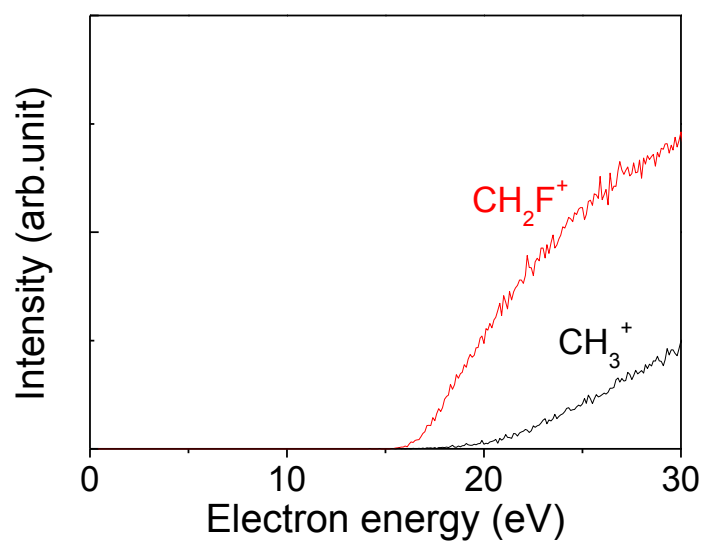
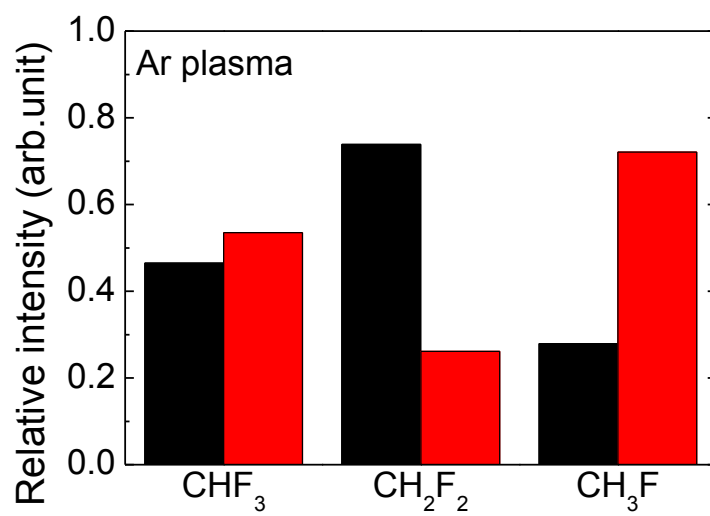
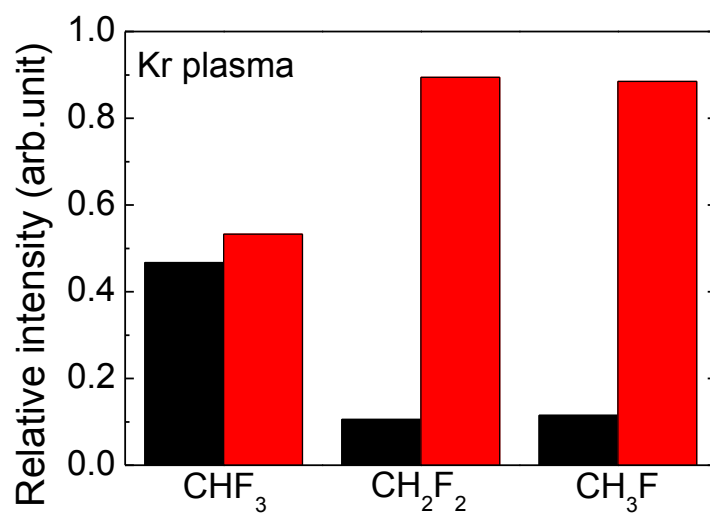


Fig 4.1 (c) Cross sections of C-H dissociation product ion and C-F dissociation product of CH_3F

Fig 4.2 Relative CH_xF_y ion densities in $\text{CH}_2\text{F}_2/\text{Ar}$ plasmaFig 4.3 Relative CH_xF_y ion densities in $\text{CH}_2\text{F}_2/\text{Kr}$ plasma

4.3 Dissociation reaction of C-H and C-F bonds in CH₂F₂

4.3.1 Experimental detail

A mixture of Ar or Kr gas (flow rate of 300 sccm) with CH₂F₂ gas (flow rate of 30 sccm) was introduced into a chamber through the upper electrode. In the trace rare gases optical emission spectroscopy,^[36-39] a small amount (less than 4%) of five rare gases (He, Ne, Ar, Kr, and Xe) was added with a flow rate of 10 sccm (2 sccm in each) in portion of the feed gas, e.g. the Ar or Kr gas with a flow rate of 290 sccm. The pressure was maintained at 2 Pa. High-frequency (60 MHz, VHF) power of 1800 W was applied to the upper electrode. In the experiments, medium frequency (2 MHz, MF) power was not applied to the lower electrode as a substrate bias.

A quadrupole mass spectrometer (QMS; Hiden Analytical, EQP) was installed in the reactor at the chamber wall. A 100- μ m diameter aperture was installed in the QMS entrance; the positive ion collection mode was used for sampling. The QMS head was electrically grounded, and collected ions from the bulk plasma through the ion sheath. Before taking mass spectra, detected ion energy was optimized for maximizing the signal intensities, since the maximum intensities depended on the plasma potential in front of the aperture. For measurements for radicals, we took mass spectra with electron energy of 12 eV, that is lower than appearance energy of ionization. The mass-dependent transmission efficiency was experimentally determined for our spectrometer. The calibrations were equated with $(m/z)^{-0.84}$. Ion densities were determined in either Ar- or Kr-diluted CH₂F₂ plasmas by integrating measured ion densities with ion energies ranged between 0 and 50 eV over the whole ion energy.

Dissociative ionization of the CH₂F₂ gas was measured using pure CH₂F₂ at a flow rate of 100 sccm introduced into the chamber at a pressure maintained at 1 Pa. Under this condition, we confirmed the QMS chamber pressure being enough low of 7×10^{-5} Pa. Cross sections of the electron impact dissociations of the two channels, with

respect to CH_2F^+ ion for C-F bond dissociation and CHF_2^+ ion for C-H bond dissociation, were estimated as a function of electron energy by reference to the Ar cross section.^[33] Threshold energies were determined by linear extrapolation of the slope to the intercept of the axis.

The absolute plasma density was measured using a plasma absorption probe (PAP).^[34,35] The probe was constructed from an antenna (length of 5 mm) using coaxial cable and a glass tube (inner diameter of 4 mm). During plasma discharge, resonant absorption spectra with frequencies on the order of GHz were recorded by a network analyzer (Agilent E5071C). The plasma density was estimated from the square of the resonance frequency.^[35]

The trace rare gases optical emission spectroscopy (OES) was performed^[36-39]; optical emission was observed through a window on the chamber wall, collected by optical fibers and a lens directed toward the center of the chamber, and measured using a spectrometer (OptoSirius Corporation, HR4000). Emissions of 750.4 nm [Ar $3p5(2P^{\circ}1/2)4s \rightarrow 3p5(2P^{\circ}1/2)4p$], 768.5 nm [Kr $4p5(2P^{\circ}1/2)5s \rightarrow 4p5(2P^{\circ}1/2)5p$], and 881.9 nm [Xe $5p5(2P^{\circ}3/2)6s \rightarrow 5p5(2P^{\circ}3/2)6p$] were observed.^[36-38] Comparing the observed atomic line intensities estimated to change the electron temperature of plasma. Small amount of the added inert gas mixture did not significantly perturb the plasma as no change in the ionic mass spectra is observed.

4.3.2 Mechanism of selective dissociation of C-H and C-F in CH₂F₂

Figure 4.3 shows positive-ion mass spectra for the CH₂F₂ plasma diluted with pure Ar or pure Kr, under discharge conditions of 1800 W VHF power to the upper electrode, at a total flow rate of 330 sccm, including 30 sccm CH₂F₂ gas, at 2 Pa. Results indicate that the main peaks observed were those for the dilution gas ions, and CH₂F⁺ and CHF₂⁺ ions in the CH₂F₂ plasma. The peaks were observed at 20 m/z for Ar²⁺, 33 m/z for CH₂F⁺, 36 m/z for ³⁶Ar⁺, and 40 m/z for Ar⁺, 52 m/z for CHF₂⁺, and 84 m/z for Kr⁺. The relative intensities are listed in Table 4.1. The intensities were normalized to 100% by the total ion intensities of each rare gas. A higher intensity was found for CH₂F⁺ than for CHF₂⁺ for the case of Kr, while the opposite relation was found for Ar. Figure 4.4 shows typical ion energy distribution of CH₂F⁺ ion in the CH₂F₂ plasma diluted with pure Ar or pure Kr, with identical condition for Figure 4.3. Ion intensities were obtained by integration over energies ranged between 0 to 50 eV. Moreover the ion energy for measurements of mass spectra was optimizes at the maximum in intensity, e. g. approximately 38 eV for the Ar dilution and 30 eV for the Kr dilution.

The measurements revealed that the dominant positive ions were CH₂F⁺ and CHF₂⁺. The ionization energy of CH₂F₂⁺ was 13.8 eV.^[29] However, as reported by Torres *et al.*, the ionization cross section for CH₂F₂⁺ is approximately 5% compared with those for CH₂F⁺ and CHF₂⁺.^[29] In quantum chemistry calculations, channels of the dissociative ionization corresponded with similar behavior in the lowest triplet and singlet excited energies assuming that the fundamental vibrations of CH₂F₂ include asymmetric (C_s) and symmetric (C_{2v}) modes. The symmetric vibrations cause the dissociation of two atoms bound to a central C atom. Thus, the other channels, such as CH₂F₂ + e⁻ → CH₂⁺ + 2F· + 2e⁻ and CH₂F₂ + e⁻ → CF₂⁺ + 2H· + 2e⁻, contributed to the generation of ions for higher-energy electron collisions, however these channels were determined to be

negligibly small compared with the two major channels.^[40]

Torres *et al.* reported cross sections and appearance potentials for electron impact dissociative ionization of CH₂F₂ molecules.^[29] In the ionization pathway generated for CH₂F⁺ and CHF₂⁺ ions, two channels are involved: CH₂F⁺ through C-F bond dissociation or through C-H bond dissociation. The reaction schemes for the dissociative reactions in electron collisions are given by:



The counter fragments of charge-neutral H and F atoms were generated simultaneously through these dissociation mechanisms.

Figure 4.5 shows measured cross sections of CHF₂⁺ and CH₂F⁺ produced by electron collision with CH₂F₂. They were constructed by referencing the QMS intensities and known cross section for Ar gas.^[33] Cross sections were estimated for the fragmented ions from parent CH₂F₂ gas as a function of electron impact energies between 10 and 20 eV. Ionization thresholds were observed at 13.8±0.5 eV for CHF₂⁺ and at 15.8 ±0.5 eV for CH₂F⁺. (Errors were uncertainty of primary electron energy for the ionization.) These values agreed with the literature values of 13.10 eV for CHF₂⁺^[29] and 14.43 eV for CH₂F⁺.^[29]

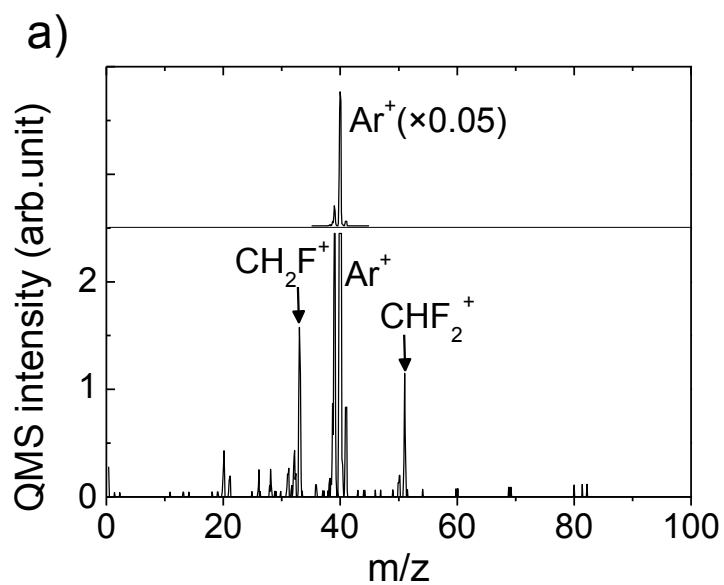


Fig .4.3 (a) Positive-ion mass spectra for the CH_2F_2 plasma diluted with pure Ar

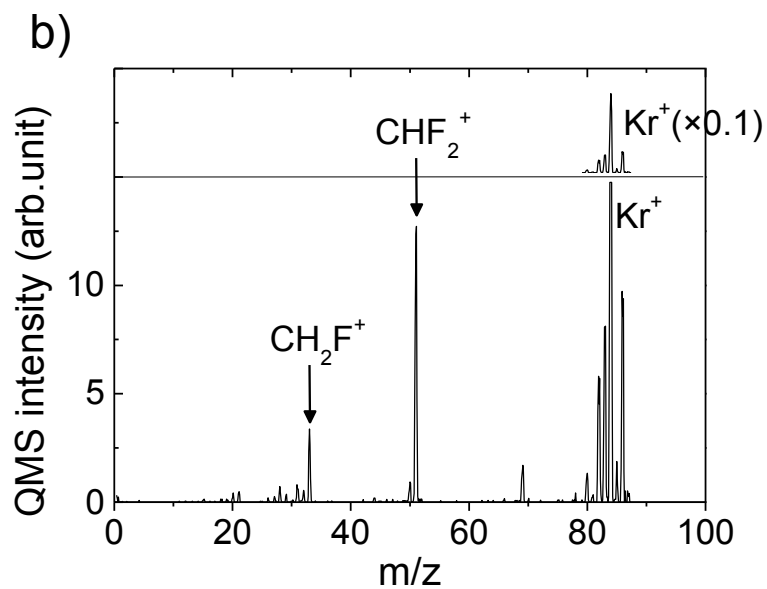


Fig .4.3 (b) Positive-ion mass spectra for the CH_2F_2 plasma diluted with pure Kr (b)

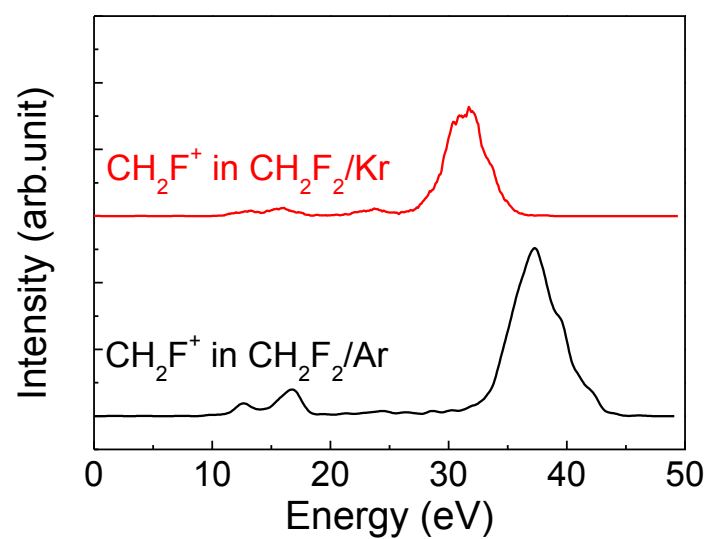


Fig .4.4 CHF_2^+ and CH_2F^+ produced by electron collision with CH_2F_2

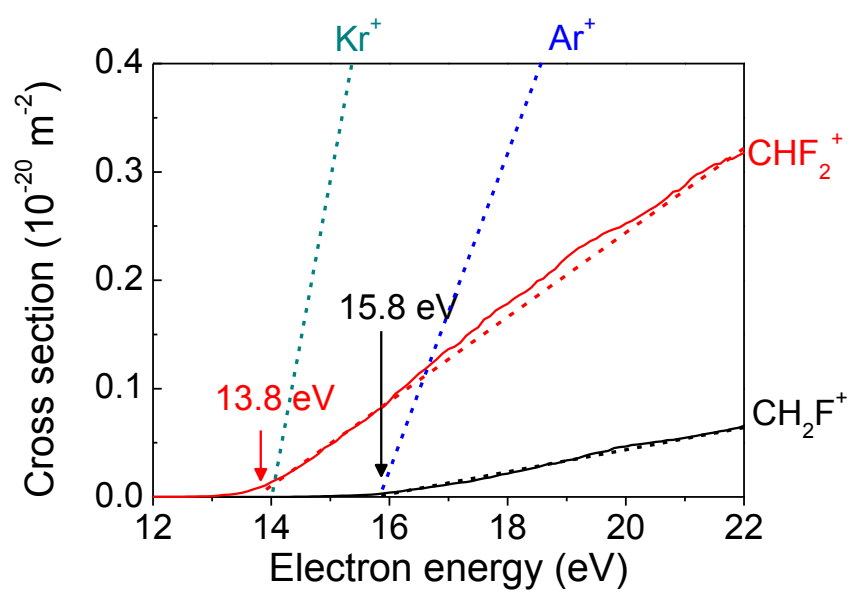


Fig .4.5 Cross sections of CHF_2^+ and CH_2F^+ produced by electron collision with CH_2F_2

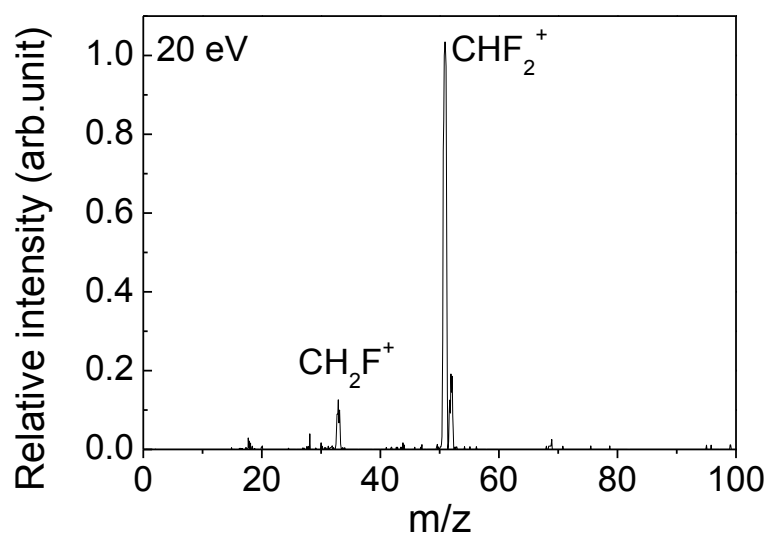


Fig .4.6 Positive-ion mass spectra for the CH_2F_2 obtained by electron impact at 20 eV.

Table 4.1 Relative intensities of positively charged ions in rare gas-diluted CH_2F_2 plasma

m/z	Species	Rare gas	
		Ar	Kr
31	CH_2F^+	8	2
52	CHF_2^+	2	14
40	Ar^+	100	0
84	Kr^+	0	57

Since C-H bonds dissociate more readily than C-F bonds, CHF_2^+ ions should be a major component of the fragmented ions from the CH_2F_2 parent gas. As seen in Figure 4.5, the dissociative ionization of electron impacts with lower energies showed always large cross section for CHF_2^+ generation as a major fragmented ion. In contrast, the CH_2F^+ ion was the major ion in Ar-diluted CH_2F_2 plasma. This dissociation behavior failed to explain the ion density in the Ar-diluted CH_2F_2 plasma. Thus other factors must be responsible for the generation of these ions.

Other ionization pathways and their channels are also of interest for understanding the complicated systems involved in the generation of reactive species in plasmas. For fluorocarbons, negative ion formation generally occurs through electron attachment pathways through relatively low energetic electron collisions at resonantly vertical transition energies for negative ion states.^[40,41] In the present study, for typical process plasmas with an electron energy of less than 5 eV,^[32] these channels were considered to contribute to the dissociation of parent CH_2F_2 molecules, because the population of low-energy electrons was large.

To determine the dependence of the electron temperature of Ar- or Kr-diluted plasmas on the dissociation of CH_2F_2 , the electron temperature was estimated from the trace rare gases optical emission data. The optical emission intensity, I for transition $A_j \rightarrow A_k$, at wavelength is given $\lambda_{j,k}$ by

$$I_{A_{j,k}} \propto n_g n_e 4\pi \int_0^\infty \sigma_{A_{j,k}}(v) v^3 f_e(v) dv, \quad (4.3)$$

where n_g is number density of the ground state, σ is the cross section at electron velocity, v , for electron impact excitation level A_j from A_k , n_e is electron density, and $f_e(v)$ is normalized electron velocity distribution function. Following this representation, the rate coefficient for electron impact processes including excitation, dissociation, and so on can be represented with using brackets as integration over whole electron velocities, and rewritten by

$$I_{A_{j,k}} \propto n_g n_e \langle \sigma v \rangle. \quad (4)$$

The $\langle \sigma v \rangle$ can be used as indicator called as the degree of excitation or dissociative ionization. If the electron velocity distribution function can be approximated by Maxwellian, an electron temperature, T_e , is obtained by optical emission intensities and plasma density through consideration of the actual $\langle \sigma v \rangle$. For simplification, the excitation degree for the trace Xe was estimated from the equation:

$$\langle \sigma v \rangle = I_{Xe} \cdot 1 / (n_e \cdot [Xe]) \quad , \quad (5)$$

where I_{Xe} is optical emission intensity for Xe, and $[Xe]$ is density of Xe.^[14] The plasma density, n_e , was measured by a plasma absorption probe (PAP).^[34] Experimental results for plasma densities were $1.6 \times 10^{11} \text{ cm}^{-3}$ for $\text{CH}_2\text{F}_2/\text{Ar}$ and $2.2 \times 10^{11} \text{ cm}^{-3}$ for $\text{CH}_2\text{F}_2/\text{Kr}$. Using the Xe emissions with transition of $5p^5 6s \rightarrow 5p^5 6p$ were 881.9 nm ($2p_8$), and 823.1 nm ($2p_6$), ratios of the $n_e \langle \sigma v \rangle$'s for Kr over Ar was estimated 0.69, and 0.82, respectively. (as shown in Figure 4.9) Combined with the cross-sections for excitation of each lines,^[38] these ratios were corresponded with difference in electron temperature of 0.4 eV, assumed Maxwellian electron temperature, e.g. for $\text{CH}_2\text{F}_2/\text{Ar}$ of 3.0 eV and for $\text{CH}_2\text{F}_2/\text{Kr}$ of 2.6 eV, respectively. The computed $\langle \sigma v \rangle$ with the literature cross-section for ionization of CH_2F_2 was only 15% difference between CH_2F and CHF_2 . Since the ionization energies are different for Ar (15.76 eV) and Kr (13.99 eV), the electron temperatures tended to be lower in Kr-diluted plasmas than in Ar-diluted plasmas. However, this result indicated that the electron-induced ionization was not the major pathway, because these experimental results were contradicted to consider only the electron collisions. A larger ion density for CH_2F^+ than that for CHF_2^+ implies that F atoms were generated more frequently than H atoms. However, this phenomenon was not observed in the Kr-diluted plasmas. Thus, other dissociation processes need to be considered.

Charge exchange collisions between rare gas ions and CH_2F_2 molecules occurred readily for CH_2F_2 plasmas.^[42] As shown in Figure 4.5, the threshold for dissociative

ionization for CHF_2^+ is similar to that for the C-H appearance (dissociative ionization) energy for CH_2F_2 (13.8 eV), the energy signal is located close to that for Kr (14 eV). In addition, the threshold for dissociative ionization for CH_2F^+ , which is the same as the C-F appearance energy for CH_2F_2 (15.8 eV), is close to that for Ar (16 eV). In the Kr-diluted plasma, the dissociative ionization of CHF_2^+ (C-H bond cleavage) occurred *via* charge exchange collisions of Kr^+ ions. The dissociative ionization of CH_2F^+ (C-F bond cleavage) selectively occurred *via* charge exchange collisions of Ar^+ ion in the Ar-diluted plasma.

For charge exchange collisions, Mizutani *et al.* observed peaks for ions at a lower energy than that for the sheath accelerating energy for entering the plasma-sheath edge in Ar-diluted fluorocarbon plasmas.^[43] This indicated that some ions were generated in the sheath region by collision of neutral gases with entering Ar ions. Thus, a charge exchange collision was proposed.^[43,44] In the present study, the ionization processes occurred in bulk plasmas; therefore this phenomenon should be considered along with other pathways.

To assess dissociative ionization in charge exchange collisions, Ar or Kr gas was used as a diluent. Figure 4.9 shows the dependence of plasma densities and $ne\langle\sigma v\rangle$ as indicator for the electron temperature on the Ar fraction ratio. As the amount of Ar increased, the plasma densities decrease and the electron temperature slightly increased, as described before. Figure 4.10 shows the dependence of the Ar^+ and Kr^+ ion densities (sum of all isotopes) and the fraction of CH_2F^+ and CHF_2^+ ion densities divided by the total CH_xF_y^+ ion intensity as a function of the ratio of Ar partial pressure over the total of Ar plus Kr. Total ion densities reflected the plasma density of $1.6\times 10^{11} \text{ cm}^{-3}$ for pure Ar vs. $2.2\times 10^{11} \text{ cm}^{-3}$ for pure Kr. As the amount of Ar increased, the Ar^+ ion density increased and the Kr^+ ion density decreased, with the inversion occurring at an Ar fraction of 70%, indicating complex behavior. The ion densities did not exhibit a linear relation. This behavior appeared to depend on the

electron temperature of the mixing conditions, *i.e.*, the plasma characteristics changed dramatically at an Ar fraction of 70%. Further study is needed to understand this result.

As shown in Figure 4.10, the decrease in the CHF_2^+ ion density was similar to the increase in the CH_2F^+ ion density as the Ar fraction increased. The relative CHF_2^+ ion density correlated with that for Kr^+ , which indicates that the effect of charge exchange collisions greatly influenced the density of CHF_2^+ and CH_2F^+ ions.

Lastly Figure 4.11 shows a dependence of radical density fraction, CH_2F and CHF_2 against all other CH_xF_y radicals on the rare gas mixture ratio, $\text{Ar}/(\text{Ar}+\text{Kr})$. The result shows that CH_2F radical is dominant. This can be interpreted that dissociation channels by excitation are more dissociative in $\text{CH}_2\text{F}_2 \rightarrow \text{CH}_2\text{F} + \text{F}$ compared with $\text{CH}_2\text{F}_2 \rightarrow \text{CHF}_2 + \text{H}$. These experimental results were supported by the quantum chemistry calculation^[40] and the vacuum UV absorption^[25]. As the $\text{Ar}/(\text{Ar}+\text{Kr})$ fraction ratio changed, the densities of CH_2F and CHF_2 decreased and increased vice versa. This phenomenon also failed to explain only electron collision induced with electron temperature changes in the Ar and Kr mixture ratios. For possible explanations, we suggest that Ar and Kr metastables contributes on dissociation via excitation. In the situation of large dilution by rare gas, the positive ions of rare gas were dominated in plasma. Thus the dissociative ionization rate with collisions of rare gas ions would be comparable to electron collision processes. Three processes of radical production, (1) dissociative ionization, (2) radical ionization, and (3) Penning (metastables) ionization are roughly considerable. By using cross-section data, with assumption of the electron temperature for 3.0 eV of Ar and for 2.6 eV of Kr, an estimated radical density fraction, $\text{CH}_2\text{F}/\text{CHF}_2$, can be explained as 0.3:0.1:0.6 for the three positive ion production processes respectively, in the best fit of the experimental results. More than the half of the radicals is possibly considered to be generated by the Penning ionization. Consequently, the Kr-diluted CH_2F_2 provides potentially CHF_2^+ , CHF_2 and H, as compared with CH_2F^+ , CHF_2 and F for the Ar-dilution. Figure 4.12 shows the

dependence of the fraction of CH_2F^+ and CHF_2^+ ion densities divided by the total CH_xF_y^+ ion intensity on the pressure of chamber. In this measurement, CH_2F_2 flow rate over Ar or Kr flow rate were fixed at 0.1 to keep same residence time. The ions ratio produced by charge exchange collisions were increased with increase of pressure in both plasmas. In higher pressure, the effects of charge exchange collisions are higher because of higher molecular density. Further investigation of the neutral radicals and negative ions generated in these interactions is required. Therefore, the control of the relative CHF_2^+ and CH_2F^+ ion densities in CH_2F_2 plasmas by adjusting the Ar and Kr content will be examined in future studies. In actual etching, not only the densities of CHF_2^+ and CH_2F^+ ions but also the densities of H, F, CHF_2 , and CH_2F radicals affect the selective etching of various dielectrics. Thus the controlling the ion density ratio may help to improve the performance of plasma etching. The results of the present study demonstrated a new concept for achieving highly precise control of plasma processing.

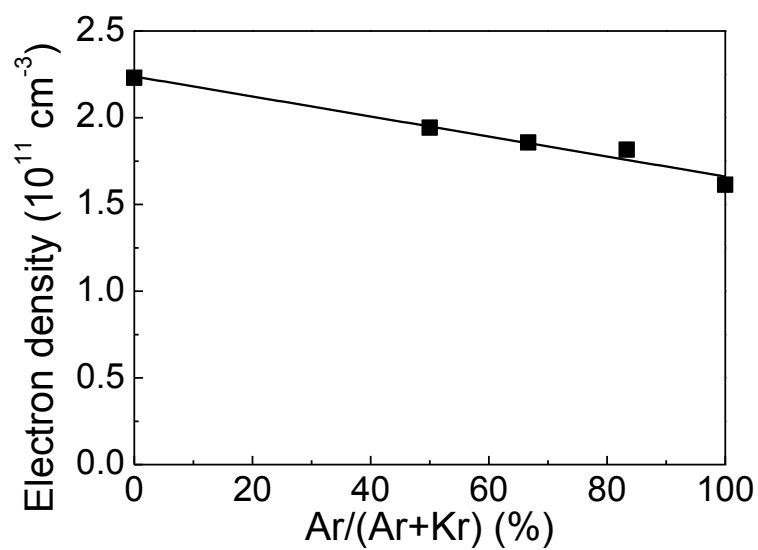


Fig .4.7 Dependence of electron density in $\text{CH}_2\text{F}_2/\text{Ar}/\text{Kr}$ plasma on Ar partial pressure

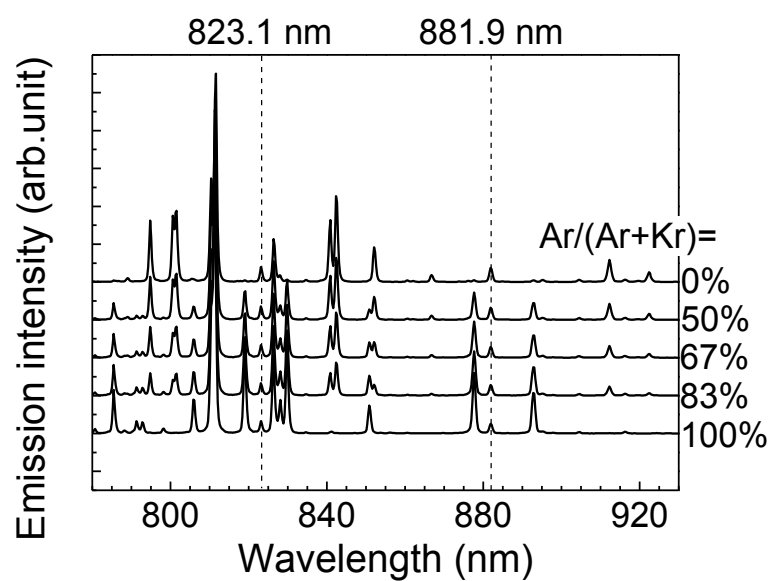


Fig .4.8 Optical emission spectra of $\text{CH}_2\text{F}_2/\text{Ar}/\text{Kr}$ plasma with tracer gas

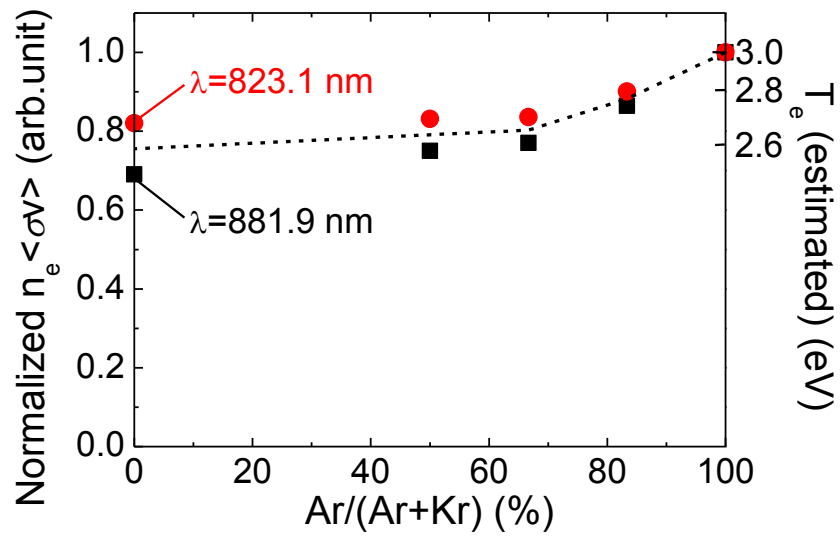


Fig .4.9 Dependence of plasma densities and $n_e \langle \sigma v \rangle$ as indicator for the electron temperature on the Ar fraction ratio

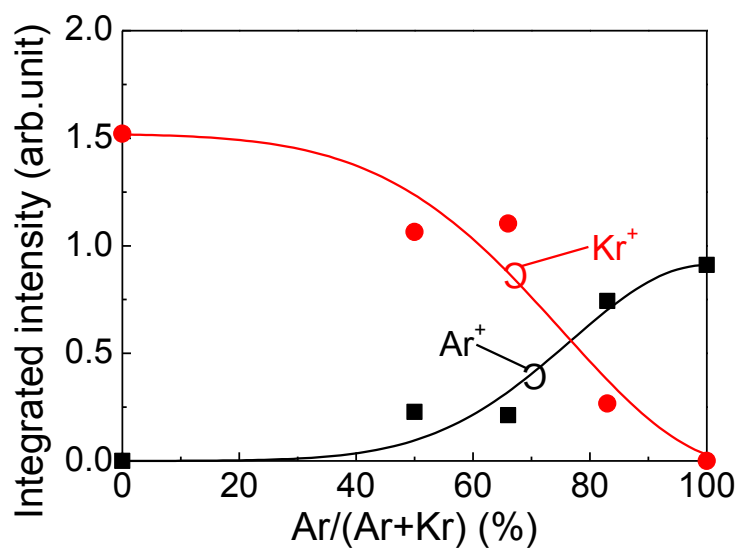


Fig .4.10 (a) Dependence of Ar^+ and Kr^+ ion density on the rare gas mixture ratio, $\text{Ar}/\text{Ar}+\text{Kr}$

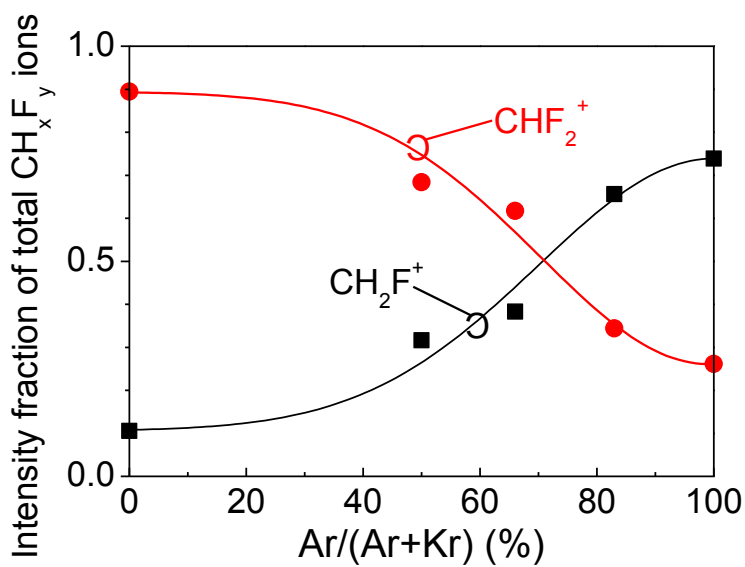


Fig .4.10 (b) Dependence of ion density fraction, CH_2F and CHF_2 against all other CH_xF_y radicals on the rare gas mixture ratio, $\text{Ar}/\text{Ar}+\text{Kr}$

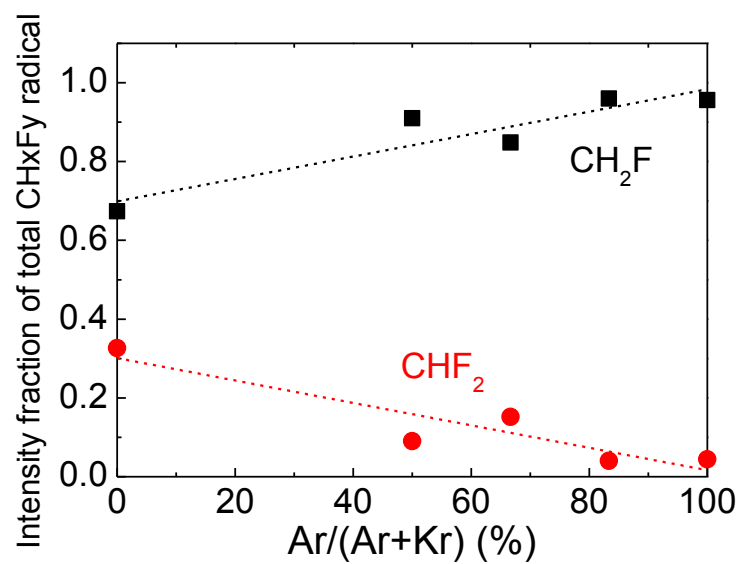


Fig .4.11 Dependence of ion density fraction, CH₂F and CHF₂ against all other CH_xF_y radicals on the rare gas mixture ratio, Ar/Ar+Kr

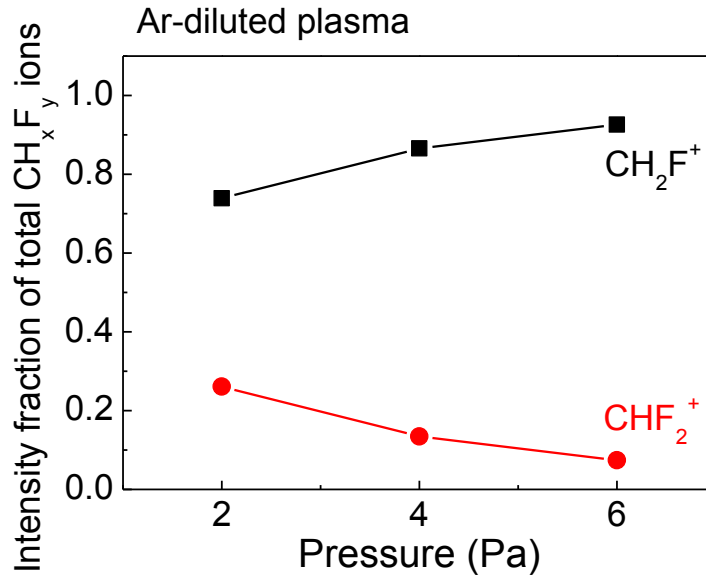


Fig. 4.12 (a) Dependence of the fraction of CH_2F^+ and CHF_2^+ ion densities divided by the total CH_xF_y^+ ion intensity on the pressure of chamber in $\text{CH}_2\text{F}_2/\text{Ar}$ plasma

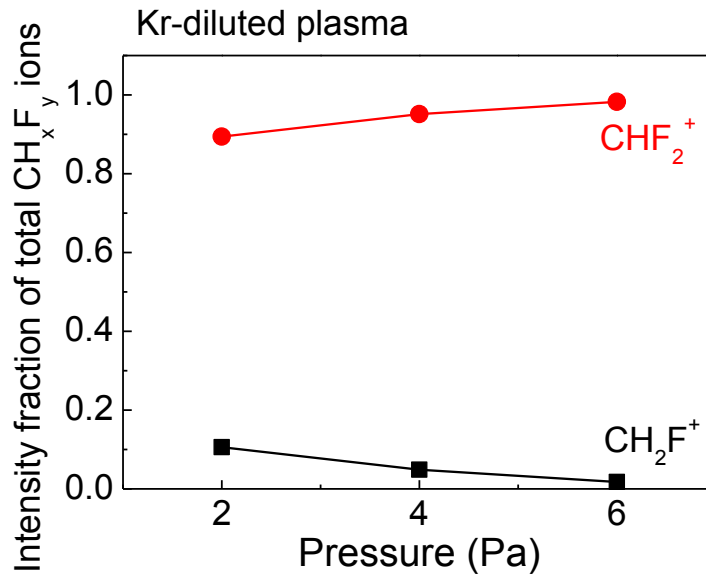


Fig. 4.12 (b) Dependence of the fraction of CH_2F^+ and CHF_2^+ ion densities divided by the total CH_xF_y^+ ion intensity on the pressure of chamber in $\text{CH}_2\text{F}_2/\text{Kr}$ plasma

4.3.3 Etch rate of SiO₂, Si₃N₄ and poly-Si by CH₂F₂/Ar/Kr plasma

Figure 4.13 shows etch rates of SiO₂, SiN and poly-Si films as a function of the flow rates of CH₂F₂ ranged between 5 and 50 sccm diluted 300-sccm-Ar gas. CH₂F₂/Ar plasma was generated under discharge conditions of 900 W VHF power to the upper electrode and 1000 W RF power to lower electrode, at 2 Pa. Under this condition, the electron energy was about 10^{11} cm^{-3} and the Vpp of lower electrode was -1000 V. At the lower CH₂F₂ flow rates below 15 sccm, the etch rates tended to increase as the flow rates increased. The etch rates were approximately 140 nm/min for SiN and 100 nm/min for poly-Si films, and 180 nm/min for SiO₂ at the CH₂F₂ flow rates of 10 sccm. As further increasing of flow rate, the poly-Si etch rates decreased, no etch depth for poly-Si was observed in the higher CH₂F₂ flow rate above 25 sccm. Meanwhile it is noticeably that the etch rate for SiN films increased and turned out to be faster than SiO₂. At the same time, in the case of poly-Si film, a polymeric film deposition occurred on the poly-Si film and no etching rate was observed. Henceforth we used the condition of high selective etching regime for SiN over Si films at a CH₂F₂ flow rate of 30 sccm.

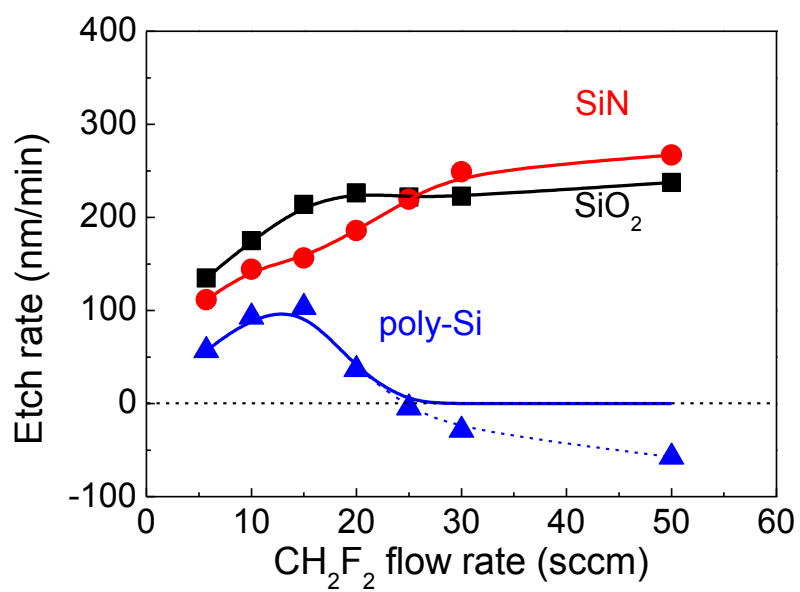


Figure. 4.13 Dependence of etch rates for SiO₂, SiN poly-Si in CH₂F₂ plasma diluted Ar on flow rate of CH₂F₂.

Previously, we examined that the dilutions with Ar and Kr gases characteristically modified the dissociation processes of CH_2F_2 , thus we discuss the impact of the reactive species on SiN etch reactions. Thicknesses of the deposited polymeric film on poly-Si films increased as the CH_2F_2 flow rates and differed at the different electron densities and electron temperatures of CH_2F_2 plasmas diluted Ar or Kr (data not shown). The deposited film thicknesses in the Kr diluted plasmas were apparently thicker than that in the Ar diluted plasmas. We believe that this polymeric film formation reflected the condition of change in incident species related to the surface reactions.

Generation of the reactive species and consideration for essential difference in the etch rates should be taken into account the electron density. For these, we measured electron densities by using the PAP. Under the condition of CH_2F_2 of 30 sccm, the VHF power changed from 600 to 1200 W. In the Ar dilution with the flow rate of 300 sccm, plasma densities were changed from 0.8 to $1.3 \times 10^{11} \text{ cm}^{-3}$. In the Kr dilution with the identical flow rate, plasma densities were changed from 1.1 to $1.8 \times 10^{11} \text{ cm}^{-3}$. The observed plasma densities were relatively larger in all the Kr dilution case than the Ar at identical VHF powers. This is explained by the large cross-sections for Kr ionization with the lower ionization energy (14.0 eV).

Figure 4.14 shows a dependence of etch rates for (a) SiO_2 and (b) SiN films in the plasma of a mixture of CH_2F_2 with flow rate of 30 sccm and Ar or Kr with the total flow rate of 300 sccm. The RF bias of 1000 W was applied and the peak-to-peak voltage (V_{pp}) was approximately 1 kV. As the VHF power changed in the range of 600 and 1200 W, the V_{pp} was not deviated under the conditions of Ar and also Kr dilution. As shown in Figure 4.14 (a), the SiO_2 etch rates were linearly increased with increasing of electron density. Commonly the etch rates were in proportion with a product of ion flux and ion etch yield at the determinant ion energy, i.e. a linear dependence of ion flux should be observed, when the constant V_{pp} were regarded as

obtaining the identical ion energy.^[45-47] An effective etching yield (a gradient in etch rate *versus* electron density) was estimated to be 0.4, which is fairly corresponded with literature data of 0.5 for CF^+ and 1.0 for CF_2^+ incidence at an energy of 1000 eV.³⁴⁾ Under the condition with V_{pp} of 1 kV and electron density of the order of 10^{11} cm^{-3} , a typical current density to the substrate was the order of $\text{mA cm}^{-2} \text{ s}^{-1}$, then the physical sputtering rate of SiO_2 was estimated to be approximately 100 nm/min. Actually as shown in Figure 4.13, the etch rates approached toward 100 nm/min, when CH_2F_2 flow rates decreased.

Furthermore, the etch rates for SiN in the Ar dilution case were always higher than that for the Kr dilution, in all cases changing of electron density as shown in Figure 4.14. Since the etching rates (ER) are in proportion to a multiplication of ion etch yield (EY) and ions fluxes $F_{ion} = (0.605 n_e \sqrt{T_e/m_i})$, where a product of the electron density (n_e) and a squared root term for the Bohm velocity, where T_e is electron temperature and m_i is mass of ion.^[45-47] Hence, the gradient of etch rates were given by $\text{ER} \propto \text{EY} \cdot F_{ion}$. As the T_e assumed to be 3 eV and n_e of 10^{11} cm^{-3} , the effective etch-yield (EY_{eff}) was roughly estimated from Figure 4.14 to be 0.27 for the Kr case and 0.45 for the Ar case.

Prior to discuss about these yields, we should note that Ar and Kr dilution of CH_2F_2 plasma provided the selective formation of CHF_2^+ or CH_2F^+ ions along with some possible contributions from counter fragments of H and F atoms on the basis of charge exchange dissociative ionization channels, $\text{CH}_2\text{F}_2 + \text{M}^+ \rightarrow \text{CH}_2\text{F}^+ + \text{F}\cdot + \text{M}^*$ and $\text{CHF}_2^+ + \text{H}\cdot + \text{M}^*$ ($\text{M}=\text{Ar, Kr}$). Namely, the dominant species in gas phase were CHF_2^+ ion and H atom in the Kr dilution case and CH_2F^+ ion and F atom in the Ar dilution case.

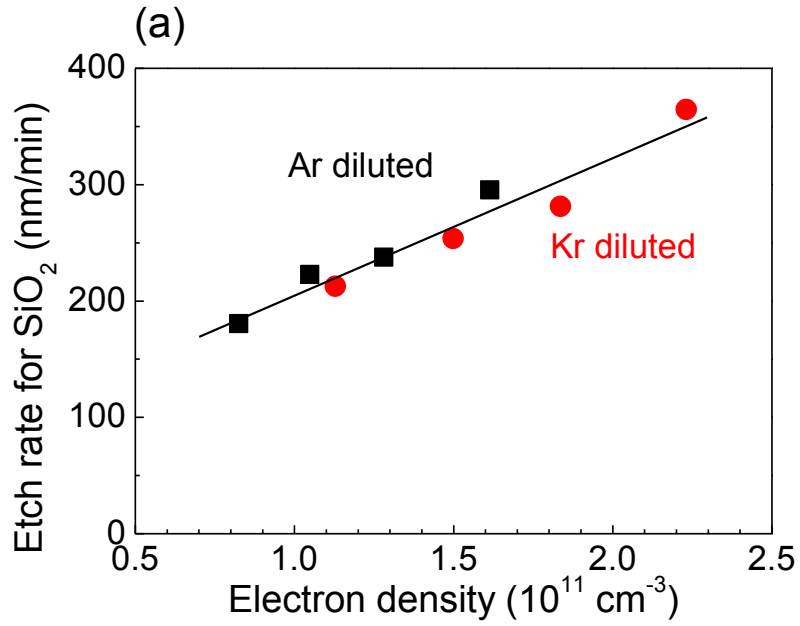


Fig 4.14 (a) Dependence of etch rates for SiO_2 on electron density changed by VHF power.

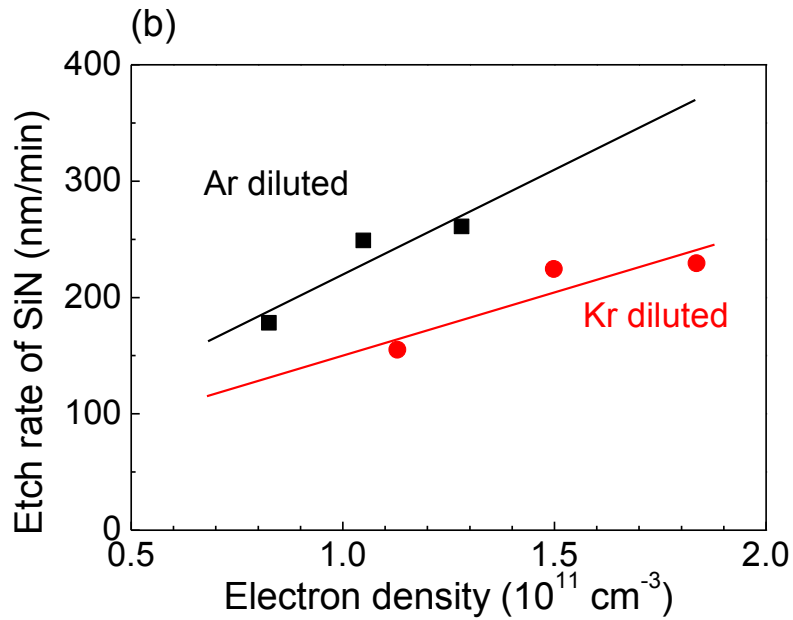


Fig 4.14 (b) Dependence of etch rates for SiN on electron density changed by VHF power.

Next, Figure 4.15 shows dependences of the RF bias power on the SiO₂ and SiN film etch rates. The results were obtained under the condition of electron density of $1.05 \times 10^{11} \text{ cm}^{-3}$ in the Ar or Kr diluted CH₂F₂ plasmas generated with the VHF power of 900 W for Ar and 500 W for Kr cases. The flow rate of CH₂F₂ was 30 sccm and dilution was done with the flow rate of 300 sccm for Ar or Kr. In the results shown in Figure 4.14, the dependence of RF bias power was confirmed to be negligibly small. For SiO₂, the behavior of etch rates on various RF power was represented as similar in the cases of Ar and Kr dilutions. On the other hand, no dependence of SiN etch rates on the RF bias power was observed the etch rates for SiN was saturated with the increase of the RF bias power. As the results, we pointed out that the observed difference in the Ar or Kr dilution was possibly resulted from the changes of the incident reactive species.

Moreover, the etch rates abruptly increased above the thresholds at the RF bias power around 100 W. The lower RF bias power processes tended to be improve the selectivity of SiN etch rate against SiO₂ etch rate. However, in the CH₂F₂ plasma diluted with Kr, the VHF power of 900 W, as shown in Figure 4.16, the SiO₂ etch rate was selectively occurred at the RF bias power at around 150 W. In this condition, the selectivity of SiO₂/SiN was around 6.5. In the CH₂F₂ plasma diluted with Ar, with the RF bias power ranged between 100 and 250 W, the selectivity of SiO₂/SiN was around 0.8.

The ion etch yields were reported that CF₂⁺ ion etch yield was 0.5 at 1000 eV for SiN,^[48] and CHF₂⁺ ion etch yield was 0.25 at 1000 eV.^[49] Ito *et al.* reported that the ion etch yields of CH₂F⁺ for SiN changed in response to the accumulated ion dosage.^[50] For the Kr case, the estimated EY_{eff} of 0.27 was fairly corresponded with the CHF₂⁺ EY of 0.25. On the other hand, the estimated EY_{eff} of 0.45 in the Ar case was discrepant, since the dominant ion was CH₂F⁺, was large. These EY values were only valid for pure ion processes. Therefore any other contribution of radicals on the surface reaction should be taken into consideration in details for the actual plasma etching

processes. In the SiN etching, both H and F atoms may work as etchant enhanced formation of volatiles such as HCN, and so forth. Thus the dominant species of H and F atoms, as well as CH_2F^+ and CHF_2^+ , might contribute to the surface reactions on SiN for the Ar case. The Ar dilution resulted in F-rich condition that might assist to enhance the etching of SiN film.

By analyzing of optical emissions, intensities for the optical emissions arisen from H and F atoms were investigated. Figure 4.17 shows I_{H} and I_{F} , referred to Xe emission, I_{Xe} , for optical emission from the CH_2F_2 plasma diluted with Ar or Kr. Previously, electron temperatures were estimated by using the optical emission data obtained by trace premixed addition of rare gases. The electron temperatures (T_{e}) were different. The T_{e} for Ar was higher approximately 0.4 eV than that for the Kr dilution. Thus the relative densities of H and F atoms should be estimated by the actinometric data referenced by the intensities of Xe as an actinometer. The I_{H} were almost unchanged to be 0.35 for Kr and 0.40 for Ar. However, the I_{F} of 0.25 for Ar was apparently different twice higher than that of 0.11 for Kr. This indicated that the F-rich condition in the Ar dilution consequently led to the increase of SiN etch rates.

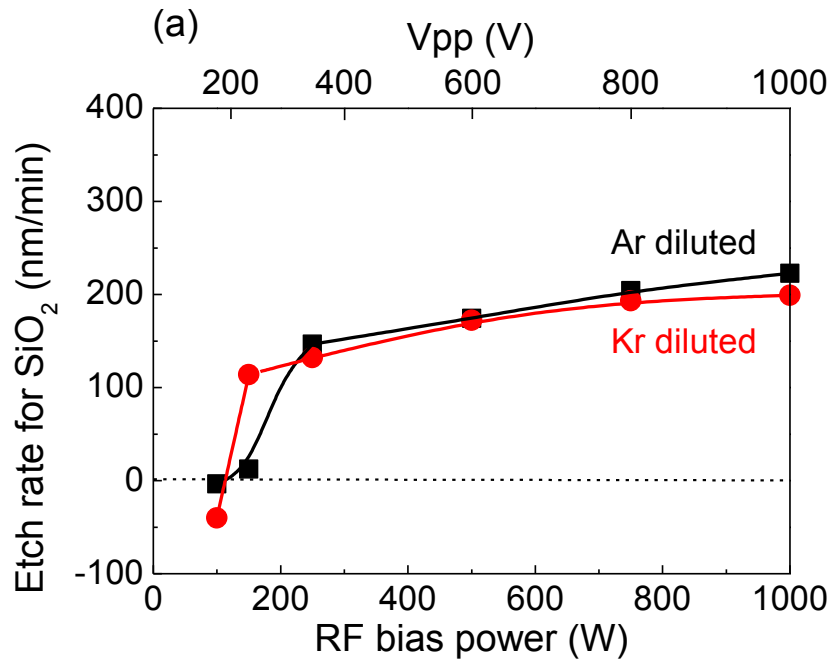


Fig 4.15 (a) Dependence of etch rates for on bias RF power ranged between 100 and 1000 W for Ar-diluted.

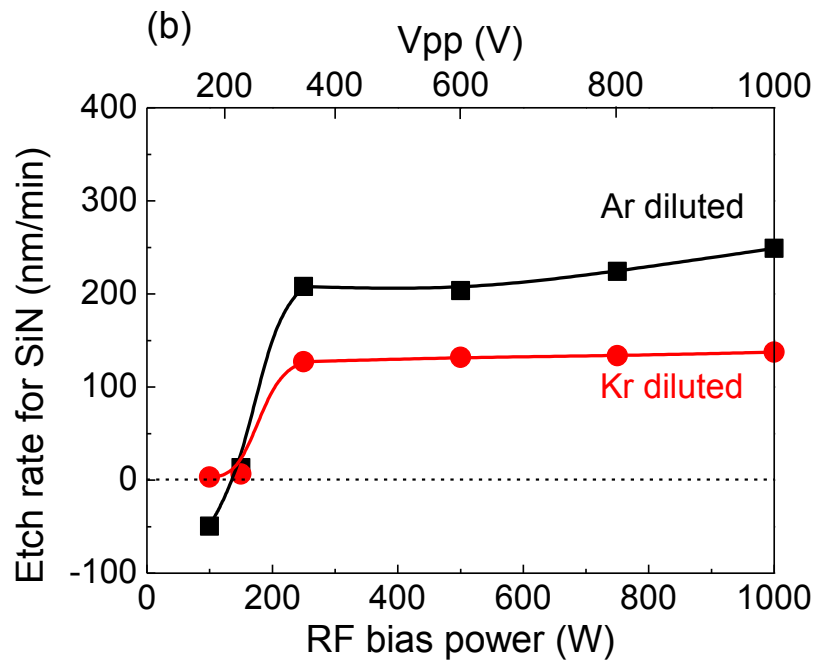


Fig 4.15 (b) Dependence of etch rates for on bias RF power ranged between 100 and 1000 W for Kr-diluted plasma.

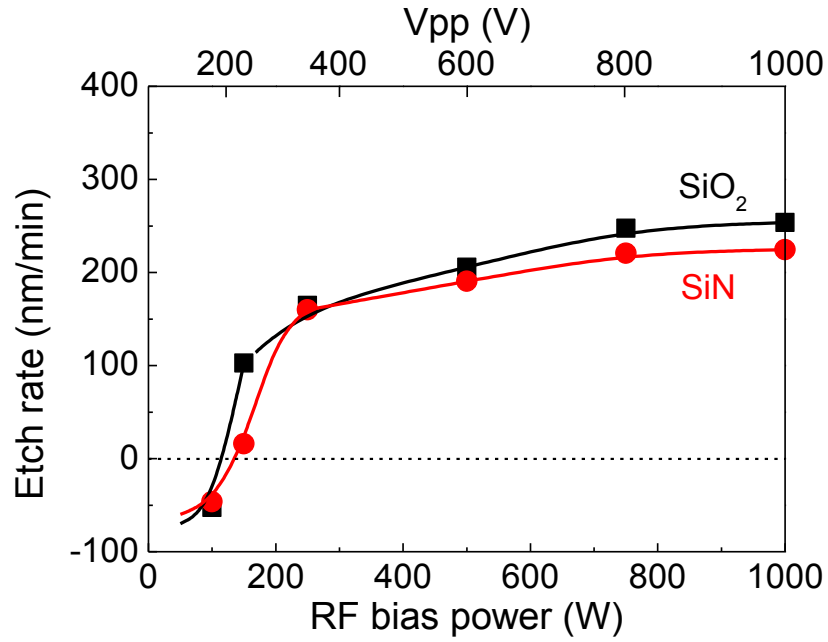


Fig 4.16 Dependence of etch rates for on bias RF power ranged between 100 and 1000 W for Kr-diluted plasma.

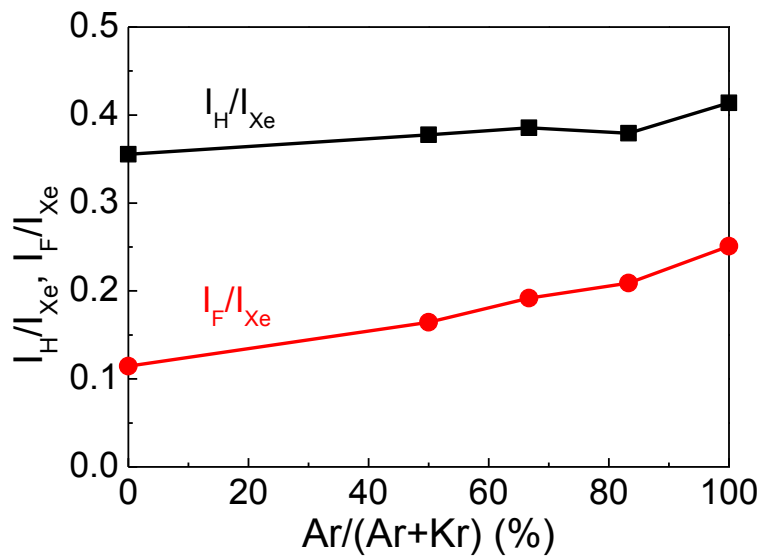


Fig 4.17 Dependence of the I_H/I_F ratio as a function of the ratio of Ar partial pressure over the total of Ar plus Kr

4.4 Conclusion

In this chapter, the C-H and C-F bond dissociation reactions of hydro-fluorocarbon were focused and characteristic CH_2F_2 selective dissociative ionization mechanism was focused.

The ion densities in CH_2F_2 plasmas diluted by Ar or Kr gas were examined using quadrupole mass spectrometry. CH_2F^+ were the dominant ions in a $\text{CH}_2\text{F}_2/\text{Ar}$ plasma, although dissociation of C-F bonds was less favorable in electron collisions than dissociation of C-H bonds. In contrast, in a $\text{CH}_2\text{F}_2/\text{Kr}$ plasma, large ion densities of CHF_2^+ due to dissociation of C-H bonds were observed. These results indicate that dissociative ionization by charge exchange collisions between CH_2F_2 and Ar^+ or Kr^+ affected the ion densities. Thus, the use of Ar and Kr to dilute CH_2F_2 plasma was demonstrated to control the charge exchange dissociative ionization channels and the selective formation of CHF_2^+ or CH_2F^+ ions, with possible contributions from counter fragments of H and F atoms.

The dependence of the etch rates of SiO_2 , SiN and poly-Si in the rare gas diluted CH_2F_2 plasmas on the flow rates of CH_2F_2 and the dilution gases of Ar or Kr was examined. For the CH_2F_2 plasma diluted Kr, the behavior of SiN etch rates could be explained by ion-induced processes for dominantly incident CHF_2^+ ion. On the other hand, in the CH_2F_2 plasma diluted Ar, the dominant incident species of F atom and $\cdot\text{CHF}_2$ radical other than CH_2F^+ ion enhanced to the etch reaction for SiN films.

It is assumed that the selective dissociative charge transfer collision reaction is shown from not only CH_2F_2 but also other molecules if these molecular dissociative ionization energy thresholds are around the molecular ionization energy of rare gas used for dilution. In addition, the metastable rare gas atom can effect on dissociation (especially dissociation to two neutral species). Therefore it is assumed that the ratio control of active species is possible by the select ion of feedstock gas molecules and a partial

pressure of rare gas.

4.5 Reference

- [1] M. Schaepkens, T. E. F. M. Standaert, N. R. Rueger, P. G. M. Sebel, G. S. Oehrlein, and J. M. Cook: *J. Vac. Sci. & Tec. A*, **17** (1999) 26.
- [2] B. S. Kwon, J. H. Lee, and N. E. Lee: *Thin Solid Films*, **519** (2011) 6741.
- [3] K. Miyata, M. Hori, and T. Goto: *J. Vac. Sci. & Tec. A*, **14** (1996) 2343.
- [4] K. Miyata, M. Hori, and T. Goto: *J. Vac. Sci. & Tec. A*, **15** (1997) 568.
- [5] A. M. Barklund, and H. O. Blom: *J. Vac. Sci. & Tec. A*, **11** (1993) 1226.
- [6] J. Givens, S. Geissler, J. Lee, O. Cain, J. Marks, P. Keswick, and C. Cunningham: *J. Vac. Sci. & Tec. B*, **12** (1994) 427.
- [7] K. Ueno, T. Kikkawa, and K. Tokashiki: *J. Vac. Sci. & Tec. B*, **13** (1995) 1447.
- [8] H. Hayashi, K. Kurihara, and M. Sekine: *Jpn. J. Appl. Phys.* **35** (1996) 2488.
- [9] S. Fang, C. Chiang, D. Fraser, B. Lee, P. Keswick, M. Chang, and K. Fung: *J. Vac. Sci. & Tec. A*, **14** (1996) 1092.
- [10] Y. Zhang, G. S. Oehrlein, and F. H. Bell: *J. Vac. Sci. & Tec. A*, **14** (1996) 2127.
- [11] M. Matsui, T. Tatsumi, and M. Sekine: *J. Vac. Sci. & Tec. A*, **19** (2001) 2089.
- [12] M. Fukasawa, A. Kawashima, N. Kuboi, H. Takagi, Y. Tanaka, H. Sakayori, K. Oshima, K. Nagahata, and T. Tatsumi: *Jpn. J. Appl. Phys.* **48** (2009) 08HC01.
- [13] Y. S. Choi, G. Lian, C. Vartuli, O. Olubuyide, J. Chung, D. Riley, and G. Baldwin: *IEEE Trans. Electron Devices*. **57** (2010) 2886.
- [14] Y. Miyawaki, Y. Kondo, M. Sekine, K. Ishikawa, T. Hayashi, K. Takeda, H. Kondo, A. Yamazaki, A. Ito, H. Matsumoto, and M. Hori: *Jpn. J. Appl. Phys.* **52** (2013) 016201.
- [15] T. Hayashi, K. Ishikawa, M. Sekine, and M. Hori: *Jpn. J. Appl. Phys.* **52** (2013) 05EB02.

- [16] H. K. Ryu, B. S. Lee, S. K. Park, I. W. Kim, and C. K. Kim: *Electrochem. Solid-State Lett.* **6** (2003) C126.
- [17] M. Darnon, T. Chevolleau, D. Eon, L. Vallier, J. Torres, and O. Jouber: *J. Vac. Sci. & Tec. B*, **24** (2006) 2262.
- [18] C. K. Park, H. T. Kim, C. H. Lee, N. E. Lee, and H. Mok: *Microelectro. Eng.* **85** (2008) 375.
- [19] L. Chen, L. Xu, D. Li, and B. Lin: *Microelectro. Eng.* **86** (2009) 2354.
- [20] J. S. Kim, B. S. Kwon, W. Heo, C. R. Jung, J. S. Park, J. W. Shon, and N.-E. Lee: *J. Vac. Sci. & Tec. A*, **28** (2010) 65.
- [21] J. W. Coburn and H. F. Winters: *J. Vac. Sci. & Tec.* **16** (1979) 391.
- [22] Y. Iijima, Y. Ishikawa, C. I. Yang, M. Chang, and H. Okano: *Jpn. J. Appl. Phys.* **36** (1997) 5498.
- [23] P. Wagner, and A. B. F. Duncan: *J. Am. Chem. Soc.* **77** (1955) 2609.
- [24] P. Sauvageau, R. Gibert, P. P. Berlow, and C. Sandorfy: *J. Chem. Phys.* **59** (1973) 762.
- [25] D. P. Secombe, R. Y. L. Chim, R. P. Tuckett, H. W. Jochims, and H. Baumgartel: *J. Chem. Phys.* **114** (2001) 4058.
- [26] C. Lifshitz, and F. A. Long: *J. Chem. Phys.* **69** (1965) 3741.
- [27] M. Barber, J. D. Clark, A. Hinchliffe, and S. Mann: *Chem. Phys. Lett.* **44** (1976) 526.
- [28] I. Torres, R. Martínez, M. N. Sánchez Rayo, J. A. Fernández, and F. Castaño: *J. Phys. B. At. Mol. Opt. Phys.* **32** (1999) 5437.
- [29] I. Torres, R. Martínez, M. N. Sánchez Rayo, and F. Castaño: *J. Phys. B. At. Mol. Opt. Phys.* **33** (2000) 3615.

- [30] I. Torres, R. Martínez, M. N. Sánchez Rayo, and F. Castaño: J. Chem. Phys. **115** (2001) 4041.
- [31] M. T. do N. Varella, C. Winstead, V. McKoy, M. Kitajima, and H. Tanaka: Phys. Rev. A, **65** (2002) 022702.
- [32] M. A. Mansour ElSabbagh, M.D. Bowden, K. Uchino, and K. Muraoka: Appl. Phys. Lett. **78** (2001) 3187.
- [33] K. Stephan, H. Helm, and T. D. Märk: J. Chem. Phys. **73** (1980) 3763.
- [34] H. Kokura, K. Nakamura, I. P. Ghanashev, and H. Sugai: Jpn. J. Appl. Phys. **38** (1999) 5262.
- [35] T. Yamaguchi, T. Komuro, C. Koshimizu, S. Takashima, K. Takeda, H. Kondo, K. Ishikawa, M. Sekine, and M. Hori: J. Phys. D: Appl. Phys. **45** (2012) 025203.
- [36] M. V. Malyshev, and V. M. Donnelly: J. Vac. Sci. Technol. A **15** (1997) 550.
- [37] M. V. Malyshev, and V. M. Donnelly: Phys. Rev. E. **60** (1999) 6016.
- [38] V. M. Donnelly: J. Phys. D: Appl. Phys. **37** (2004) R217.
- [39] Z. Chen, V. M. Donnelly, D. J. Economou, L. Chen, and Merritt Funk: J. Vac. Sci. & Tec. A, **27** (2009) 1159.
- [40] T. Hayashi, K. Ishikawa, M. Sekine, and M. Hori: unpublished.
- [41] T. Hayashi, S. Murai, F. Sato, A. Kono, N. Mizutani, and K. Suu: Jpn. J. Appl. Phys. **50** (2011) 08KB01.
- [42] M. Tsuji, T. Funatsu, H. Kouno, and Y. Nishimura: J. Chem. Phys. **97** (1992) 8216.
- [43] N. Mizutani, and T. Hayashi: Thin Solid Film. **374** (2000) 167.
- [44] T. Hayashi, M. Miyamura, and S. Komiya: Jpn. J. Appl. Phys. **21** (1982) L755.
- [45] T. Tatsumi, H. Hayashi, S. Morishita, S. Noda, M. Okigawa, N. Itabashi, Y. Hikosaka, and M. Inoue: Jpn. J. Appl. Phys. **37** (1998) 2394.

- [46] T. Tatsumi, Y. Hikosaka, S. Morishita, M. Matsui, and M. Sekine: J. Vac. Sci. & Tec. A, **17** (1999) 1562.
- [47] T. Tatsumi, M. Matsui, M. Okigawa, and M. Sekine: J. Vac. Sci. & Tec. B, **18** (2000) 1897.
- [48] K. Yanai, K. Karahashi, K. Ishikawa, and M. Moritaka: J. Appl. Phys. **97** (2005) 053302.
- [49] K. Karahashi, K. Yanai, K. Ishikawa, H. Tsuboi, K. Kurihara, and M. Nakamura: J. Vac. Sci. & Tec. A, **22** (2004) 1166.
- [50] T. Ito, K. Karahashi, M. Fukasawa, T. Tatsumi, and S. Hamaguchi: J. Vac. Sci. & Tec. A, **29** (2011) 050601.

Chapter 5 Conclusions and Future Works

5.1 Conclusion of Present Research

The motivation of this dissertation is the clarifications of the control of active species in plasma by gas molecular structures or dissociation and the effects of dissociated reactive species on dielectric film etching processes. To achieve this goal, the author investigated the dissociation reaction of fluorocarbon contained oxygen or hydrogen by measurement of plasma and fragments induced by electron impact from gas molecules and the molecular orbital calculations.

In chapter 1, the trend in the future scaled integrated circuits and the requirement for plasma etching technologies has been shown as an introduction. The development and selections of fluorocarbon molecules for achieving required etch properties was also introduced.

In chapter 2, theory of plasma diagnostics for mass spectrometry and computation method of molecular orbital calculations used for the investigation of molecular dissociation were introduced. Theories of film characterization techniques such as XPS and optical interferometer used as measurement methods of etched subsurface reactions were also described.

In chapter 3, the fluorocarbons contained oxygen as an ether bond, PMVE ($\text{C}_3\text{F}_6\text{O}$, perfluoro-ethyl-vinyl-ether) and PPVE ($\text{C}_5\text{F}_{10}\text{O}$, perfluoro-propyl-vinyl-ether), were investigated and calculated to clarify dissociation reaction of ether structure. The dissociative ionization and electron attachment reactions of a PMVE isomer were examined using quadrupole mass spectrometry. The most abundant CF_3^+ ions were generated by dissociative ionization at a threshold energy of around 10.2 eV, and the second most abundant positive ions were $\text{C}_2\text{F}_2\text{O}^+$. These data suggest rearrangement of the F atom to form CF_4 . Generation of the abundant negative ions, $\text{C}_2\text{F}_3\text{O}^-$, was

confirmed by calculation of the potential energy curves for electron attachment along the reaction coordinate on both sides of the ether C–O bond. Only dissociative electron attachment was involved in $\text{C}_2\text{F}_3\text{O}^-$ ion generation. The dissociative ionization and electron attachment reactions of a PPVE isomer were examined using quadrupole mass spectrometry. The major positive ion was CF_3^+ . A minority of positive and negative ions, involving $\text{C}_2\text{F}_2\text{O}^+$, $\text{C}_2\text{F}_3\text{O}^-$ and $\text{C}_3\text{F}_7\text{O}^-$, were observed. The appearance energies causing the dissociative ionization were around 14.5 eV for CF_3^+ and 11.8 eV for C_3F_7^+ ions. Each reaction channel was confirmed by the potential energy curves provided in the quantum chemical calculations. Combined with the previous research on the $\text{C}_3\text{F}_6\text{O}$ isomer the observed ion efficiencies for the CF_3^+ ion were larger, on the order of 10^{-20} cm^{-2} , compared with the order of only 10^{-21} cm^{-2} for the other channels. This is attributed to the excess energy of energetic electron impacts being distributed among internal energies of CF_3^+ with stabilization of the ionizing charge by delocalization onto the vinyl ether bond. Overall, perfluoro-vinyl ethers characteristically generated CF_3^+ as the largest abundant ion. This information may be useful for controlling the generation of fluorocarbon ions and in the design of molecules containing a vinyl-ether.

In chapter 4, the C–H and C–F bond dissociation reactions of hydro-fluorocarbon were focused and characteristic CH_2F_2 selective dissociative ionization mechanism was focused. The ion densities in CH_2F_2 plasmas diluted by Ar or Kr gas were examined using quadrupole mass spectrometry. CH_2F_2^+ were the dominant ions in a $\text{CH}_2\text{F}_2/\text{Ar}$ plasma, although dissociation of C–F bonds was less favorable in electron collisions than dissociation of C–H bonds. In contrast, in a $\text{CH}_2\text{F}_2/\text{Kr}$ plasma, large ion densities of CHF_2^+ due to dissociation of C–H bonds were observed. These results indicate that dissociative ionization by charge exchange collisions between CH_2F_2 and Ar^+ or Kr^+ affected the ion densities. Thus, the use of Ar and Kr to dilute CH_2F_2 plasma was demonstrated to control the charge exchange dissociative ionization channels and the

selective formation of CHF_2^+ or CH_2F^+ ions, with possible contributions from counter fragments of H and F atoms.

The dependence of the etch rates of SiO_2 , SiN and poly-Si in the rare gas diluted CH_2F_2 plasmas on the flow rates of CH_2F_2 and the dilution gases of Ar or Kr was examined. For the CH_2F_2 plasma diluted Kr, the behavior of SiN etch rates could be explained by ion-induced processes for dominantly incident CHF_2^+ ion. On the other hand, in the CH_2F_2 plasma diluted Ar, the dominant incident species of F atom and $\cdot\text{CHF}_2$ radical other than CH_2F^+ ion enhanced to the etch reaction for SiN films. It is assumed that the selective dissociative charge transfer collision reaction is shown from not only CH_2F_2 but also other molecules if these molecular dissociative ionization energy thresholds are around rare gas molecular ionization energy. In addition, the metastable rare gas atom can effect on dissociation (especially dissociation to two neutral species). Therefore it is assumed that the control of active species ratio is possible if select feedstock gas molecules and a partial pressure of rare gas.

5.2 Future scope

In this dissertation, the dissociation of fluorocarbon gas molecules contained oxygen or hydrogen and the control of active species from these molecule in plasma were studied based on plasma diagnostics, measurement of fragmentation and computation method for etching process. To control plasma etch process and achieve high etch properties, it is necessary to understand the relationship between feedstock gas and active species in plasma, and active species in plasma and surface reactions. For the future etch process, the accuracy of etch pattern achieve only around 10 atoms scale. Thus a little change of active species lead to defective products. The complex structures of device such as 3-dimentional structure and air gap have been already used for ULSI. Therefore it is necessary to sensitive control of active species and etch process.

Various fluorocarbon molecules have been developed for high etch properties such as high selectively, high etch rate and fine profile. These developments have been performed by trial-and-error method. To become easy developments of fluorocarbon molecules, it is necessary to feed back the dissociation data and etch process data to development region. In this study, the possibility of selective dissociation molecular structure was shown. This information would help the development of designed gas molecules. Also, in this study, it was found that there are selective dissociation reactions at specific bond in plasma by relationship between rare gas and feedstock gas. The combination of gas design and selective dissociation reactions in plasma leads to more controllable plasma.

Etch processes depend on active species in plasma strongly. In this study, I focused on the production of active species from feedstock gas. However the relationship between active species and surface, another important piece for controlling etch processes, is not understood well. To clarify the relationship between active species and surface,

beam method and plasma diagnostics have been used. If a lot of the relationship between feedstock gas and active species in plasma, and active species in plasma and surface reactions will be understood, veracious model of plasma reaction can be constructed. Veracious model is useful for understanding plasma conditions easily and control etch processes.

In near future, using the designed feedstock gas and plasma model, the control of active species in plasma for achieve required etching process is possible. The measurement and calculation of molecular dissociation would be expected to accelerate development for plasma etching process.

Acknowledgements

The present research has been performed in Prof. Hori and Prof. Sekine Laboratory, Department of Electrical Engineering and Computer Science, Nagoya University. The research results presented in this thesis could not have been obtained without the support of the following people.

First and foremost, I would like to express my deep appreciation to Prof. Masaru Hori, Institute of Innovation for Future Society, Nagoya University, for having given me the opportunity to pursue a Ph.D. in his group. I could not progress rapidly in my understanding of this research without his guidance, valuable advices, and encouragements.

I would also like to deeply appreciate my co-supervisor, Prof. Makoto Sekine, Plasma Nanotechnology Research Center, Nagoya University, for providing his wealth of experience and wonderful discussions. I would like to thank the vice-adviser Prof. Hirotaka Toyoda, Department of Electrical Engineering and Computer Science, Nagoya University and also the vice-adviser Prof. Tatsuru Shirafuji, Department of Physical Electronics and Informatics, Osaka city University, for giving me worth advice and discussions.

I would like to acknowledge Semiconductor Research Corporation for their fruitful discussion and financial support.

I am also grateful to the entire staff in Hori and Sekine's Lab., Associate Prof. Hiroki Kondo, Assistant Prof. Keigo Takeda, Dr. Lu Yi, and Dr. Hyung Jun Cho, the entire staff in Plasma Nanotechnology Research Center, Prof. Kenji Ishikawa, Prof. Toshio Hayashi, Associate Prof. Satomi Tajima, Prof. Hitoshi Ito, and Prof. Hiromasa Tanaka, the entire staff in Venture Business Laboratory, Dr. Yudai Miyawaki for their fruitful discussion and valuable comments.

I would like to express my gratitude to Prof. Masafumi Ito, Department of

Acknowledgements

Electrical and Electronic Engineering, Meijo University, Prof. Mineo Hiramatsu, Department of Electrical and Electronic Engineering, Meijo University, Associate Prof. Takayuki Ohta, Department of Electrical and Electronic Engineering, Meijo University, and Dr. Masanaga Fukasawa, Sony corporation.

I would like to acknowledge Dr. Shoji Den, Dr. Koji Yamakawa, Dr. Shunji Takahashi in Katagiri Engineering Co., Ltd., Dr. Hiroyuki Kano in NU Eco-Engineering Co., Ltd., for constructing and modifying the experimental equipments.

The author thanks sincerely Mr. Minyoung Ahn, Mr. Tatsuya Komuro, Mr. Haoran Wang, and Mr. Naoki Yoshitake who aided their experimental works carried out on my researches and also expressed their valuable suggestions and discussions.

A big thanks to my colleagues in Prof. Hori and Prof. Sekine's Lab, Dr. Wakana Takeuchi, Dr. Chang Soon Moon, Dr. Shingo Kondo, Dr. Tsuyoshi Yamaguchi, Dr. Hirotoshi Inui, Dr. Hiroshi Yamamoto, Dr. Arkadiusz Malinowski, Dr. Shang Chen, Dr. Yusuke Abe, Dr. Takuya Takeuchi, Dr. Takehiro Hiraoka, Dr. Hitoshi Watanabe, Dr. Hironao Shimoeda, Dr. Toshiya Suzuki, Ms. Sachiko Iseki, Mr. Tetsuya Kimura, Mr. Hiroki Kuroda, Mr. Kota Mase, Mr. Yuto Matsudaira, Mr. Hiroyuki Mikuni, Mr. Sho Kawashima, Mr. Tokushige Kino, Mr. Shinpei Amasaki, Mr. Koji Yasuda, Mr. Masanori Kato, Mr. Naoya Sumi, Mr. Tatsuya Hagino, Mr. Takayuki Kanda, Mr. Jong Yun Park, Mr. Takayoshi Tsutsumi, Mr. Kohei Asano, Mr. Jun Kuki, Mr. Ryosuke Kometani, Mr. Atsushi Fukushima, Mr. Takeyoshi Horibe, Ms. Ya Lu, Mr. Leyong Yu, Mr. Tomohiro Takahashi, Mr. Jiadong Cao, Mr. Kuangda Sun, Mr. Zecheng Liu, Mr. Makoto Isobe, Mr. Tomoki Amano, Mr. Takashi Kako, Mr. Ryo Gonda, Mr. Masayuki Nakamura, Mr. Keita Miwa, Ms. Sijie Liang, Mr. Da Xu, Mr. Harry Zhang, Mr. Shun Imai, Mr. Kazuki Iwamoto, Mr. Takumi Kumakura, Mr. Naoyuki Kurake, Mr. Hirotugu Sugiura, Mr. Yusuke Fukunaga, Mr. Takumi Ito, Mr. Kazuaki Kojima, Mr. Peter Pan, Mr. Takuya Kurihara, Mr. Shunichi Sato, Mr. Shinnosuke Takai, Mr. Takuya

Acknowledgements

Tonami, Mr. Kenichi Naito and Mr. Ryo Furuta for giving the big pleasure in life and creating a most enjoyable work atmosphere.

I also appreciate the enough secretarial supports to Ms. Tomoko Yokoi, Ms. Rie Nozaki, Ms. Megumi Oshigane, Ms. Azusa Ohta, Ms. Rieka Kamiya, Ms. Naoko Kataoka, Ms. Masako Takahashi, Ms. Mitsuko Era, Ms. Machiko Sakai, Ms. Yukie Kase, Ms. Yoko Kuwahara, Ms. Chagay Alena, Ms. Asako Nishiyama and Ms. Kanae Teshigawara for helping me to concentrate on the research without any problem of administrative task.

Finally, I would like to dedicate this thesis to my parents, my sisters, and good friends.

Yusuke Kondo

January 2015

Acknowledgements

List of Papers

1. Original Papers

	<i>Title</i>	<i>Journal</i>	<i>Authors</i>
1	Hydrofluorocarbon ion density of argon- or krypton-diluted CH_2F_2 plasmas: Generation of CH_2F^+ and CHF_2^+ by dissociative-ionization in charge exchange collisions	Journal of Physics D: Applied Physics. 48 (2015) 045202.	Yusuke Kondo, Yudai Miyawaki, Kenji Ishikawa, Toshio Hayashi, Keigo Takeda, Hiroki Kondo, Makoto Sekine, and Masaru Hori
2	CF_3^+ fragmentation by electron impact ionization of perfluoro-propyl-vinyl-ethers, $\text{C}_5\text{F}_{10}\text{O}$, in gas phase	Japanese Journal of Applied Physics. 54 (2015) 040301.	Yusuke Kondo, Kenji Ishikawa, Toshio Hayashi, Yudai Miyawaki, Keigo Takeda, Hiroki Kondo, Makoto Sekine, and Masaru Hori
3	Silicon nitride (SiN) etch performance of CH_2F_2 plasmas diluted argon or krypton	Japanese Journal of Applied Physics. 54 (2015) 040303.	Yusuke Kondo, Kenji Ishikawa, Toshio Hayashi, Yudai Miyawaki, Keigo Takeda, Hiroki Kondo, Makoto Sekine, and Masaru Hori

2. International Conferences

	<i>Title</i>	<i>Conference</i>	<i>Authors</i>
1	SiO ₂ Plasma Etching Process Using Alternative Gas, C ₃ F ₆ O	3rd International Symposium on Advanced Plasma Science and its Applications for Nitrides and Nanomaterials, Nagoya, Japan, March 6-9, 2011.	Y. Kondo, Y. Miyawaki, K. Takeda, K. Ishikawa, H. Kondo, T. Hayashi, H. Okamoto, M. Sekine and M. Hori
2	Chemical Modeling of Etch Process Using C ₃ F ₆ O Alternative Gas	The 4th International Conference on PLAsma-Nano Technology & Science, Gifu, Japan, Mar. 10-12, 2011.	Y. Kondo, Y. Miyawaki, K. Takeda, K. Ishikawa, H. Kondo, T. Hayashi, H. Okamoto, M. Sekine and M. Hori,
3	Modeling of C ₃ F ₆ O/Ar Plasma Chemistry for SiO ₂ Etching Processes	The 8th Asian-European International Conference on Plasma Surface Engineering, China, September 19-22, 2011	Y. Kondo, Y. Miyawaki, K. Takeda, K. Ishikawa, H. Kondo, T. Hayashi, M. Sekine and M. Hori
4	Mechanism of generating ions and radicals in C ₃ F ₆ O plasma	The 14th International Workshop on Advanced Plasma Processing and Diagnostics, Fukuoka, Japan, January 7-8, 2012.	Y. Kondo, Y. Miyawaki, K. Takeda, K. Ishikawa, H. Kondo, T. Hayashi, M. Sekine and M. Hori
5	Mechanism of generating ions and radicals in C ₃ F ₆ O plasma	4th International Symposium on Advanced Plasma Science and its Applications for Nitrides and Nanomaterials Aichi, Japan, March 4-8, 2012.	Y. Kondo, Y. Miyawaki, K. Takeda, K. Ishikawa, H. Kondo, T. Hayashi, M. Sekine and M. Hori

List of papers

	<i>Title</i>	<i>Conference</i>	<i>Authors</i>
6	Reaction mechanism of plasma etching using hydrogen-containing fluorocarbon gas	The 15th Korea-Japan workshop for Advanced Plasma Process and Diagnostics, Sungkyunkwan University, Korea, June 7-8, 2012	Y. Kondo, Y. Miyawaki, K. Ishikawa, T. Hayashi, M. Sekine, K. Takeda, H. Kondo and M. Hori
7	Mechanism of generating ions and radicals in fluorocarbon plasma investigated by reaction model analysis	AVS 59th International Symposium & Exhibition, Oct.28-Nov. 2, 2012	Y. Kondo, Y. Miyawaki, K. Takeda, H. Kondo, K. Ishikawa, T. Hayashi, M. Sekine, and M. Hori
8	Generation Mechanism of Ions and Radicals in CH _x F _y Etching Plasmas	The 11th APCPST and 25th SPSM , Kyoto University ROHM Plaza, Kyoto, Japan, Oct. 2-5, 2012	Y. Kondo, Y. Miyawaki, K. Takeda, H. Kondo, K. Ishikawa, T. Hayashi, M. Sekine, and M. Hori
9	Gas-phase reaction model of Ar-diluted CH _x F _y plasmas	5th International Symposium on Advanced Plasma Science and its Applications for Nitrides and Nanomaterials, Aichi, Japan, January 28-February 1, 2013	Y. Kondo, Y. Miyawaki, K. Takeda, H. Kondo, K. Ishikawa, T. Hayashi, M. Sekine, and M. Hori
10	Effects of hydrogen contained in fluorocarbon gas molecules for dielectric film etching proces	The 6th International Conference on PLAsma Nano Technology & Science, Gero Synergy Center 'ACTIVE', Gero-city, JAPAN, Feb. 2-3, 2013	Y. Kondo, Y. Miyawaki, K. Takeda, K. Ishikawa, H. Kondo, T. Hayashi, M. Sekine, and M. Hori

List of papers

	<i>Title</i>	<i>Conference</i>	<i>Authors</i>
11	Control of Gas Phase Reaction in Etching Plasmas Employing Hydro-fluorocarbon Gases	Dry Process Symposium 2013 (DPS2013), Ramada Plaza Jeju Hotel, Jeju, Korea, Aug.29 - 30, 2013	Y. Kondo, Y. Miyawaki, K. Takeda, H. Kondo, K. Ishikawa, T. Hayashi, M. Sekine, M. Hori
12	Mechanism of Generating Active Species and Etch Reaction in CH _x F _y Plasma	6th International Symposium on Advanced Plasma Science and its Applications for Nitrides and Nanomaterials, Meijo Univ. , Aichi, Japan, Mar. 2-6, 2014	Y. Kondo, Y. Miyawaki, K. Takeda, S. Tajima, H. Kondo, K. Ishikawa, T. Hayashi, M. Sekine, M. Hori

3. Research Project

- International Training Program (Program for incubating young researchers on plasma nanotechnology materials and device processing, conducted by Japan Society for the Promotion of Science) in Prof. Goeckner research group, University of Texas at Dallas, Dallas, USA, from January to March, 2012.
- International Training Program (Program for incubating young researchers on plasma nanotechnology materials and device processing, conducted by Japan Society for the Promotion of Science) in at Prof. Han research group, Sungkyunkwan University, Suwon, Korea, from August to October, 2012.

4. Awards

- John Coburn and Harold Winters Student Award in Plasma Science and Technology, Finalist
AVS 59th International Symposium & Exhibition, AVS 59th International Symposium & Exhibition, Oct.28-Nov. 2, 2012